FAULT ZONE DAMAGE, NONLINEAR SITE RESPONSE, AND DYNAMIC TRIGGERING ASSOCIATED WITH SEISMIC WAVES

A Dissertation
Presented to
The Academic Faculty

by

Chunquan Wu

In Partial Fulfillment
of the Requirements for the Degree
DOCTOR OF PHILOSOPHY (GEOLOGICAL SCIENCES) in the
SCHOOL OF EARTH AND ATMOSPHERIC SCIENCES,
GEORGIA INSTITUTE OF TECHNOLOGY

Georgia Institute of Technology

August, 2011

FAULT ZONE DAMAGE, NONLINEAR SITE RESPONSE, AND DYNAMIC TRIGGERING ASSOCIATED WITH SEISMIC WAVES

Approved by:

Dr. Zhigang Peng, Advisor
School of Earth and Atmospheric Science
Georgia Institute of Technology

Dr. Dominic Assimaki
School of Civil and Environmental Engineering
Georgia Institute of Technology

Dr. Josef Dufek
School of Earth and Atmospheric Science
Georgia Institute of Technology

Dr. Andrew V. Newman
School of Earth and Atmospheric Science
Georgia Institute of Technology

Dr. Karim Sabra
School of Mechanical Engineering
Georgia Institute of Technology

Date Approved: May 27, 2011

To my Family

ACKNOWLEDGEMENTS

I would like to first thank my advisor Dr. Zhigang Peng for his patience, support, and guidance at all stages of my doctoral work. His expertise, innovative vision, and advices inspired me during all the years that I worked with him. I would also thank my committee members Dr. Andrew Newman, Dr. Dominic Assimaki, Dr. Josef Dufek, and Dr. Karim Sabra for their valuable discussion and critical comments.

This work also benefits from the discussion and helps from many researchers. I would like to give my thanks to Dr. Yehuda Ben-Zion, Dr. Leland Timothy Long, Dr. Peng Zhao, Kevin Chao, Dr. Tao Jiang, Dr. Chi-Chia Tang, Dr. Zheqiang Shi, Dr. Wenzheng Yang, Dr. Weijun Wang, and Dr. Qi-Fu Chen. The fault zone trapped waves synthetic code is from Dr. Yehuda Ben-Zion. Financial support for my studies was provided by the National Science Foundation (grant EAR-0710959, EAR-0908310), Southern California Earthquake Center, and Georgia Institute of Technology.

I want to thank many of my colleagues and friends in Georgia Institute of Technology including Dr. Lujia Feng, Jaime Convers, Dr. Tatiana Toteva, Xiaofeng Meng, Yan Luo, Chuanfei Dong, Chastity Aiken, Kate Craft, Jennifer Telling, Chenxiao Du, Jeff Hoeft and all the other current and past members in the Geophysics group. I also want to thank Dr. Judith Curry, Dr. Ellery Ingall, Dr. Carol Paty, Dr. Kurt Frankel, Dr. Christian Huber, Kathy Plummer, Laura Cederquist, and Susan Ryan for their advices and help.

Last but most important, I would like to thank my parents and other family members for their love and support. To them I dedicate this work.

TABLE OF CONTENTS

CHAPTER 5: TEMPORAL CHANGES OF SITE RESPONSE DURING THE M9.0 TOHOKU EARTHQUAKE IN JAPAN

LIST OF TABLES

LIST OF FIGURES

SUMMARY

My dissertation focuses primarily on the following three aspects associated with passing seismic waves in the field of earthquake seismology: temporal changes of fault zone properties, nonlinear site response, and dynamic triggering.

Quantifying the temporal changes of material properties within and around active fault zones (FZ) is important for better understanding of rock rheology and estimating the strong ground motion that can be generated by large earthquakes. As high-amplitude seismic waves propagate through damaged FZ rocks and/or shallow surface layers, they may produce additional damage leading to nonlinear wave propagation effects and temporal changes of material properties (e.g., seismic velocity, attenuation). Previous studies have found several types of temporal changes in material properties with time scales of tens of seconds to several years. Here I systematically analyze temporal changes of fault zone (FZ) site response along the Karadere-Düzce branch of the North Anatolian fault that ruptured during the 1999 İzmit and Düzce earthquake sequences. The coseismic changes are on the order of 20-40%, and are followed by a logarithmic recovery over an apparent time scale of ~1 day. These results provide a bridge between the large-amplitude near-instantaneous changes and the lower-amplitude longer-duration variations observed in previous studies. The temporal changes measured from this high-resolution spectral ratio analysis also provide a refinement for the beginning of the longer more gradual process typically observed by analyzing repeating earthquakes.

An improved knowledge on nonlinear site response is critical for better

understanding strong ground motions and predicting shaking induced damages. I use the same sliding-window spectral ratio technique to analyze temporal changes in site response associated with the strong ground motion of the Mw6.6 2004 Mid-Niigata earthquake sequence recorded by the borehole stations in Japanese Digital Strong-Motion Seismograph Network (KiK-Net). The coseismic peak frequency drop, peak spectral ratio drop, and the postseismic recovery time roughly scale with the input ground motions when the peak ground velocity (PGV) is larger than ~5 cm/s, or the peak ground acceleration (PGA) is larger than ~100 Gal. The results suggest that at a given site the input ground motion plays an important role in controlling both the coseismic change and postseismic recovery in site response.

In a follow-up study, I apply the same sliding-window spectral ratio technique to surface and borehole strong motion records at 6 KiK-Net sites, and stack results associated with different earthquakes that produce similar PGAs. In some cases I observe a weak coseismic drop in the peak frequency when the PGA is as small as ~20-30 Gal, and near instantaneous recovery after the passage of the direct *S* waves. The percentage of drop in the peak frequency starts to increase with increasing PGA values. A coseismic drop in the peak spectral ratio is also observed at 2 sites. When the PGA is larger than ~60 Gal to more than 100 Gal, considerably stronger coseismic drops of the peak frequencies are observed, followed by a logarithmic recovery with time. The observed weak reductions of peak frequencies with near instantaneous recovery likely reflect nonlinear response with essentially fixed level of damage, while the larger drops followed by logarithmic recovery reflect the generation (and then recovery) of additional rock damage. The results indicate clearly that nonlinear site response may occur during medium-size earthquakes, and that the PGA threshold for *in situ* nonlinear site response is lower than the previously thought value of ~100-200 Gal.

The recent Mw9.0 off the Pacific coast of Tohoku earthquake and its aftershocks generated widespread strong shakings as large as ~3000 Gal along the east coast of Japan. I systematically analyze temporal changes of material properties and nonlinear site response in the shallow crust associated with the Tohoku main shock, using seismic data recorded by the Japanese Strong Motion Network KIK-Net. I compute the spectral ratios of windowed records from a pair of surface and borehole stations, and then use the sliding-window spectral ratios to track the temporal changes in the site response of various sites at different levels of PGA The preliminary results show clear drop of resonant frequency of up to 70% during the Tohoku main shock at 6 sites with PGA from 600 to 1300 Gal. In the site MYGH04 where two distinct groups of strong ground motions were recorded, the resonant frequency briefly recovers in between, and then followed by an apparent logarithmic recovery. I investigate the percentage drop of peak frequency and peak spectral ratio during the Tohoku main shock at different PGA levels, and find that at most sites they are correlated.

The third part of my thesis mostly focuses on how seismic waves trigger additional earthquakes at long-range distance, also known as dynamic triggering. Previous studies have shown that dynamic triggering in intraplate regions is typically

not as common as at plate-boundary regions. Here I perform a comprehensive analysis of dynamic triggering around the Babaoshan and Huangzhuang-Gaoliying faults southwest of Beijing, China. The triggered earthquakes are identified as impulsive seismic arrivals with clear *P*- and *S*-waves in 5 Hz high-pass-filtered three-component velocity seismograms during the passage of large amplitude body and surface waves of large teleseismic earthquakes. I find that this region was repeatedly triggered by at least four earthquakes in East Asia, including the 2001 Mw7.8 Kunlun, 2003 Mw8.3 Tokachi-oki, 2004 Mw9.2 Sumatra, and 2008 Mw7.9 Wenchuan earthquakes. In most instances, the microearthquakes coincide with the first few cycles of the Love waves, and more are triggered during the large-amplitude Rayleigh waves. Such an instantaneous triggering by both the Love and Rayleigh waves is similar to recent observations of remotely triggered 'non-volcanic' tremor along major plate-boundary faults, and can be explained by a simple Coulomb failure criterion. Five earthquakes triggered by the Kunlun and Tokachi-oki earthquakes were recorded by multiple stations and could be located. These events occurred at shallow depth (< 5 km) above the background seismicity near the boundary between NW-striking Babaoshan and Huangzhuang-Gaoliying faults and the Fangshan Pluton. These results suggest that triggered earthquakes in this region likely occur near the transition between the velocity strengthening and weakening zones in the top few kms of the crust, and are likely driven by relatively large dynamic stresses on the order of few tens of KPa.

CHAPTER 1

INTRODUCTION

1.1 Overview of Seismic Wave Propagation Effects

When an earthquake occurs within the earth, part of the energy is radiated in the form of elastic seismic waves traveling through or along the surface of the earth. The most well-known and publicly-concerned effect of seismic waves is ground motion, the shaking caused by seismic waves travelling to the surface of the earth. Devastating earthquakes may generate strong ground motion in nearby region, and result in major loss in lives and properties of human beings. In addition, the strong ground motion associated with seismic waves could also trigger tsunami, landslide, and other natural disasters. In the case of earthquake hazard, the two most important parameters are the amplitude and duration of ground motion (McGuire 2004), which are determined by the magnitude, location, depth of the earthquake source, the quality factor, density, and dynamic properties of the Earth's medium, and the type of sites.

Seismic waves are important to seismologists because they could be recorded by surface and borehole seismometers, and have been utilized in a wide range of applications. These include seismic imaging of the earth's interior structure, earthquake source properties and seismic hazard analysis, and exploration of petroleum and other natural resources. In most cases, seismic wave propagation is considered as linear elastic. That is, when the amplitude of the seismic wave is small, the medium will return its initial stage after the wave passage. However, if the amplitude of the wave (or the associated dynamic stress) is large enough, it would cause a change the elastic property of the medium during its propagation path and other secondary effects. This phenomenon is termed as nonlinear wave propagation effects and usually found for highly fractured region such as shallow sedimentary layers (e.g. Yu *et al.* 1992) and fault damage zones (e.g. Vidale & Li 2003). Nonlinear site effects are typically associated with strong ground motions (>100 Gal, e.g. Beresnev & Wen 1996a), which are typically found in regions close to the epicenters of large earthquakes, as the amplitudes of seismic waves attenuate rapidly with distance. On the other hand, many recent studies have found that surface waves of large earthquakes could cause perturbations in the stress fields of regions that are several hundreds to thousands of kilometers away, and result in transient fault slip and dynamically triggered earthquakes and tremor activities (e.g. Hill *et al.* 1993; Rubinstein *et al.* 2007b).

1.2 Motivations and Objectives

Investigations of the nonlinear wave propagation effects within and around active fault zones (FZ), and in the near-surface layers, are important for better understanding rock rheology, estimating seismic hazard, predicting future ground motions (Frankel *et al.* 2000), and designing geotechnical and structural engineering systems (NEHRP 2003). Investigations of dynamic triggering effects could help to improve the understanding of the underlying mechanisms of earthquake initiation and interaction, which are both key components of earthquake forecasting and hazard analysis. During my Ph.D. work, I conducted a comprehensive investigation of the seismic wave propagation effects, including nonlinear site effects and dynamic triggering effects, which are presented in this dissertation. These studies provide new/additional observations and evidences of wave propagation effects, and will help to improve our understanding of the controlling parameters and underlying mechanisms of the observations.

1.3 Thesis Organization

This thesis mainly consists of four published papers (Wu *et al.* 2009a, 2009b, 2010, 2011), and one in press (Wu & Peng 2011). In the following Chapter 2, I present a study of temporal changes in FZ site response associated with strong ground motion of the 1999 Mw7.1 Düzce earthquake (Wu *et al.* 2009b). Chapter 3 describes a detailed study of temporal changes in site response of shallow layers associated with the strong ground motion of the Mw6.6 2004 Mid-Niigata earthquake sequence in Japan (Wu *et al.* 2009a). In Chapter 4, I present a systematic analysis of nonlinear effects and temporal changes of site response associated with medium-size earthquakes, using seismic data recorded by the Japanese Strong Motion Network KIK-Net (Wu *et al.* 2010). In Chapter 5, I present a similar study of nonlinear site effects during the recent Mw9.0 Tohoku earthquake in Japan (Wu & Peng 2011). Chapter 6 focuses on dynamic triggering around the Babaoshan and

Huangzhuang-Gaoliying faults near Beijing, China (Wu *et al.* 2011). Finally in Chapter 7, I conclude this dissertation by summarizing the observations, and discussing some future directions.

CHAPTER 2

Non-linearity and Temporal Changes of Fault Zone Site Response Associated with Strong Ground Motion

2.1 Introduction

2.1.1 Fault Zone Structures

Large earthquakes occur on major fault zone (FZ) structures. The faulting process produces localized belts of damaged FZ rocks (Figure 2.1) that have lower elastic moduli than the surrounding rocks (e.g. Ben-Zion & Sammis 2003, and references therein). The FZ damage is pronounced in the top few km of the crust, because increasing normal stress suppresses the damage generation and enhances the healing process of damage recovery (e.g. Lyakhovsky *et al.* 1997; Ben-Zion & Shi 2005; Johnson & Jia 2005; Rice *et al.* 2005; Finzi *et al.* 2009). The top few hundred meters of the crust away from faults are also heavily fractured due to weathering processes, seismic motions, seasonal thermoelastic strain, and other forces that operate under very low normal stress conditions. The shallow surface layers are characterized by extremely low shear wave velocity (~200-400 m/s) and very high attenuation (Q ~1-10) (e.g. Aster & Shearer 1991). Quantifying the temporal changes of material properties within and around active FZs, and in the near-surface layers, is important for better understanding rock rheology and estimating the strong ground motion that can be generated by large earthquakes.

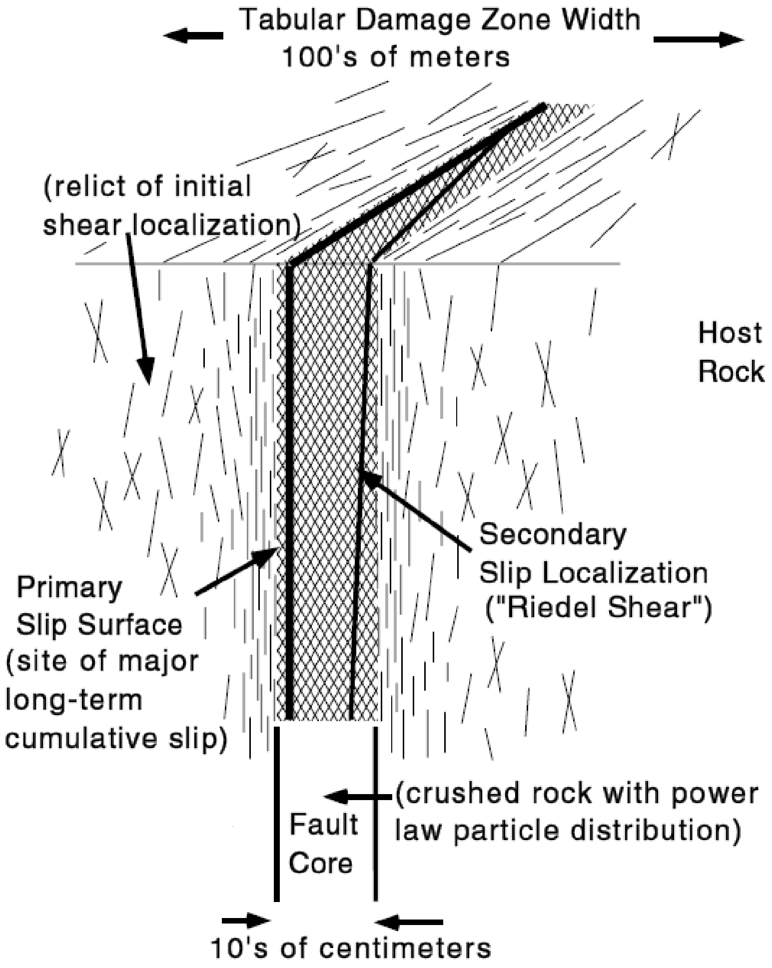

Figure 2.1 A conceptual representation of fault damage zone structures (after Ben-Zion & Sammis 2003).

2.1.2 Previous Approaches

As high-amplitude seismic waves propagate through damaged FZ rocks and/or shallow surface layers, they may produce additional damage leading to non-linear wave propagation effects and temporal changes of material properties (e.g., seismic velocity, attenuation). Recent studies based on waveform cross-correlations of repeating earthquakes observed clear changes of seismic velocities in shallow surface layers and around active FZs, with rapid reductions during strong motions of nearby large earthquakes followed by logarithmic recoveries (Rubinstein & Beroza 2004a, b; Rubinstein & Beroza 2005; Peng & Ben-Zion 2006; Rubinstein *et al.* 2007a). The use of repeating earthquakes allows separation of spatial variations from temporal changes of material properties (e.g. Peng & Ben-Zion 2005, 2006), but is limited by the availability of repeating earthquakes in the study area. Some studies employed repeating artificial sources (e.g. Li *et al.* 1998, 2006; Vidale & Li 2003 , see Figure 2.2), but these types of studies are limited by high cost and poor depth penetration.

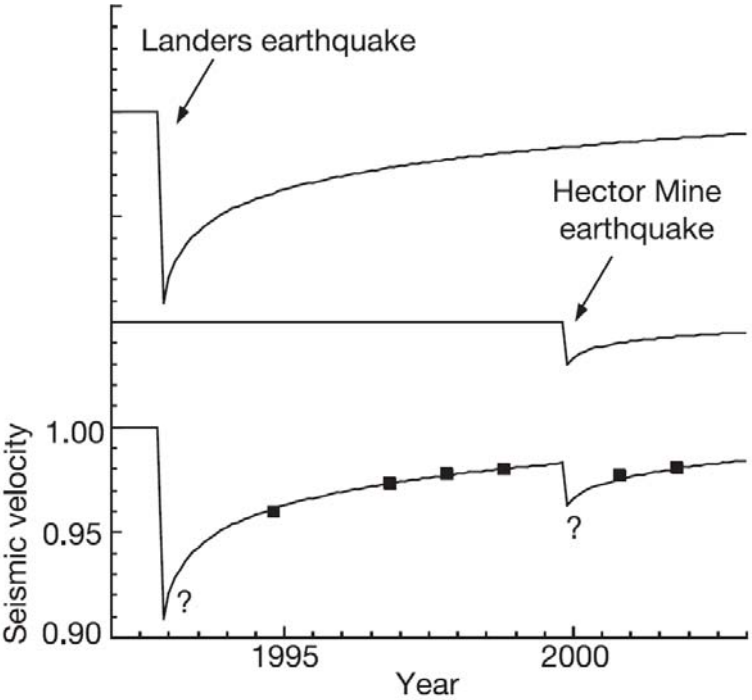

Figure 2.2 An example of seismic velocity drop and recovery at shallow Landers fault after Landers and Hector Mine earthquakes measured from repeating sources (after Vidale & Li 2003).

Another technique that has been widely applied to study non-linear site response of surface layers and sediments is the spectral ratio method (e.g. Beresnev & Wen 1996a; Field *et al.* 1997; Pavlenko & Irikura 2003; Sawazaki *et al.* 2006; Sawazaki *et al.* 2009). This method generally involves comparisons of weak and strong-motion responses based on the spectral ratio between a target and a reference site (e.g. nearby hard rock site or borehole). Recently, Karabulut & Bouchon (2007) applied the spectral ratio method to near-fault ground accelerations to quantify spatial variability and non-linearity along the Karadere-Düzce branch of the North Anatolian fault (NAF) in relation to the 1999 Mw7.1 Düzce earthquake. Their results indicated ~45 percent reduction in S-wave velocity during the Düzce main shock and near-instantaneous recovery (Figure 2.3). In comparison, based on waveform cross correlations of weak motion generated by repeating earthquakes in the same region, Peng & Ben-Zion (2006) found a much smaller percentage of co-seismic reduction in S-wave velocity (up to 3 percent) and a much longer time scale of recovery (at least 3 months, see Figure 2.4). The differences may stem from different resolutions of the employed data and analysis techniques along with different site conditions where the instruments are placed.

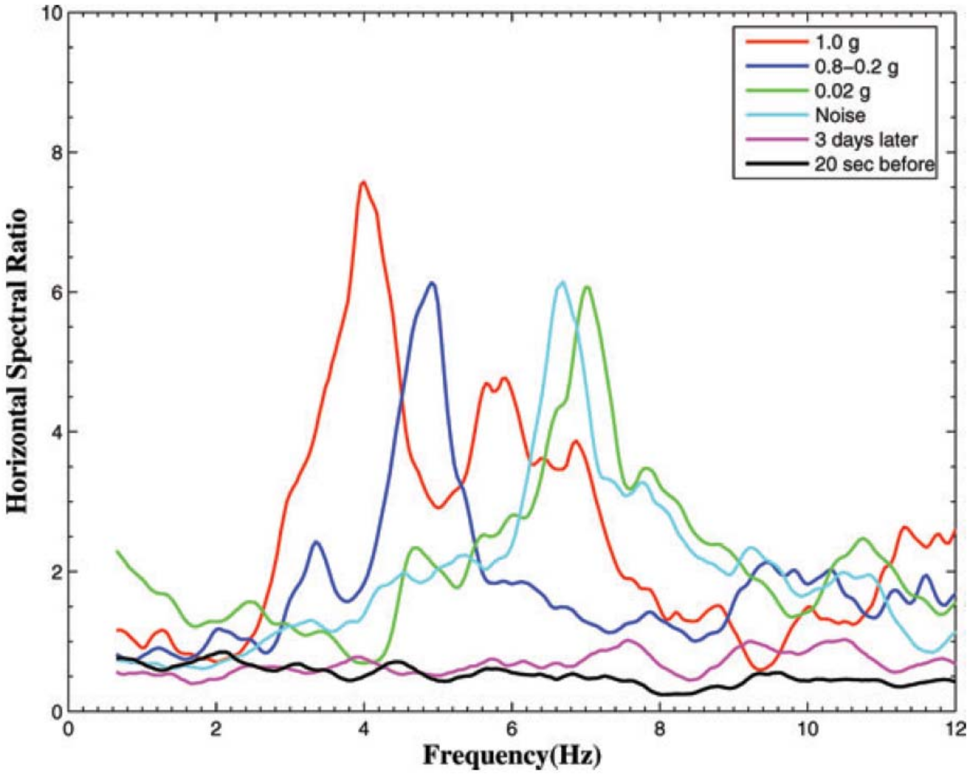

Figure 2.3 Average horizontal spectral ratios between on- and off-fault stations for the strong, weak motion and noise. (after Karabulut & Bouchon 2007)

2.1.3 Motivation

To better quantify temporal changes of FZ properties and investigate the differences in the above two studies, I apply the spectral ratio method to strong and weak motion data recorded by a pair of on- and off-fault stations before and during the Mw7.1 Düzce earthquake and its aftershocks. The analysis of the strong ground motion shows a 20-40 percent reduction of peak frequency (frequency of maximum spectral ratio amplitude) and 80-150 percent increase of peak spectral ratios (maximum of spectral ratio amplitude) at the FZ station immediately following the Düzce main shock, consistent with the ~45 percent reduction in S-wave velocity found by Karabulut & Bouchon (2007). These strong changes of spectral ratios are followed by a logarithmic recovery to the values before the main shock within ~1 day. The on-scale weak motion data used in the spectral ratio analysis start only ~6 hours after the Düzce main shock and show mild evolution of peak spectral frequency afterwards (within large error bars), consistent generally with the results of Peng & Ben-Zion (2006).

2.2 Data and Analysis Procedure

2.2.1 Seismic Data

The analysis employs primarily strong and weak motion data recorded by two stations VO and FP from a temporary 10-station PASSCAL seismic network (Figure 2.4a) along and around the Karadere-Düzce branch of NAF that was deployed a week after the August 17, 1999, Mw7.4 İzmit earthquake (Seeber *et al.* 2000; Ben-Zion *et al.* 2003). All 10 stations had REFTEK recorders and three-component L22 short-period sensors with a sampling frequency of 100 Hz. In addition, 8 stations (not including MO and GE) had 3-component force-balance accelerometers (FBA). During the six-month operational period, this network recorded seismograms of about 26000 earthquakes, including the November 12, 1999, Mw7.1 Düzce main shock, its foreshocks and aftershocks (Figure 2.4).

I use seismic waveforms recorded by the station pair VO and FP for the main analysis in this work, because these stations form the only pair that is deployed at close distance and has both strong and weak motion recordings. In particular, station VO is deployed on a shutter ridge with high relief, composed of gouge and slope debris inside the rupture zone of the İzmit earthquake. Station FP is ~400 m off the fault in soil near bedrock with medium relief (Figure 2.4b). Additional details regarding the seismic experiment and data set are given by Seeber et al. (2000) and Ben-Zion et al. (2003).

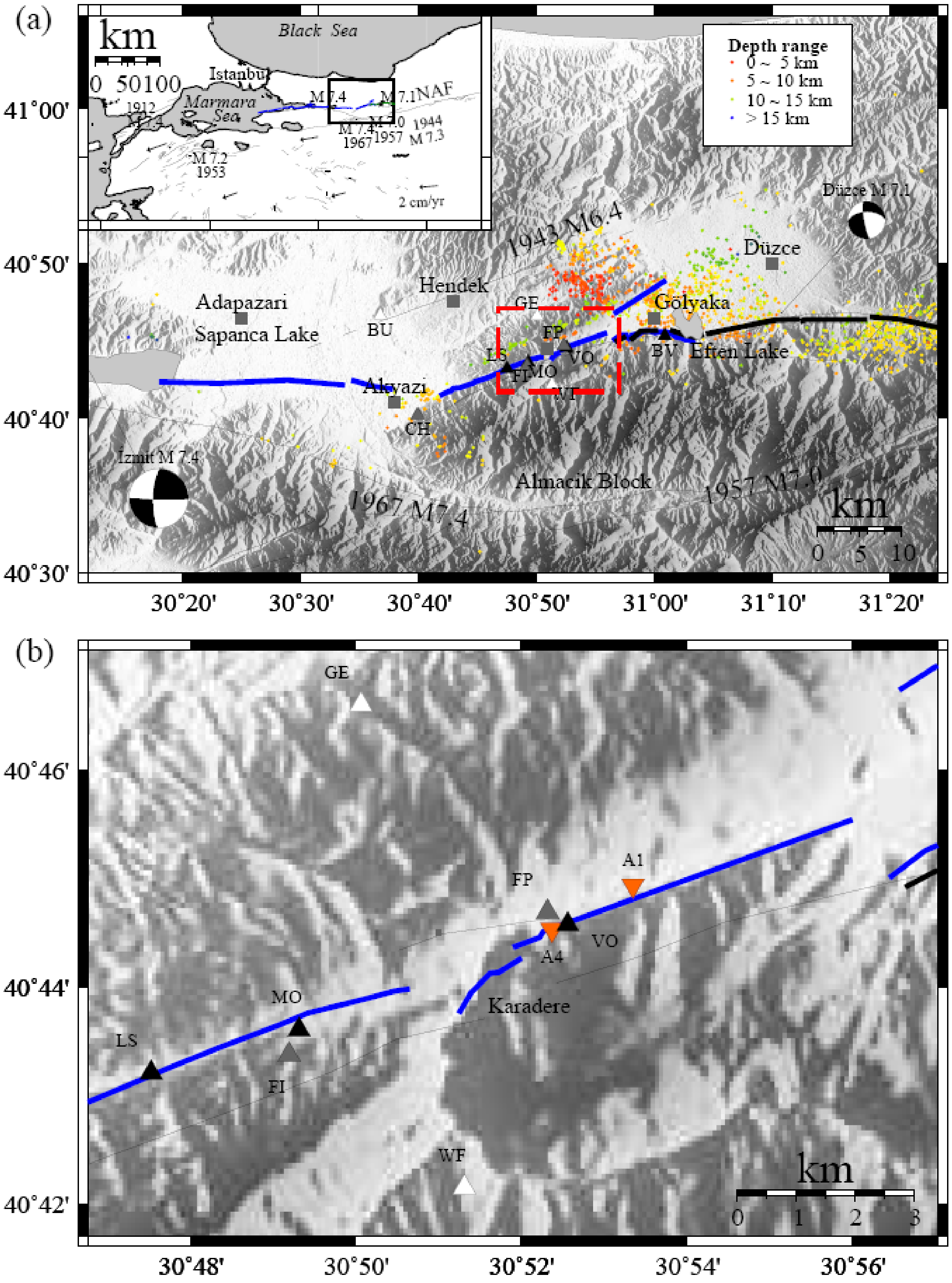

Figure 2.4 (a) Topographic map of the area along the Karadere-Düzce branch of the North Anatolian fault (NAF). Earthquake locations are marked by small dots with colors denoting different depth ranges. Shaded background indicates topography with white being low and dark being high. The surface ruptures of the İzmit and Düzce earthquakes are indicated with blue and black lines, respectively. Dark thin lines associated with earthquake information denote faults that were active during recent

ruptures. Other dark thin lines are geologically inferred fault traces. Stations within, near, and outside the FZ are shaded with dark, gray, and white triangles, respectively. Gray squares denote locations of nearby cities. The area bounded by the red dashed lines is shown in (b). The inset illustrates the tectonic environment in northwestern Turkey with the box corresponding to our study area. Vectors represent plate deformation rate (Reilinger *et al.* 1997) from GPS data. Modified from Peng & Ben-Zion (2006). (b) A zoom-in map around the location of the station VO inside the fault and FP ~400 m away from the fault. All the symbols and notations are the same as in (a). The inverted triangles mark seismic stations A1 and A4 used in the study of Karabulut & Bouchon (2007).

2.2.2 Analysis Procedure

The analysis generally follows the procedures of Sawazaki et al. (2006) and Karabulut & Bouchon (2007) and is briefly described here. I use the two horizontal-component ground acceleration records at stations VO and FP that are generated by 1806 earthquakes. These include 113 events starting 8 days before the Düzce main shock, the main shock, and 1692 events within 3 months after the main shock. The local magnitudes of most events range from 0 to 5, and the hypocentral depths range from 5 to 15 km. The occurrence times, magnitudes and peak ground accelerations (PGA) associated with the employed events are shown in Figure 2.5.

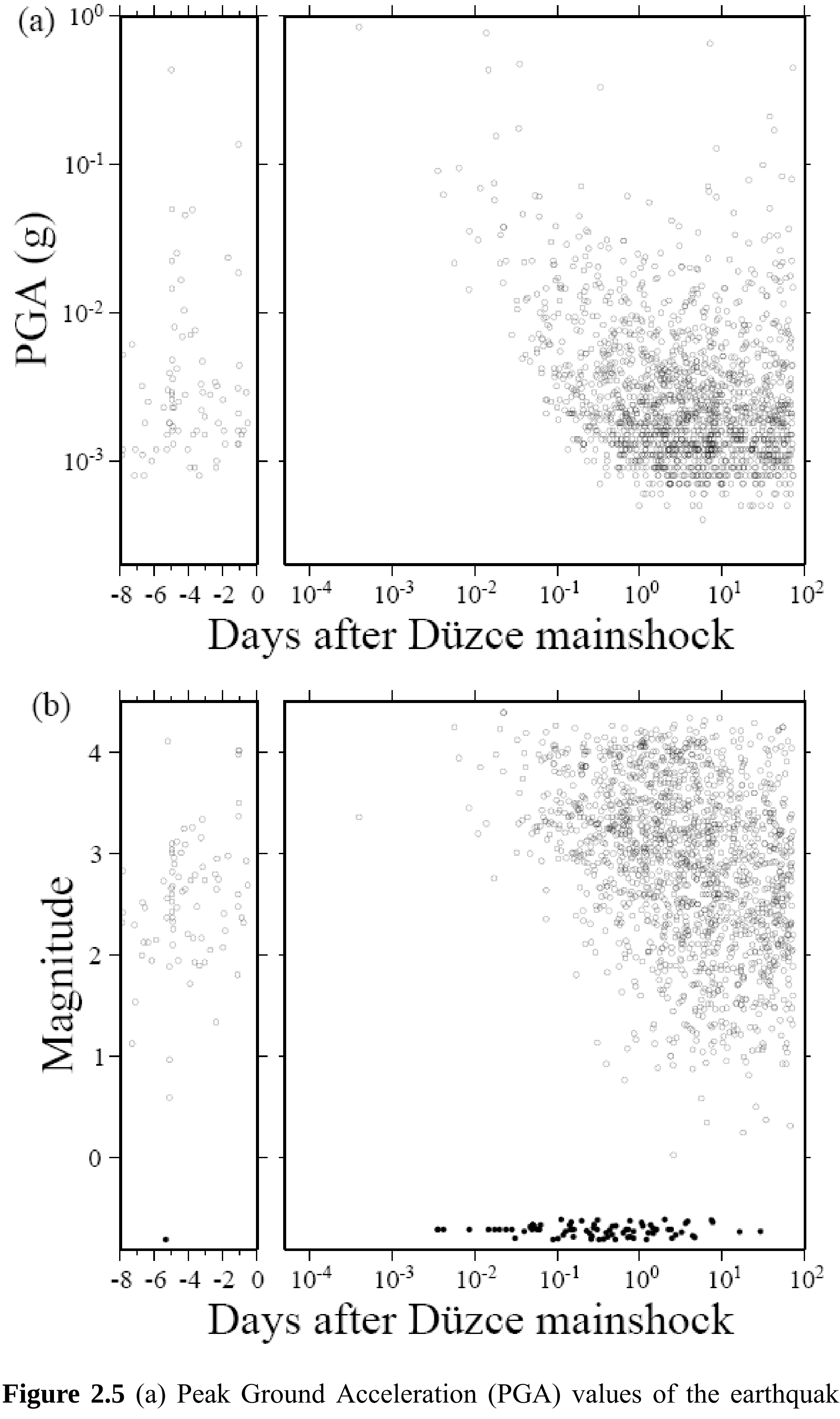

Figure 2.5 (a) Peak Ground Acceleration (PGA) values of the earthquakes used in this study plotted against occurrence times (days in linear scale before and logarithmic scale after the Düzce main shock) (b) Magnitudes of the earthquakes used in this study plotted against occurrence times (same as in a). Open and filled circles mark events that have magnitudes and those that do not, respectively. The events with

no magnitudes are plotted at the bottom of the figure around magnitude of –1, with a random number added for plotting purposes.

I analyze the entire seismic dataset using two slightly different approaches. In the first approach, I use 10-second time windows with origins that are moved forward by 5 seconds for all waveforms recorded at stations VO and FP. In this case all possible seismic phases, including pre-event noise, *P*, *S* and coda waves are analyzed together. In the second approach I only analyze data within a 10 seconds long coda wave window, which starts from twice the direct *S*-wave travel time after the origin time of each event (e.g. Sawazaki *et al.* 2006). To avoid mixing coda waves with other phases, I do not use the records in the coda-window-based analysis if there are any other events between the onset of the S-wave and the end of the coda window or if S-wave phases cannot be clearly identified.

Next, I remove the mean value of the traces and apply a 5 percent Hanning taper to both ends. I add the power spectra of the two horizontal components and take the square root of the sum to get the amplitude of the vector sum of the two horizontal spectra. The obtained spectra are smoothed by applying the mean smoothing algorithm from the subroutine “smooth” in the Seismic Analysis Code (Goldstein *et al.* 2003), with half width of five points. The spectral ratio is obtained by taking the ratio of the horizontal spectra for stations VO and FP. Figure 2.6 illustrates the analysis procedure with example waveforms generated by the Düzce main shock.

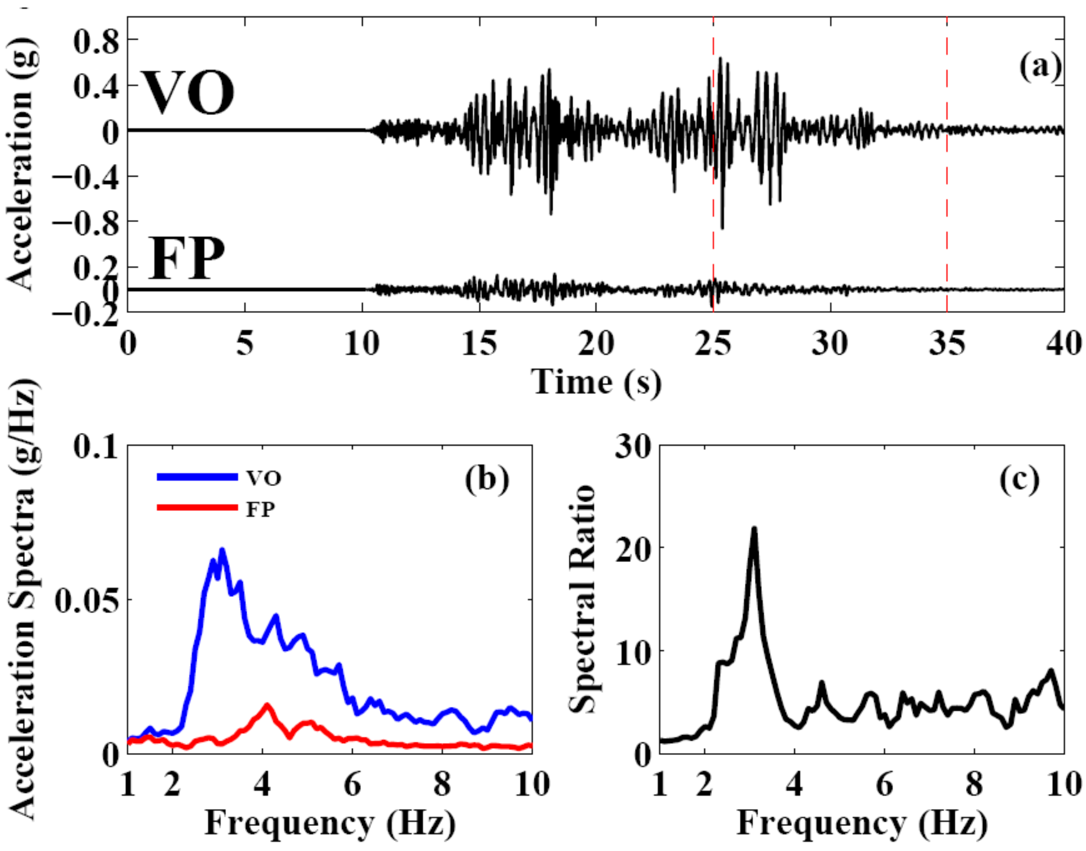

Figure 2.6 (a) Ground accelerations recorded at the two stations VO and FP during the 1999 Mw 7.1 Düzce, Turkey, earthquake. The red dashed lines indicate the time window that is used to compute the spectra in (b) and spectral ratio in (c).

The same procedure is applied to the weak motion data. I do not analyze time windows in which the peak velocity is above 80 percent of the maximum observed level at a given station, since these windows may be associated with clipped portions of waveforms (Yang *et al.* 2007).

2.3 Results

2.3.1 Strong Motion Data

After processing the sliding-window-based data, I obtain from the first approach 7543 spectral ratio traces, including 390 before the Düzce main shock, 7 during the main shock, and 7147 after the main shock. From the coda-window-based analysis, I obtain 697 spectral ratio traces, including 54 before the main shock and 643 after the main shock. Figure 2.7 shows a comparison of spectral ratios for the direct *S*-wave and the coda waves for 15 events within 2 hours after the main shock. The spectral ratios calculated from coda waves are generally similar to those calculated from the direct *S*-waves but with less scatter. This is consistent with the observations by Sawazaki *et al.* (2006) and Mayeda *et al.* (2007). This phenomenon can be attributed to the random distribution of heterogeneities and backscattered waves in the coda (Aki 1969; Aki & Chouet 1975). Such random distribution provides an averaging effect for the observed spectral ratios by making them less dependent on propagation paths than the direct *S*-wave (Phillips & Aki 1986). The disadvantage of using only the coda waves is that data in a certain time range (e.g., immediately after the main shock) may not be used due to overlapping seismic records (e.g. Peng *et al.* 2006). I therefore analyze in this study results using both approaches.

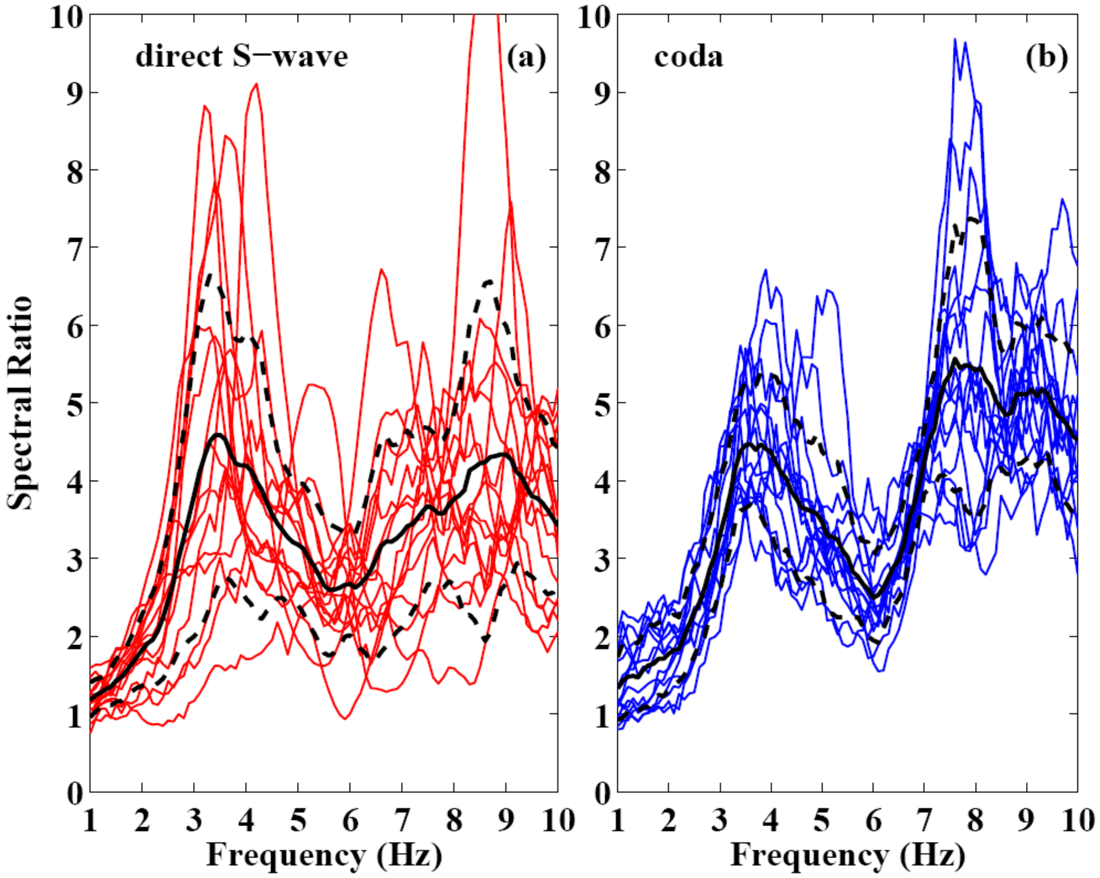

Figure 2.7 Spectral ratios for the strong motion data from (a) direct *S*-waves and (b) coda waves for 15 events occurred within two hours after the Düzce main shock. The black solid and dashed lines show the average spectral ratios and the standard deviation.

The temporal changes of spectral ratio for all phases and coda wave windows are shown in Figures 2.8a and 2.8b, respectively. In both plots, I observe a clear increase in peak spectral ratios and reduction in peak frequencies at the time of the main shock, followed by logarithmic recovery. To better quantify the degree of coseismic changes and the time scale of postseismic recovery, I obtain the values of peak spectral ratios and peak frequencies for all traces and average them in different time periods. I divide the whole dataset into the following periods: before the main shock, 10-30 s after the main shock, 300-1000 s after the main shock, and then every 0.25 interval in logarithmic time scale after 1000 s. I have tested averaging the peaks using different time windows and the obtained results remain essentially the same. I use logarithmic, instead of linear time because previous studies have found a logarithmic healing process for long-term recovery (e.g. Rubinstein & Beroza 2004a; Schaff & Beroza 2004; Peng & Ben-Zion 2006; Sawazaki *et al.* 2006). Next, I compute the average of the peak spectral ratios and peak frequencies in each time period. The same procedure is applied to the coda-window-based spectral ratio traces. Due to lack of data and overlapping records, there are gaps in the coda-window analysis at 0-30 s and 300-1000 s after the main shock.

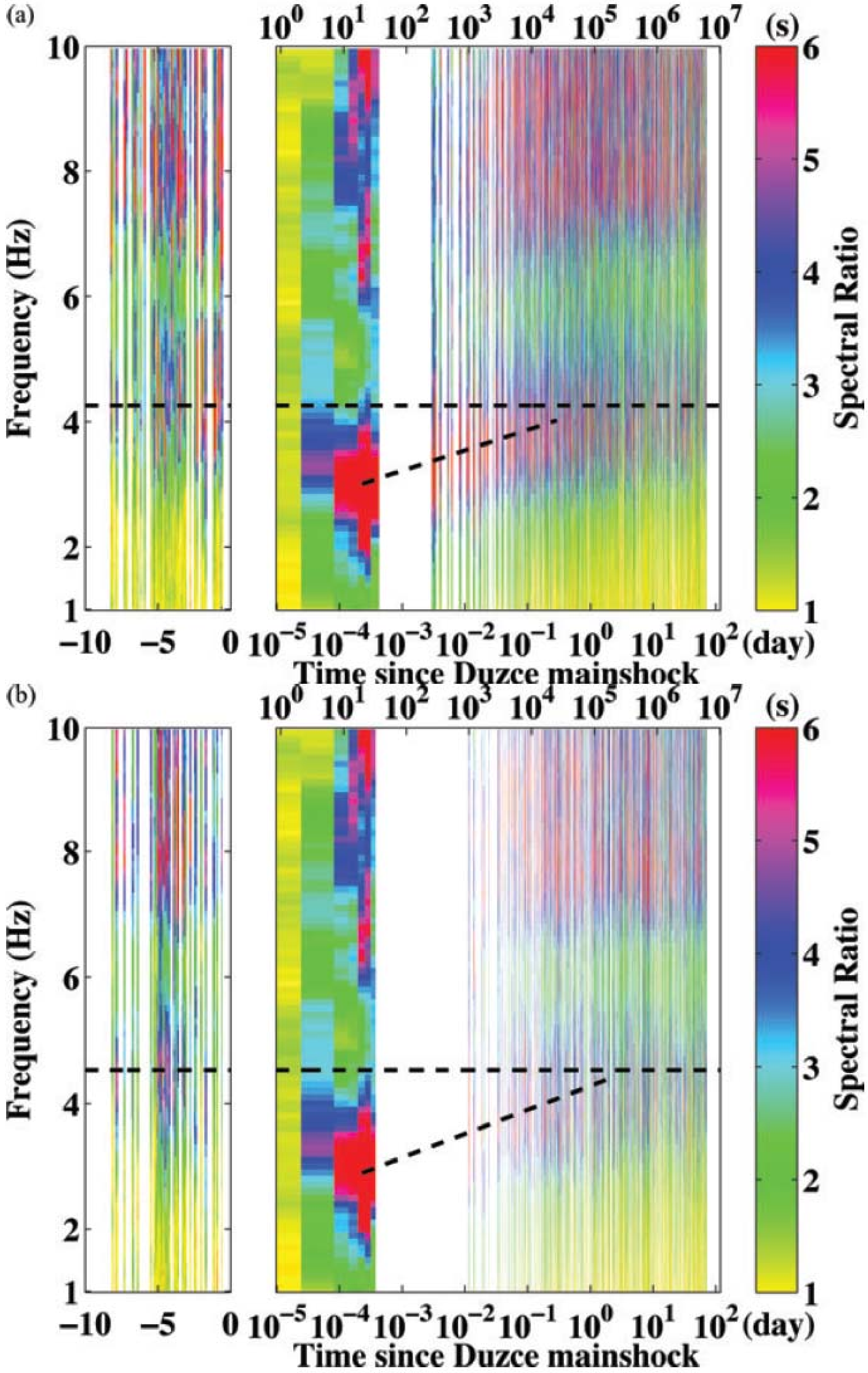

Figure 2.8 (a) Temporal changes of sliding-window-based spectral ratios for the

strong motion data at stations VO and FP. The right bin shows the color-coded spectral ratios for the main shock and aftershocks. The left bin shows those before the main shock. Values shown on the top and bottom of the figure indicate lapse times after the main shock in seconds and in days, respectively. White color represents no data. The horizontal and inclined black dashed lines show the pre-main shock value and the recovery trend, respectively. (b) Temporal changes of coda-window-based spectral ratio for the strong motion data at stations VO and FP. Symbols and notations are the same as in (a).

The averaged peak spectral ratios and frequencies with their standard deviations based on the analysis with all phases and only coda windows are shown in Figures 2.9a,c and Figures 2.10a,c, respectively. For comparison, the averaged peak spectral ratios and frequency in the period 0-30 s after the main shock from all phases are included in the results of the coda-window-based analysis (Figures 2.9a,c). The results from both datasets show a sudden increase of peak spectral ratio and a shift of the spectral peak to lower frequencies during the main shock. The values of the averaged peak spectral ratios and peak frequencies, together with the increase/reduction or recovery rates before, immediately after, and one day after the main shock are listed in Table 2.1. Both types of spectral ratio change show a near-complete recovery with a time scale of ~1 day after the main shock.

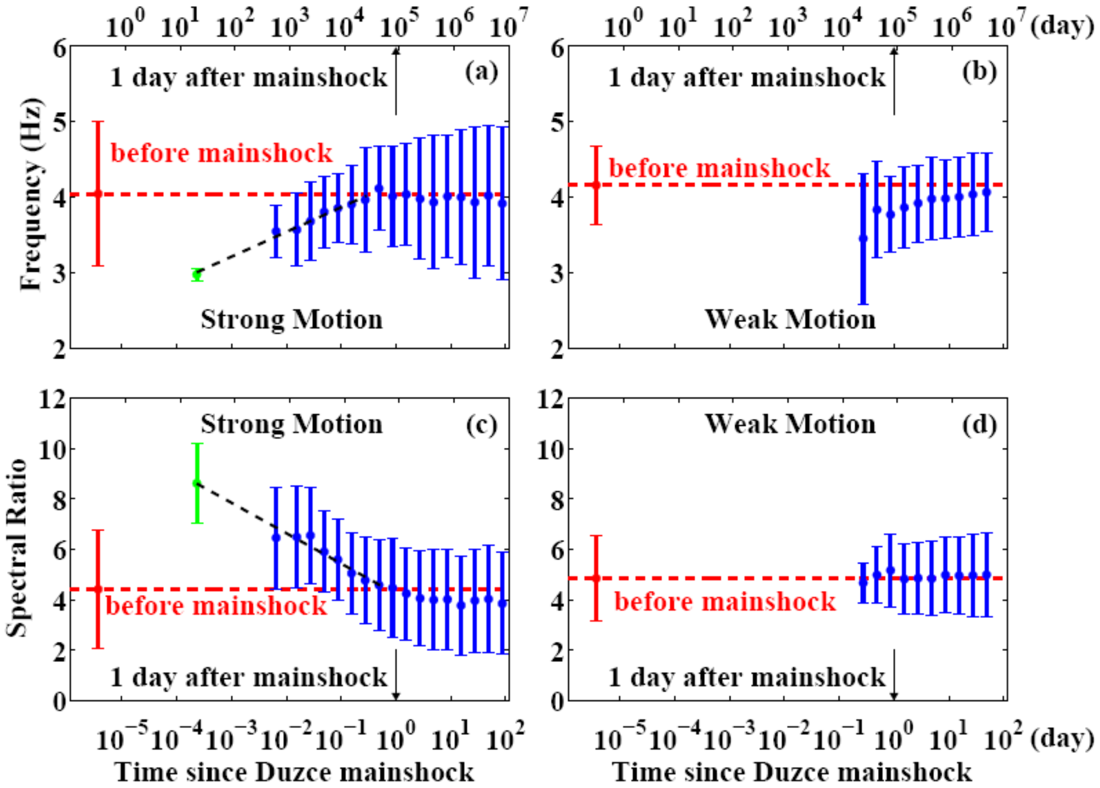

Figure 2.9 (a) Averaged peak frequencies from the sliding-window-based strong-motion data before (red), during (green), and after (blue) the main shock, recorded at stations VO and FP. Vertical solid bar centered at each data point shows the standard deviation. The red dashed line indicates the pre-main shock value of peak frequency. The vertical black line with arrow marks the time of 1 day after the main shock. Values shown on the top and bottom of the figure indicate lapse times after the main shock in seconds and in days, respectively. (b) Same plot as (a) for the weak motion data. (c) Averaged peak spectral ratios with the same symbols and notations as (a). (d) Same plot as (c) for the weak motion data.

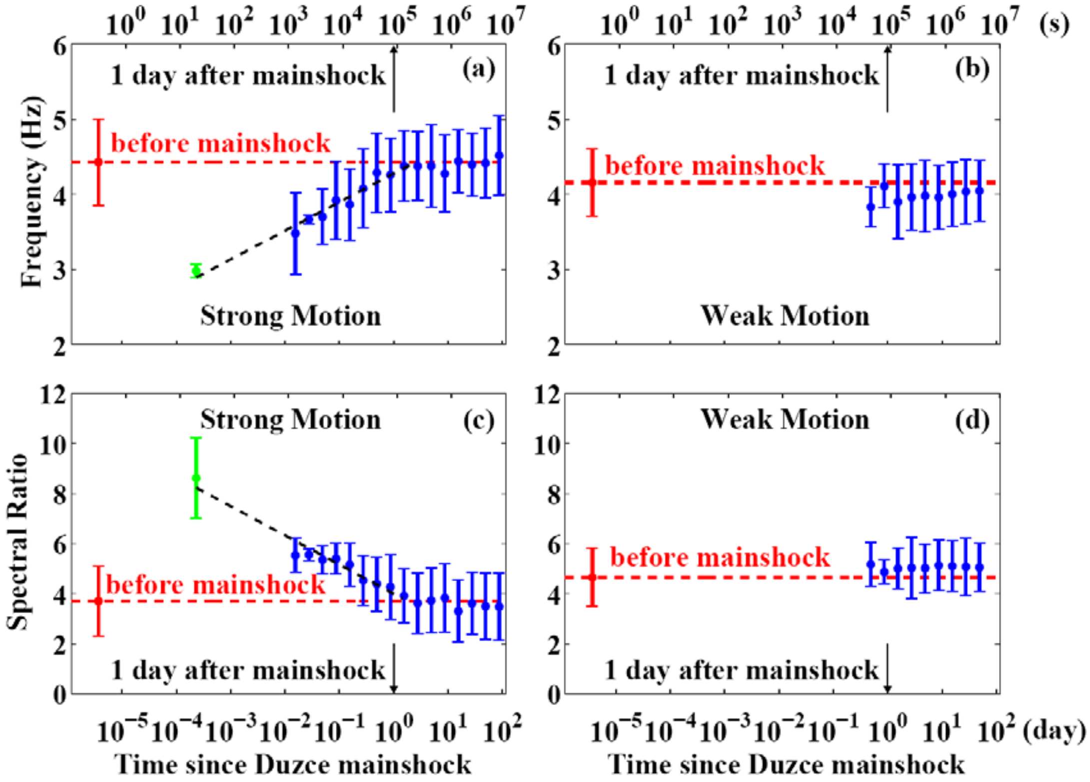

Figure 2.10 (a) Averaged peak frequencies from the coda-window-based strong-motion data before (red), during (green), and after (blue) the main shock, recorded at stations VO and FP. (b) Same plot as (a) for the weak motion data. (c) Averaged peak spectral ratios with the same symbols and notations as (a). (d) Same plot as (c) for the weak motion data. Other symbols and notations are the same as in Figure 2.9.

Table 2.1 Averaged peak spectral ratios, peak frequencies and increase/recovery rates with error assessments before, immediately after and 1 d after the main shock from (a) the sliding-window based analysis and (b) the coda-window based analysis.

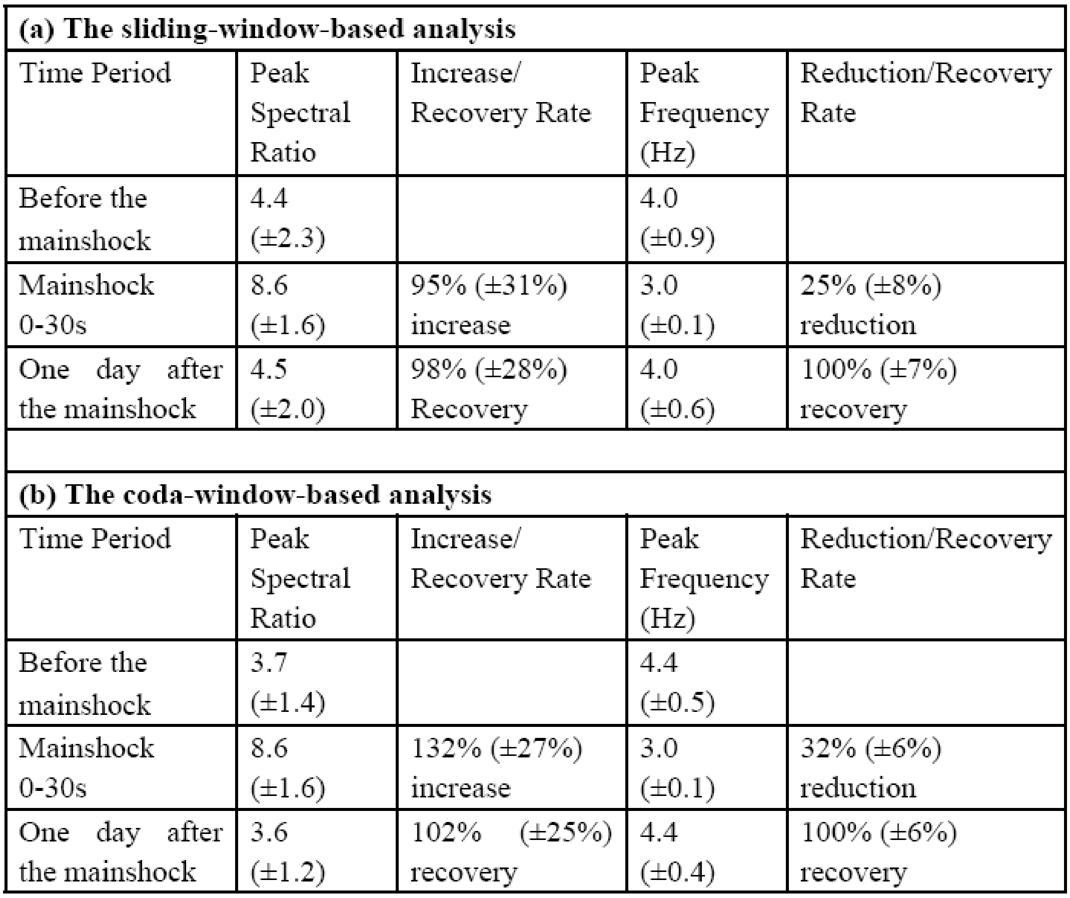

(a) The sliding-window-based analysis				
Time Period	Peak Spectral Ratio	Increase/ Recovery Rate	Peak Frequency (Hz)	Reduction/Recovery Rate
Before the mainshock	4.4 (±2.3)		4.0 (±0.9)	
Mainshock 0-30s	8.6 (±1.6)	95% (±31%) increase	3.0 (±0.1)	25% (±8%) reduction
One day after the mainshock	4.5 (±2.0)	98% (±28%) Recovery	4.0 (±0.6)	100% (±7%) recovery
(b) The coda-window-based analysis				
Time Period	Peak Spectral Ratio	Increase/ Recovery Rate	Peak Frequency (Hz)	Reduction/Recovery Rate
Before the mainshock	3.7 (±1.4)		4.4 (±0.5)	
Mainshock 0-30s	8.6 (±1.6)	132% (±27%) increase	3.0 (±0.1)	32% (±6%) reduction
One day after the mainshock	3.6 (±1.2)	102% (±25%) recovery	4.4 (±0.4)	100% (±6%) recovery

I have performed the same analyses on the vertical component seismograms but the results did not show clear spectral peaks and temporal changes in the same frequency range. This is consistent with observations that horizontal components are generally more sensitive to site amplification and other local structures than vertical components (e.g. Castro *et al.* 1997).

2.3.2 Weak Motion Data

Figures 2.9b, d and 2.10b, d show corresponding results for the weak motion data by applying the same averaging technique that has been used for the strong motion data. The obtained peak frequencies and spectral ratios are very similar to those from the strong motion data. Unfortunately, the results from the weak motion data lack useful data points within the first few hours after the main shock due to severe clipping of waveforms on the weak motion instruments. The peak frequencies from the time period with useful weak motion data are increasing gradually with time in the 3 months following the Düzce main shock. However, the large error bars imply that these changes are not well resolved by the employed spectral ratio technique. The amplitudes of the spectral ratios of the weak motion data do not show a clear pattern. In the following sections I focus on the results obtained from the strong motion data.

2.4 Synthesis Waveforms

In this section I attempt to relate the observed temporal changes of peak frequency and spectral ratios to changes of elastic properties within the FZ. Assuming a low-velocity FZ layer of width W in a half space (HS), the relation between the FZ fundamental resonance frequency f and the S-wave velocity β_{FZ} inside the FZ is given by $f = \beta_{FZ} / 2W$. A shift of peak frequency to lower value during the strong ground motions of the Düzce main shock can hence be related to the coseismic reduction of the S-wave velocity inside the FZ (Karabulut & Bouchon 2007).

2.4.1 2-D Model and Parameters

To quantify the relationship between the observed spectral changes and the velocity reduction in the FZ, I use the 2-D analytical solution of Ben-Zion & Aki (1990) and Ben-Zion (1998) for waveforms generated by a shear dislocation in a structure with a low-velocity FZ layer (Figure 2.11). Since the velocity variations along the FZ are much smaller than those across it, the 2-D model should provide a valid simplification of the 3-D velocity variations in the vicinity of the FZ. I simulate ground motion inside and outside the FZ using parameters obtained from analysis of FZ trapped waves in the same region (Ben-Zion *et al.* 2003). The employed parameters are: FZ width W = 100 m, S-wave velocities in the FZ and the half space $\beta_{FZ} = 1.5$ km s^{-1} and $\beta_{HS} = 3.2$ km s^{-1}, and quality factors in the FZ and the half space $Q_{FZ} = 10$ and $Q_{HS} = 1000$. As mentioned, Ben-Zion *et al.* (2003) and Peng & Ben-Zion (2004) found that the FZ damaged layer in the study area is confined primarily to the top ~3-4 km. I thus put the shear dislocation source at the depth of 3 km inside the FZ and 90 m from the left boundary near the right FZ interface. Station VO is placed in the middle of the FZ at the free surface and station FP is placed ~400 m away from VO. I use the first 4 s of the calculated synthetic ground velocity records, transfer them into acceleration records, and then compute the spectral ratio. An example is shown in Figure 2.12 to illustrate the procedure.

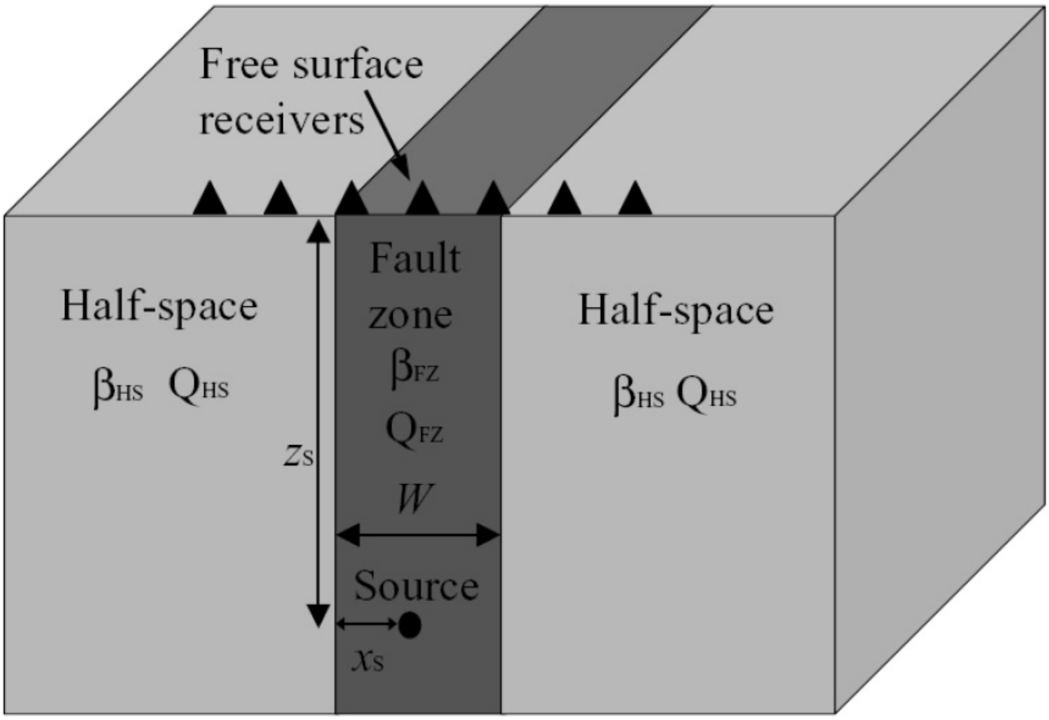

Figure 2.11 A three-media model for a uniform low-velocity FZ structure in a half-space. The source is an SH line dislocation with coordinates (x_S, z_S). The width, shear attenuation coefficient and shear wave velocity of the FZ are marked by *W*, Q_{FZ}, and β_{FZ}, respectively. The shear wave velocity and the attenuation coefficient of the HS are denoted by β_{HS} and Q_{HS} (after Ben-Zion *et al.* 2003).

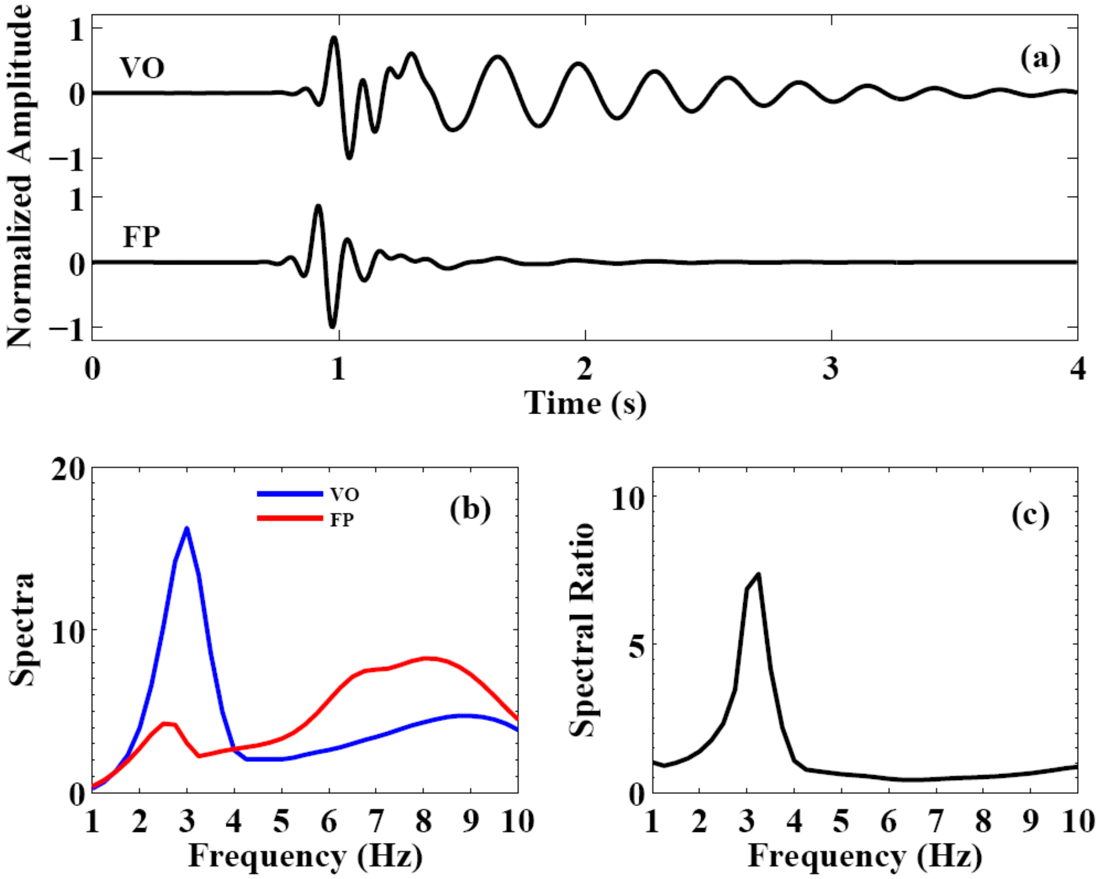

Figure 2.12 (a) Synthetic ground acceleration waveforms from the model in Figure 2.11. The acceleration traces are filtered between 1 and 10 Hz. The spectra in (b) and spectral ratio in (c) are smoothed by applying a mean smoothing algorithm with half width of 1 point.

2.4.2 Simulation Results

To estimate the expected spectral changes associated with evolution of FZ properties, I compute spectral ratios from sets of synthetic seismograms generated by changing the seismic velocity in the FZ and keeping the other parameters the same as above. Figure 2.13 shows spectral ratios obtained with five different values of β_{FZ}. As the β_{FZ} value is reduced from 2 to 1 km s^{-1}, the peak frequency decreases from 5.3 to

3.3 Hz and the peak spectral ratio increases from 4.9 to 7.3. These changes are consistent with the general patterns observed in Figures 2.8-2.9. I note that for a FZ width of 100 m, the peak frequency predicted from the basic relation $f = \beta_{FZ} / 2W$ is 10 Hz for β_{FZ} = 2 km s^{-1}, and 5 Hz for β_{FZ} = 1 km s^{-1}. This value is higher than the simulation results because the synthetic calculations employ a very low quality factor Q_{FZ} = 10 inside the FZ. The associated high attenuation tends to shift the fundamental frequencies of FZ waves to lower values (e.g. Ben-Zion 1998). If I use the same quality factor of 1000 for both the FZ and HS, the obtained peak frequencies match the basic equation well.

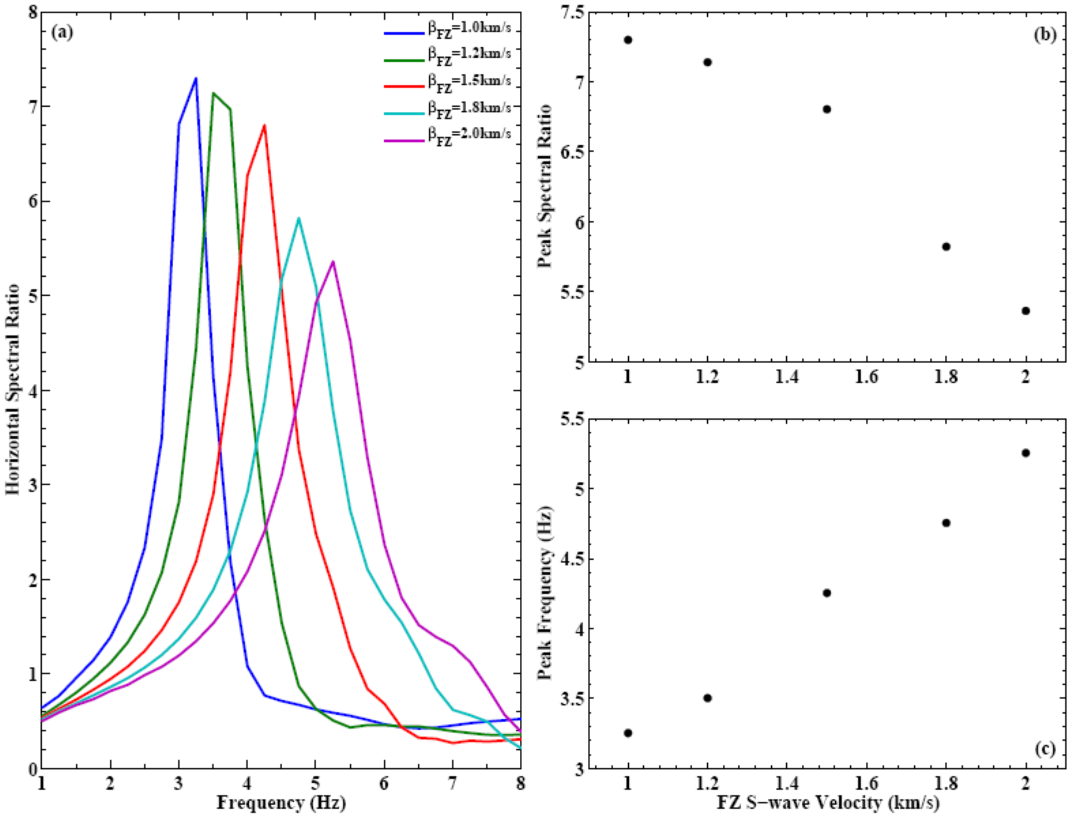

Figure 2.13 (a) Synthetic spectral ratios between stations VO and FP for five FZ *S*-wave velocities marked on the top right corner. (b) Peak spectral ratio and (c) peak

frequencies plotted against FZ *S*-wave velocity for the traces shown in (a).

To characterize better the likely changes of the FZ *S*-wave velocity, I perform synthetic simulations with β_{HS} values in the range from 0.5-3 km s^{-1} with increments of 0.01 km s^{-1}, and search for the values that best fit the observed peak frequency shifts (Figure 2.9a). The best fitting velocities and the corresponding peak frequencies and peak spectral ratios are shown in Figure 2.14a-c. The synthetic results indicate a reduction of the β_{FZ} value from ~1.6 km s^{-1} before the main shock to ~0.97 km s^{-1} immediately after the main shock (~40 per cent change) and near complete recovery in ~1day. I also perform a grid search of the FZ quality factor with the fixed β_{FZ} value of 1.5 km s^{-1} (Figure 2.14d-f). The results show that reducing the Q_{FZ} value can explain the observed peak frequency shift. But in this case the peak spectral ratios decrease, which is in contrast to our observations. The simulations indicate that temporal changes of β_{FZ} values play a major part in causing the observed spectral changes. A more complete analysis will employ simultaneous changes of multiple parameters (e.g. β_{FZ}, Q_{FZ} and W values) but this is left for a future work.

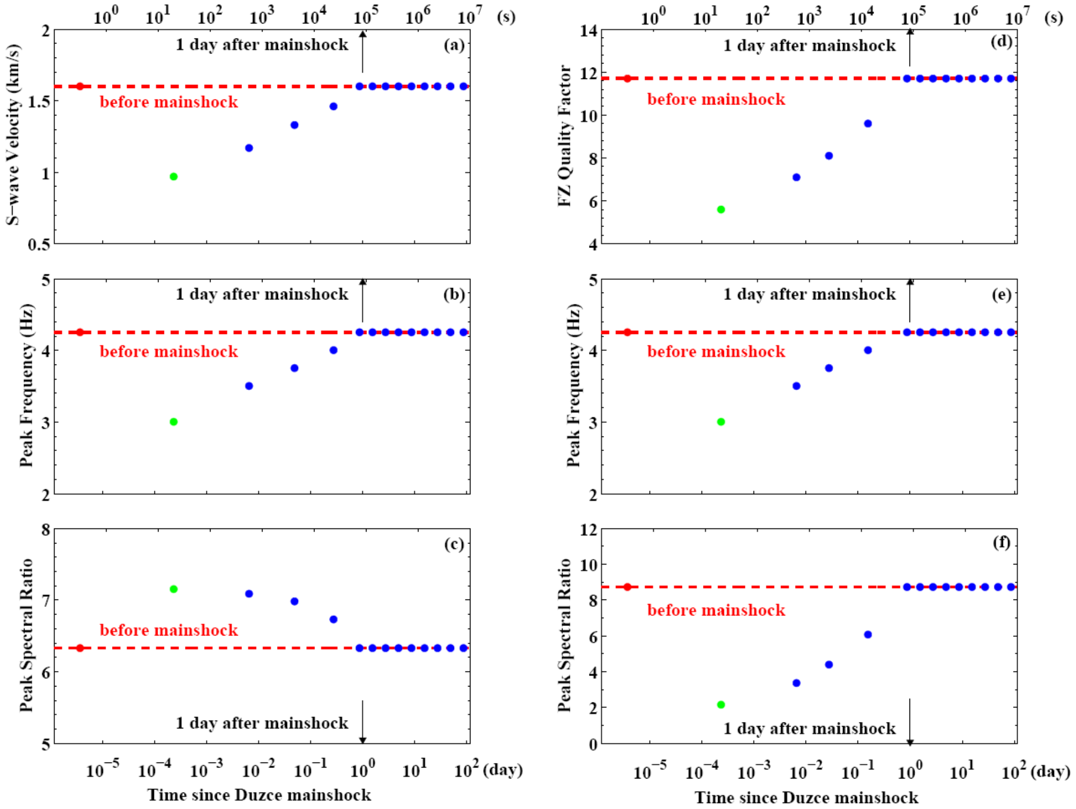

Figure 2.14 (a) Best fitting *S*-wave velocities from waveform simulation inside the FZ before (red), during (green), and after (blue) the main shock to the observed frequency shifts in Figure 6a. The red dashed line indicates the pre-main shock value. The vertical black arrow marks the time of 1 day after the main shock. Values shown on the top and bottom of the figure indicate lapse times after the main shock in seconds and in days, respectively. (b) Synthetic peak frequencies and (c) synthetic peak spectral ratios by varying the FZ *S*-wave velocity, with the same symbols and notations as (a). (d) Best fitting quality factor from waveform simulation. (e) Synthetic peak frequencies and (f) synthetic peak spectral ratios by varying FZ Q value.

2.5 Comparison with Previous Studies

2.5.1 Spatio-temporal Changes of FZ Properties

The Karadere segment of the NAF has been the focus of several detailed studies on spatio-temporal changes of FZ properties. Ben-Zion *et al.* (2003) performed a comprehensive analysis of seismic FZ trapped waves using the data set described in section 2.2.1. They concluded that the trapped waves along the Karadere segment are generated by ~100 m wide FZ layers that extend primarily to ~3-4 km depth and are characterized by strong attenuation (*Q* values of ~10-15) and 30-50 per cent velocity reduction from that of the host rock. Systematic analyses of seismic anisotropy with fault-parallel cracks in the same area (Peng & Ben-Zion 2004, 2005) indicated that the trapping structures are surrounded by 1-2 km wide zones with lower damage that also extend primarily to the top few km of the crust. Peng & Ben-Zion (2006) and Karabulut & Bouchon (2007) observed clear temporal changes of seismic properties and non-linear wave propagation effects near the Karadere fault. The damaged FZ layers that produce trapped waves, seismic anisotropy, scattering, and non-linear wave propagation effects are all likely parts of a hierarchical flower structure that resides primarily above the seismically-active portion of the crust. The anomalous wave propagation effects of the shallow damaged FZ layers may be referred to collectively as FZ-related site effects (Ben-Zion *et al.* 2003).

2.5.2 Differences in Recovery Time scale

Peng & Ben-Zion (2006) used a moving-window waveform cross-correlation technique to monitor the temporal changes of seismic velocities after the Düzce main shock using weak motion generated by repeating earthquakes. They found clear step-like co-main shock changes followed by logarithmic recovery over a time scale of at least 3 months in direct *S* and early *S*-coda waves (Figure 2.15a). The spectral ratio analysis of the strong ground motion in this study indicates ~20-40 per cent reduction of the peak frequency and recovery with time scale of 1 day. The spectral ratio analysis of weak motion in this study shows a mild recovery over the 3 months duration of the data within large scatter. Assuming that the observed temporal changes are accumulated in the top ~3 km of the crust (Ben-Zion *et al.* 2003), the coseismic change of seismic velocities extrapolated to the main shock time is on the order of a few per cent. However, if we assume that the thickness of the layer responsible for the temporal changes in only ~300 m (e.g. Rubinstein & Beroza 2005), the inferred coseismic velocity change at the FZ station VO is about 17 per cent (Figure 12b). This value is much closer to the ~45 per cent changes observed by Karabulut & Bouchon (2007) and in this study. Further decreasing the layer thickness to smaller values like 100 m would result in a better match of the co-seismic changes. As summarized in Figure 2.15, our spectral ratio results based on the strong motion data indicate a recovery time scale of ~1 day, which is much shorter than the ~3 month time scale of Peng & Ben-Zion (2006) but significantly longer than the near-instantaneous recovery inferred by Karabulut & Bouchon (2007).

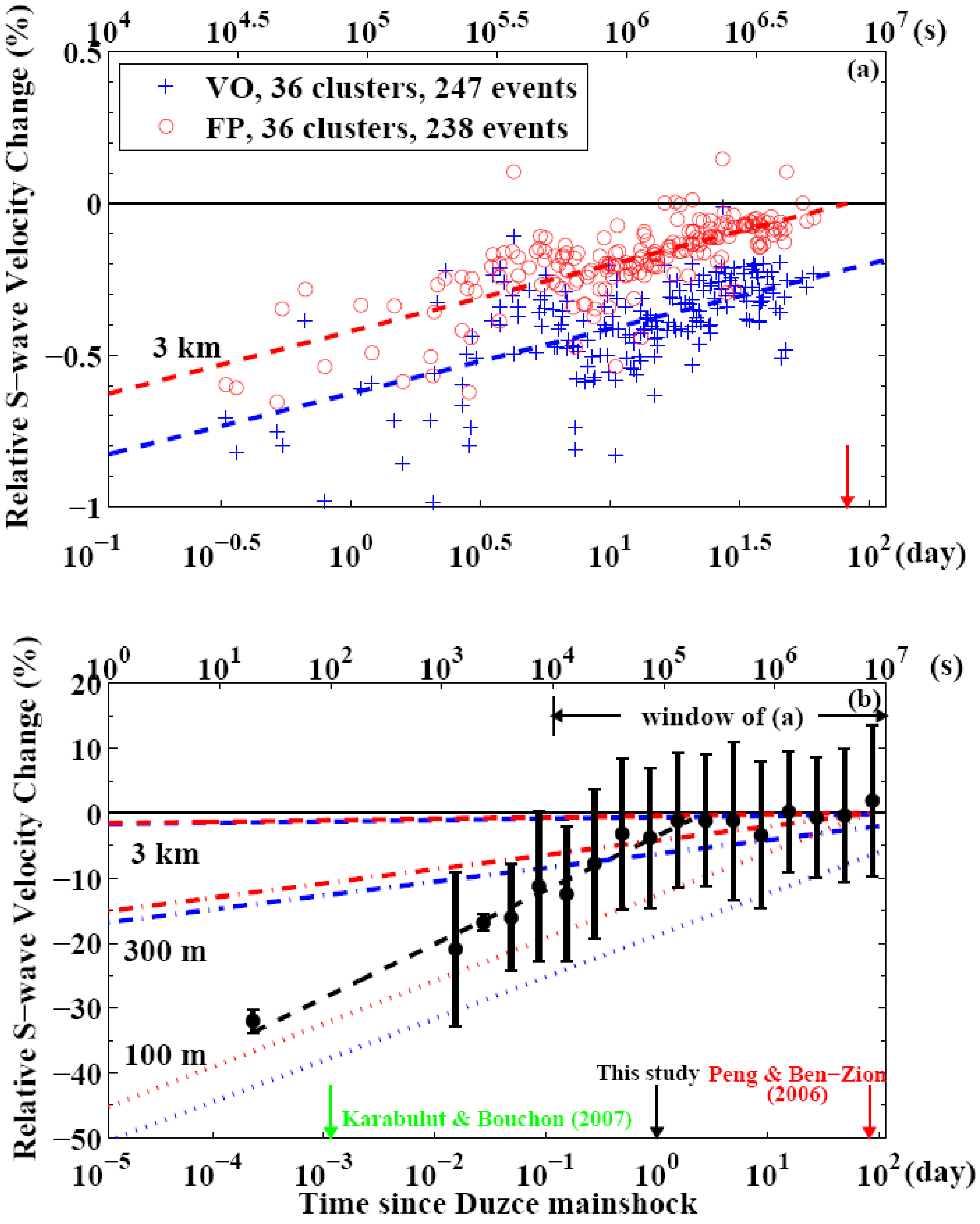

Figure 2.15 (a) Relative *S*-wave velocity changes inferred from time delays for early *S*-coda waves by Peng & Ben-Zion (2006). The blue crosses and red circles show measurements for stations VO and FP, respectively. The horizontal black solid line indicates the pre-main shock level of 0 per cent. The blue and red dashed lines are least-squares fits to the data, and the red arrow indicates the recovery time of at least 3 months. Values shown at the top and bottom of the figure indicate lapse times after the Düzce main shock in seconds and in days, respectively. (b) Relative *S*-wave

velocity changes measured from the averaged peak frequencies for the coda-window-based analysis. Vertical solid bar centered at each data point shows the standard deviation. The black dashed line shows the least-squares fit to the data observed in this study. The blue (VO) and red (FP) dashed lines, dash-dot lines, and dotted lines show the least-squares fits to the data shown in (a) assuming that temporal changes occur in the top 3 km, 300 m, and 100 m, respectively. The green, black and red arrows mark the time scale of recovery of ~100 s inferred by Karabulut & Bouchon (2007), ~1 day in this study, and at least 3 months by Peng & Ben-Zion (2006).

2.5.3 Possible Explanations

One possible explanation for the different results is the differences in the time scale of the usable data. The coseismic change and the apparent recovery within 1 day observed in this study are obtained from on-scale strong motion recordings during and immediately after the main shock (Figures 2.8-2.10). As noted in section 3, most of the weak motion recordings are saturated in this time period, thus preventing similar analysis based on repeating earthquakes (e.g. Peng & Ben-Zion 2006). Some waveforms may be clipped or buried inside seismograms of other events immediately after the main shock, and many earthquakes (including repeating events) are not detected in the standard earthquake catalogs (e.g. Peng *et al.* 2006, 2007; Enescu *et al.* 2007). A systematic search for repeating earthquakes in the early aftershock period (e.g. Peng & Zhao 2009) could provide useful information on the co-seismic changes in material properties of the shallow crust, and how they evolve within the initial minutes to hours after the main shock.

Another basic explanation for the differences of results is the use of different analysis techniques. In this study I employ station FP as the reference site for the spectral ratio calculations. However, as shown by Peng & Ben-Zion (2006) and Figure 2.15a, changes of seismic velocities are observed at both stations VO and FP during the Düzce main shock, although the degree of change at FP is smaller than that at VO. It is therefore clear that calculations based on the spectral ratios between these two stations give lower bound values for both the amplitude of the co-main shock change at station VO and the time scale of recovery. The spectral ratios of the strong motion records provide relatively high-resolution results on the very early large temporal changes of FZ properties following the Düzce main shock. The lower-amplitude longer-duration variations that occur at both stations are generally beyond the sensitivity of the spectral ratio analysis, as evident by the relatively constant values and large error bars for both the strong and weak motion data. Such subtle changes could be measured better by the repeating earthquakes analysis (e.g. Peng & Ben-Zion 2006).

The difference in the time scale of recovery between our results and those from Karabulut & Bouchon (2007) probably also stems from differences in the data sets and analysis procedures. In this study, I analyzed both weak and strong motion recordings from several days before to 72 days after the Düzce main shock. In addition, the distance between the station pair employed in this study is ~400 m, smaller than the 1.5 km distance for the station pair used by Karabulut & Bouchon (2007). Since I analyzed a larger dataset having smaller path effects, I am probably able to observe finer details of the very-early strong co-main shock changes and the more subtle longer-duration recovery process.

2.6 Discussion

Many factors could contribute to the temporal changes of seismic spectra observed in this study. These include apparent changes produced by varying radiation from sources at different locations, and physical changes occurring in shallow sediments and within the damaged FZ rocks. Because the two employed stations are very close to each other (~400 m) compared to the distances between the earthquakes sources and stations (typically more than 10 km), apparent changes from variable source locations are unlikely to be the reason for the observed changes. The presence of hard rock outcrops near the two stations VO and FP (Herece & Akay 2003), and the location of station VO within the FZ, reduce the likelihood that the results are dominated by shallow sediments, although such changes can contribute to the observations.

Temporal changes of seismic properties within the damaged FZ rocks that are initiated by the strong ground motion of the Düzce main shock are likely to be the main origin of the observed variations of the spectral ratios and peak frequencies. As suggested by the synthetic waveform simulations, the abrupt co-main shock changes are likely associated with reduction of seismic velocity in the FZ layer and to a lesser extent probably also reduction of the FZ attenuation coefficient. Such changes involve physically increasing crack and void densities in the shallow FZ structure, which can be generated by opening and growth of cracks inside the FZ and possibly also reduced packing of the near-surface granular material. During the post-main shock period the normal stress produces reversed processes associated with decreasing density of crack surfaces and increasing sediment packing. These healing processes produce logarithmic recovery of properties that approach asymptotically the pre-main shock levels. The discussed effects are observed in laboratory experiments with granular material and rocks (e.g. Dieterich & Kilgore 1996; Scholz 2002; Johnson & Jia 2005) and may be simulated using damage rheology models (e.g. Hamiel *et al.* 2004; Lyakhovsky & Ben-Zion 2008; Finzi *et al.* 2009).

The opening and growth of cracks in the damaged FZ material during strong ground motion is expected to increase the contrast of the seismic velocity across the FZ. This can increase the amplification of ground motion within the FZ, although part of the seismic energy could be consumed in the crack opening and growth processes and the amplification may be reduced partially by increasing attenuation. It is important to try to separate effects associated with reduced seismic velocities and increasing attenuation. However, detailed investigation of temporal changes in attenuation of the FZ material requires nearly identical microseismic sources (e.g. Bokelmann & Harjes 2000; Chun *et al.* 2004) to preclude source, path, and other variations, which is beyond the scope of this study.

It is not clear what parameters control the time scale of recovery. Previous studies suggested that diffusion of fluids may play an important role in the coseismic reduction and postseismic logarithmic recovery (e.g. Schaff & Beroza 2004; Sawazaki *et al.* 2006). However, logarithmic recovery is also expected due to generic enlargement of the real contact area of crack surfaces and grain contacts under normal stress (e.g. Marone 1998; Johnson & Sutin 2005). Although there is no direct evidence for the presence of fluids in our study area, many studies have observed widespread increase of water flow after several major earthquakes (e.g. Rojstaczer *et al.* 1995; Brodsky *et al.* 2003b; Wang *et al.* 2004; Manga & Wang 2007). They proposed that increasing permeability in the near surface layers due to strong shaking from the main shock is the main cause of increased fluid flow. Sawazaki *et al.* (2006) found a 30-70 per cent reduction of the peak frequencies in the coda-window-based spectral ratios using data recorded by vertical borehole arrays during the 2000 Western Tottori and 2003 Tokachi-Oki Earthquake sequences in Japan. The coseismic reduction is followed by a logarithmic recovery to pre-main shock value with time scales ranging from a few tens of minutes at a soft sandy gravel site to a few years at solid and weathered hard rock sites. If fluids play an important role in the process, the observed time scale could be mainly controlled by the permeability at each site, which is related to the specific site conditions, and would increase with the amplitude of seismic waves (Elkhoury *et al.* 2006). Additional field and laboratory studies are needed to clarify the precise processes controlling the co-seismic changes and timescale of the recovery process.

Our observations and the results of Karabulut & Bouchon (2007) of large co-seismic reduction of seismic velocities at FZ sites support the notion (e.g. Beresnev & Wen 1996a; Field *et al.* 1997) that non-linearity is widespread in the shallow crust during strong ground motion of moderate to large earthquakes. The analysis done in this study provides a bridge between the large-amplitude near-instantaneous changes inferred by Karabulut & Bouchon (2007) and the lower-amplitude longer-duration variations inferred by Peng & Ben-Zion (2006). The changes observed by the spectral ratio analysis provide a refinement for the beginning of the longer more gradual process observed by Peng & Ben-Zion (2006) and other related works based on waveform analysis of repeating earthquakes (e.g. Rubinstein & Beroza 2004a, b, 2005; Rubinstein *et al.* 2007a).

CHAPTER 3

Temporal Changes in Site Response Associated with Strong Ground Motion of 2004 Mw6.6 Mid-Niigata Earthquake Sequences in Japan

3.1 Introduction

3.1.1 Near Surface Nonlinearity

It has been long recognized that local site conditions have significant effects on the strong ground motions generated by large earthquakes (e.g., Joyner *et al.* 1976; Chin & Aki 1991; Yu *et al.* 1992). These studies have illustrated that the dynamic material properties, such as the shear modulus (G) and material attenuation (ξ), control the amplitude and frequency content of ground motions. More specifically, because the seismic velocities and densities of shallow sediments are generally much lower than those of the bedrock, amplification and resonance effects would occur due to conservation of energy. When the amplitude of the incident wave exceeds a certain threshold, the sediment response does not follow the linear Hooke's law with the input ground motion, resulting in nonlinear site effects. Overall, nonlinear effects have been shown to strongly correlate with the level of ground motion (e.g., Hartzell 1998; Su *et al.* 1998; Johnson *et al.* 2009) and local soil conditions (e.g., Beresnev & Wen 1996a; Hartzell 1998; Tsuda *et al.* 2006), and in terms of ground motion amplitude, typically manifest beyond an amplitude threshold of 100-200 Gal

(Beresnev & Wen 1996a). An improved knowledge on nonlinear site response is critical for better understanding and predicting strong ground motions.

3.1.2 Previous Work and Motivation

While most previous studies have focused on direct comparisons of site response during strong and weak ground motions to infer soil nonlinearity, several recent studies have also investigated the details of the nonlinearity recovery process by means of the spectral ratio method in different regions (e.g., Pavlenko & Irikura 2002b; Sawazaki *et al.* 2006, 2009; Karabulut & Bouchon 2007; Wu *et al.* 2009b). A general pattern emerged from these studies is a sharp reduction (on the order of 20-70%) of measured peak frequencies (i.e., resonant frequencies) in the spectral ratios during the strong ground motions of the nearby large main shock, followed by a time-dependent logarithmic recovery to the level before the main shock. However, the speed and time scale of the postseismic recovery is quite different, including near-instant recovery (Karabulut & Bouchon 2007), a few to tens of minutes (Pavlenko & Irikura 2002b; Sawazaki *et al.* 2006), around one day (Wu *et al.* 2009b), and several years (Sawazaki *et al.* 2006, 2009). It is still not clear whether the wide range of recovery time scales observed in these studies are mainly caused by differences in the local site conditions, choice of the reference site, employed method, or other factors. Whether the input ground motion is among the controlling parameters for the time scale or the speed of the postseismic recovery remains an open question.

A better understanding of the coseismic change and postseismic recovery in site response requires a good estimate of the input motion, and by far the best, although not perfect, source of information on the input motion came from downhole arrays. Downhole array records have provided direct *in situ* evidence of nonlinearity (e.g., Seed *et al.* 1970; Satoh *et al.* 2001). They are generally more accurate than surface-rock records as the input motion to surface soil (e.g., Satoh *et al.* 1995; Steidl *et al.* 1996), although the downgoing wavefields presented in borehole recordings could introduce some bias (Steidl *et al.* 1996). In this study, I apply a spectral ratio method to the strong motion data recorded by a pair of surface and borehole stations before, during, and after the 2004 Mid-Niigata earthquake sequence (Figure 3.1). The Mw6.6 main shock was followed by a vigorous aftershock sequence with at least 3 ~Mw6 events, which provides an ideal dataset to quantify the effects of the input ground motion on the degrees of nonlinearity and the recovery processes.

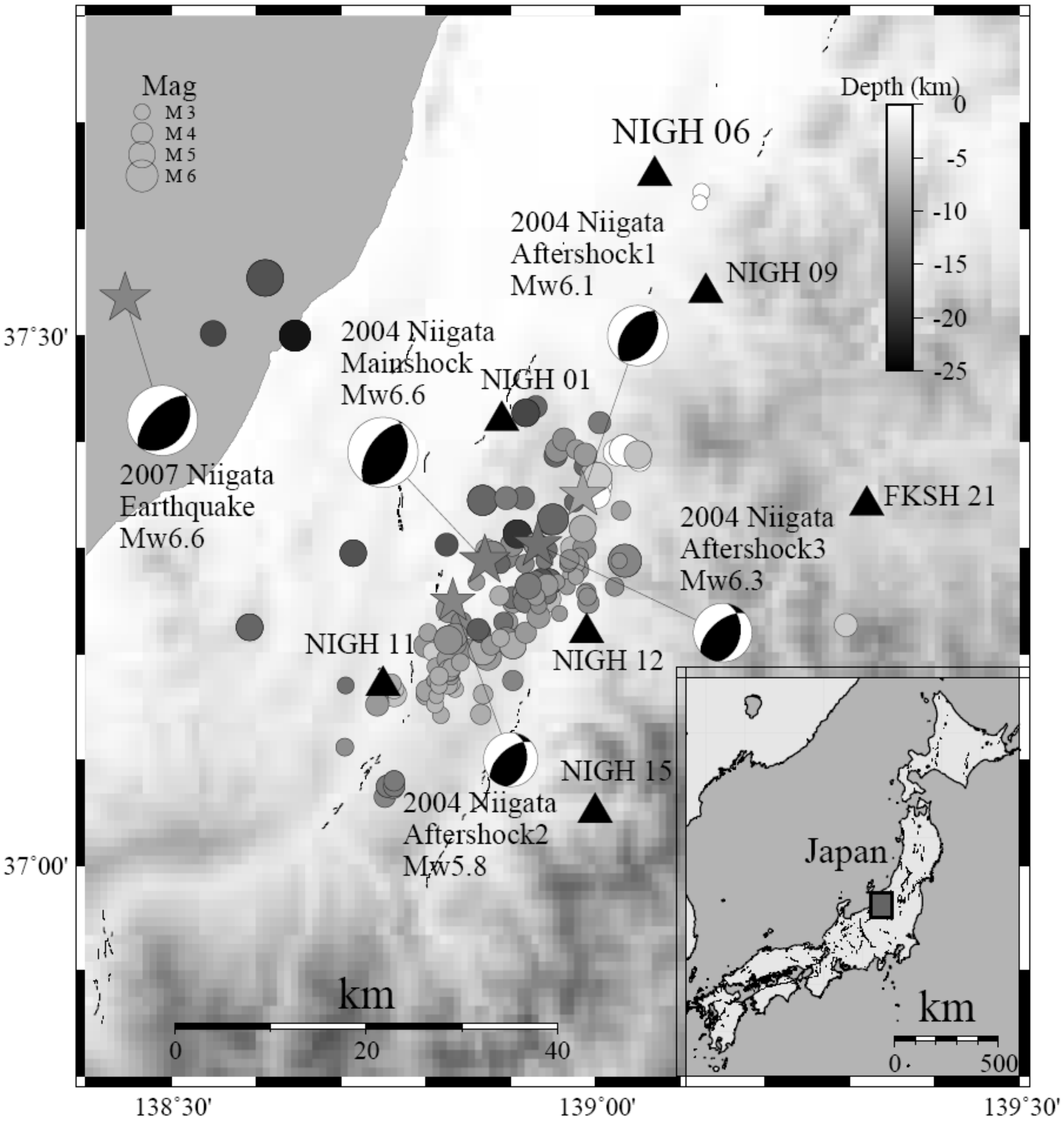

Figure 3.1 Topography map of the area along the west coast of Honshu, Japan. Shaded background indicates topography with white being low and dark being high. Epicenters of the 2004 Mw6.6 Mid-Niigata main shock, three large aftershocks, and the 2007 Mw6.6 Niigata-ken Chuetsu-oki earthquake are shown in stars together with their moment tensor solution. Other events are shown in circles. The size of circle indicates the magnitude of each event and gray scale shows the depth with white being shallow and dark being deep. Locations of 7 KiK-net stations within 50 km of the epicenter of 2004 Mid-Niigata main shock with PGA greater than 200 Gal are shown in black triangles. Black dash lines show the faults in this region. The inset shows the map of Japan. The box indicates the region shown in the topography map.

3.2 Seismic Data

The analysis employs strong motion data recorded by station NIGH06 in the Japanese Digital Strong-Motion Seismograph Network KiK-Net operated by National Research Institute for Earth Science and Disaster Prevention (Aoi *et al.* 2000). The network consists of 659 stations with an uphole/downhole pair of strong-motion seismometers. Each KiK-Net unit consists of three-component accelerometers and a data logger having a 24 bit A/D converter with a sampling frequency of 200 Hz.

Among all the 8 stations within 50 km of the epicenter of the 01/23/2004 Mw6.6 Mid-Niigata earthquake, the recorded peak ground acceleration (PGA) at stations NIGH01, NIGH06, NIGH09, NIGH11, NIGH12, NIGH15, and FKSH21 are larger than 200 Gal, a common threshold for nonlinear site amplification as found from previous studies (Chin & Aki 1991; Beresnev & Wen 1996a). I focus on the station NIGH06 (see Figure 3.1) for detailed analysis in this study mainly because the structure beneath the surface station is relatively simple with very low *S*-wave velocities, which has a larger potential for generating nonlinearity than other stations (Steidl *et al.* 1996; Tsuda *et al.* 2006). Indeed, the observed temporal changes in peak frequencies and peak spectral ratios (maximum of the spectral ratios) at station NIGH06 are much larger than those at other stations, allowing us to better quantify the differences associated with varying ground motions.

The borehole depth (below the surface) for station NIGH06 is 100 m. The rock types between the surface and borehole stations are clay with sand at the top 4 m, organic clay from 4 m to 7 m, gravel from 7 m to 43 m, and sandstone-mudstone from 43 m to 100 m. Additional details regarding the network and site conditions can be found at http://www.kik.bosai.go.jp/kik/index_en.shtml.

3.3 Analysis Procedure

The analysis procedure generally follows those of Sawazaki *et al.* (2006, 2009) and Wu *et al.* (2009b), and is briefly described here. I use two horizontal-component accelerations recorded at the surface and borehole seismometers and generated by 235 earthquakes. These include 38 events starting 4 years before, the Mid-Niigata main shock, and 196 events within 4 years after the main shock. The magnitudes of most events (except the main shock and some regional large events) range from 3 to 6.5, and the hypocentral depths range from 5 to 15 km.

I analyze the entire seismic data using two slightly different approaches (Wu *et al.* 2009b). In the first approach, I use 10-s time windows that are moved forward by 5 s for all waveforms recorded by the surface and borehole stations. In this case all possible seismic phases, including pre-event noise, *P*, *S* and coda waves are analyzed together. This sliding-window-based approach is applied to the records of the Mid-Niigata main shock and three largest aftershocks with magnitude Mw>6 to track the temporal changes immediately after the strong motion, and also to all the events for the statistical analysis described later in Section 3.4. In the second approach I only analyze data within a 10-s-long coda wave window, which starts from twice the direct

S-wave travel time after the origin time of each event (Sawazaki *et al.* 2006). Figure 3.2a shows an example of the original acceleration records generated by an M5.2 aftershock on Nov 04, 2004 and the coda wave window used to compute the spectral ratio. To avoid mixing coda waves with other phases, I did not use the records in the coda-window-based analysis if there are any other events between the onset of the *S*-wave and the end of the coda window or if *S*-wave phases cannot be clearly identified. The coda-window-based approach has been shown to have less scatter than the sliding-window-based analysis (Sawazaki *et al.* 2006; Wu *et al.* 2009b), and here we apply it to all the events to track possible long-term changes.

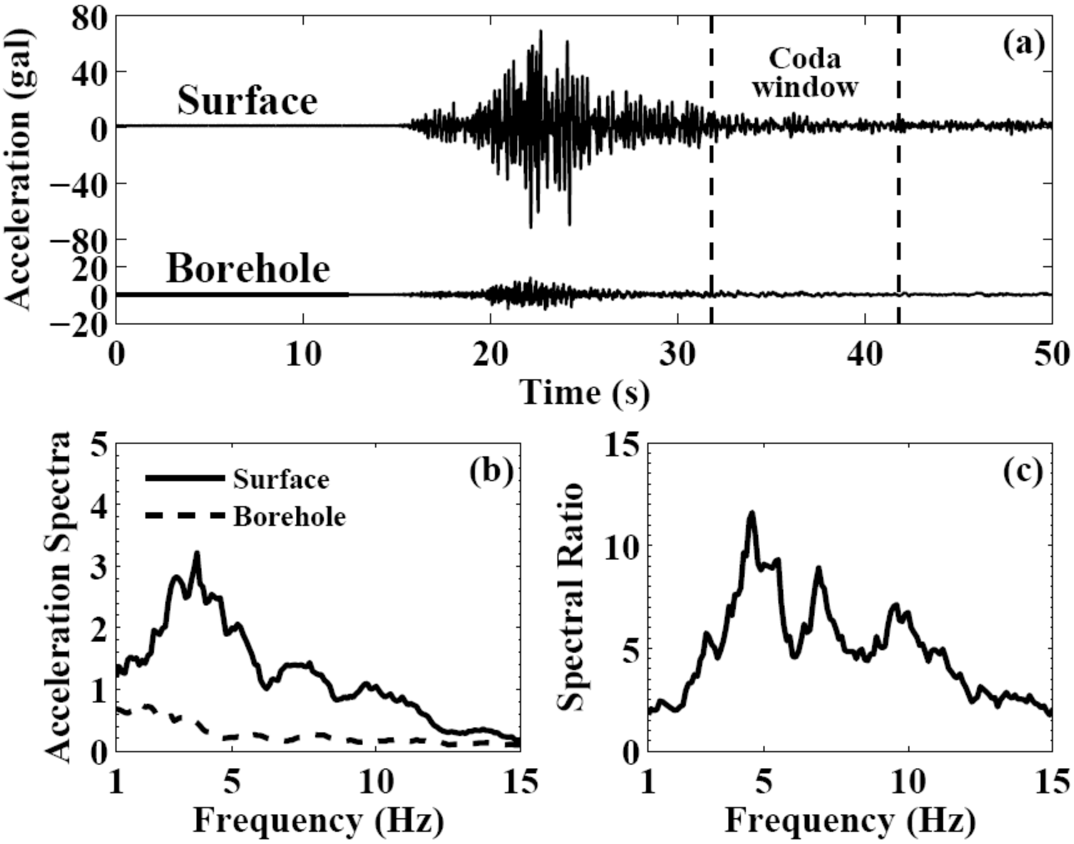

Figure 3.2 (a) East-component ground accelerations recorded at the station NIGH06

generated by an M5.2 earthquake on Nov 04, 2004. Surface recording is shown at the top and borehole recording is shown at the bottom. The dashed lines indicate the coda window that is used to compute the acceleration spectra in (b) and spectral ratio in (c).

Next, I remove the mean value of the traces and apply a 5 per cent Hanning taper to both ends. I add the power spectra of the two horizontal components and take the square root of the sum to get the amplitude of the vector sum of the two horizontal spectra. The obtained spectra are smoothed by applying the mean smoothing algorithm from the subroutine "smooth" in the Seismic Analysis Code (Goldstein *et al.* 2003), with half width of five points. The spectral ratio is obtained by taking the ratio of the horizontal spectra for surface and borehole stations. The amplitude of the spectra for both the surface and downhole recordings, and the resulting spectral ratio for the aforementioned aftershock recordings are shown in Figure 3.2b and c.

3.4 Results

After processing all the data, I obtain 5935 spectral ratio traces for station NIGH06 from the sliding-window-based analysis. From the coda-window-based analysis, I obtain 210 spectral ratio traces. Next, I select those spectral ratio traces from events with PGA exceeding 20 Gal to ensure signal-to-noise ratio, and combine the spectral ratios from the sliding-window-based analysis for the Mid-Niigata main shock and largest aftershocks with those from the coda-window-based analysis for all the other selected events (Figure 3.3). The running spectral ratios show clear decreases in peak spectral ratios and peak frequencies at the time of the main shock and three large aftershocks, followed by a logarithmic-type recovery. In addition, the coseismic changes appear to be different for these events.

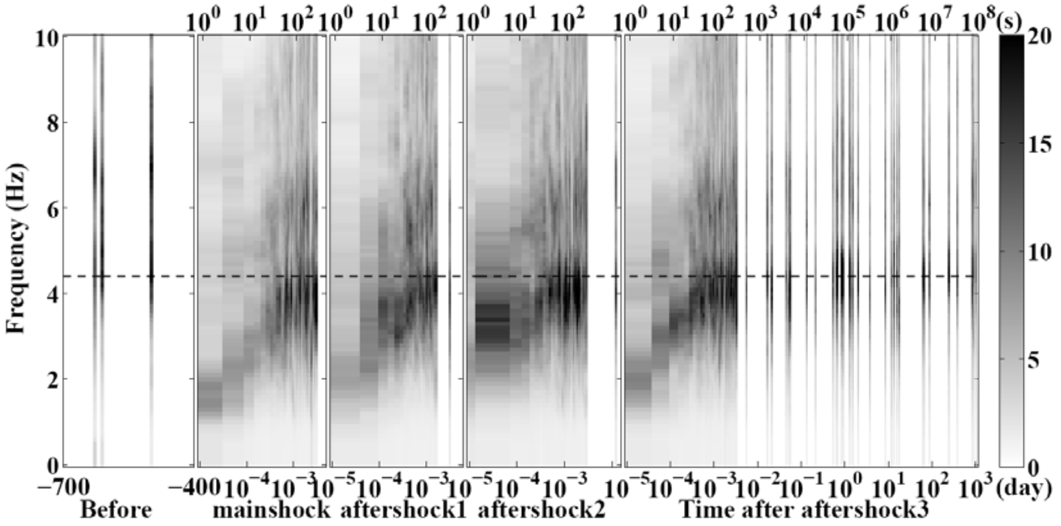

Figure 3.3 Temporal changes of spectral ratio at station NIGH06 during the 2004 Mid-Niigata earthquake sequence. The left bin shows gray-scale-coded spectral ratios for events before the main shock. The middle and right bins show those for the main shock and three aftershocks. Values shown on the top and bottom of the figure indicate lapse times after the main shock and large aftershocks in seconds and in days, respectively. Gaps represent no data. The horizontal black dashed line shows the pre-main shock value of peak frequency.

To better quantify the degree of coseismic change and the time scale of postseismic recovery, I stack the traces of NIGH06 in different time periods. I divide the selected dataset into the following periods: before the main shock, every 0.25 in the logarithmic time after the main shock and three largest aftershocks, and then every 0.5 in the logarithmic time for the following events. I have tested averaging the peaks using slightly different time windows, and the obtained results are similar.

Logarithmic time is used instead of linear time because previous studies have always found a logarithmic recovery process for the observed temporal changes in the shallow crust (Rubinstein & Beroza 2004a, 2005; Schaff & Beroza 2004; Li *et al.* 2006; Peng & Ben-Zion 2006; Sawazaki *et al.* 2006, 2009; Rubinstein *et al.* 2007a; Wu *et al.* 2009b). Next, I identify the peak spectral ratio and peak frequency of the stacked trace in each period (Figure 3.4). The obtained results again show a sudden drop of peak spectral ratio and a shift of the spectral peak to lower frequencies during each large event, followed by logarithmic recovery with time scale of several tens to more than a hundred seconds.

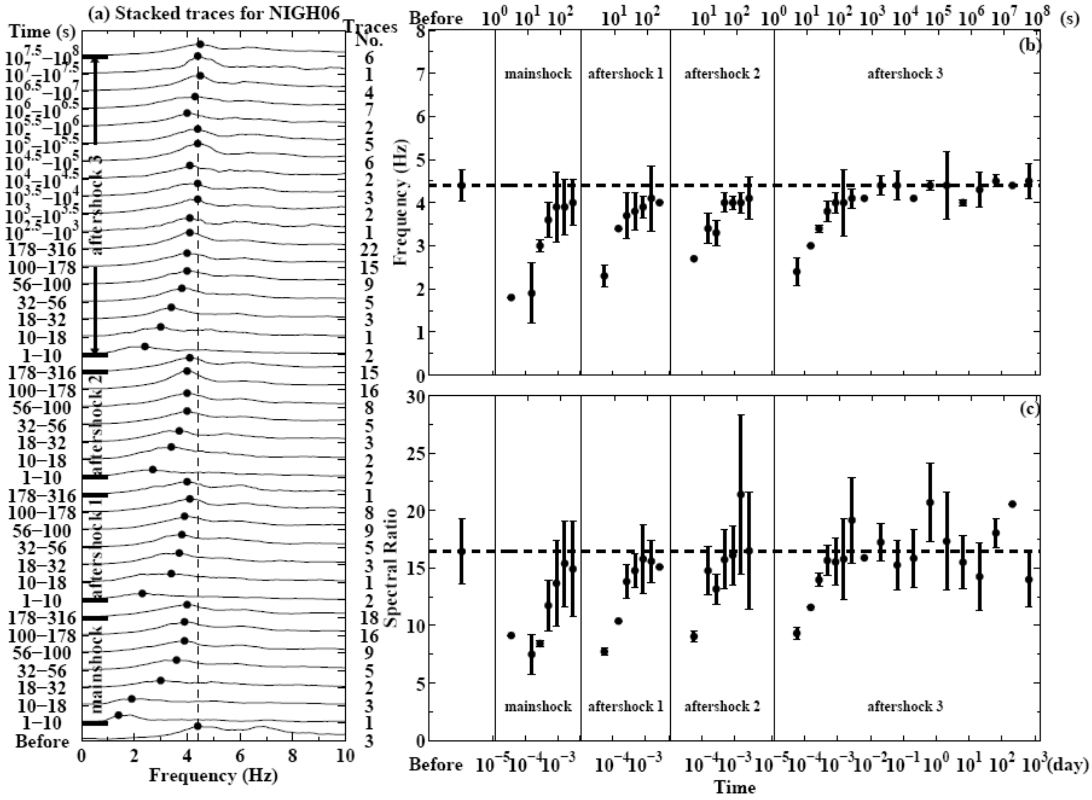

Figure 3.4 (a) Spectral ratios stacked within different time periods at station NIGH06 during the 2004 Mw6.6 Mid-Niigata earthquake sequence. The solid circle marks the

peak spectral value, and the dashed line mark the peak frequency level before the main shock. The time windows and number of traces used to generate each stack are marked on the left and right side, respectively. (b) Peak frequency and (c) peak spectral ratio measured from the stacked spectral ratio traces in (a) before and after the main shock. The vertical solid bar centered at each data point shows the standard deviation. The dashed line indicates the pre-main shock value.

Finally, I examine the relationship between the observed temporal changes and the input ground motion by comparing the percentage of drop in peak frequency, peak spectral ratio, time scale of recovery, and recovery speed with the PGA (Figure 3.5) and peak ground velocity (PGV) (Figure 3.6) for each event. The PGA and PGV for each event are measured from the amplitude of the vector sum of the two horizontal-component ground acceleration and velocity records, respectively. The ground velocity records are obtained by integrating the original acceleration records and then applying a 1-20 Hz Butterworth band-pass filter to remove the DC shift. I use the averaged peak frequency and peak spectral ratio from coda-window-based spectral ratios of the 56 events before the 2004 Mid-Niigata main shock as the reference values. I first calculate the percentage in coseismic reduction for both peak spectral ratio and peak frequency by comparing the 10-s windows immediately after the direct *S*-wave arrivals with the reference values. The recovery time is identified when the values from the sliding 10-s windows recovered to 90% of the reference values. The apparent recovery speed is simply the ratio between the coseismic drop and the recovery time. As shown in Figures 3.5 and 3.6, the coseismic peak frequency, peak spectral ratio drop and the postseismic recovery times roughly scale with the input ground motion when the PGV is larger than 5 cm/s (or PGA is larger than 100

Gal). When the input ground motion is relatively small, the measurements are scattered and do not show a clear relationship with either PGV or PGA. For the events with PGV larger than 5 cm/s (or PGA larger than 100 Gal), I also apply a slightly different technique by fitting a least squares to the sliding-window measurement to obtain the recovery speed first, and then calculating the coseismic drop and recovery time from the recovery speed. I did not apply the least squares fitting to the measurements with the PGV less than 5 cm/s (or PGA less than 100 Gal) due to a lack of enough data points below the reference values. The obtained recovery times from the least squares fitting for events with larger input motions are slightly higher than the previous method, but the general trend with the PGV or PGA remains essentially the same.

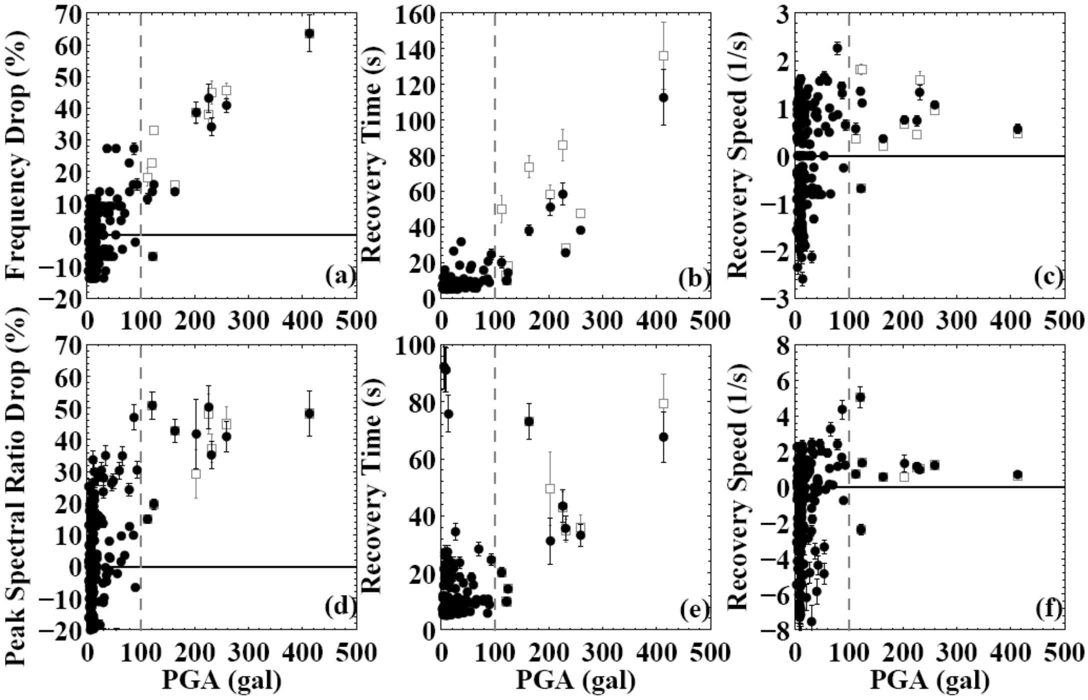

Figure 3.5 (a) Percentage drop of the peak frequency plotted against the peak ground acceleration (PGA) at NIGH06 for all the 235 events. The solid circles mark the values measured from the 10-s windows immediately after the direct *S*-wave arrivals. The open squares show the values calculated from least squares fitting of the sliding-window measurements for events with PGA larger than 100 Gal. The vertical solid bar centered at each data point shows the standard deviation. The horizontal black solid line indicates the pre-main shock value. The vertical grey dashed line marks the PGA value of 100 Gal. (b) Recovery time to the reference peak frequency versus the PGA. (c) Apparent recovery speed of peak frequency versus the PGA. (d) Percentage drop of the peak spectral ratio versus the PGA. (e) Recovery time to the reference peak spectral ratio versus the PGA. (f) Apparent recovery speed of peak spectral ratio versus the PGA.

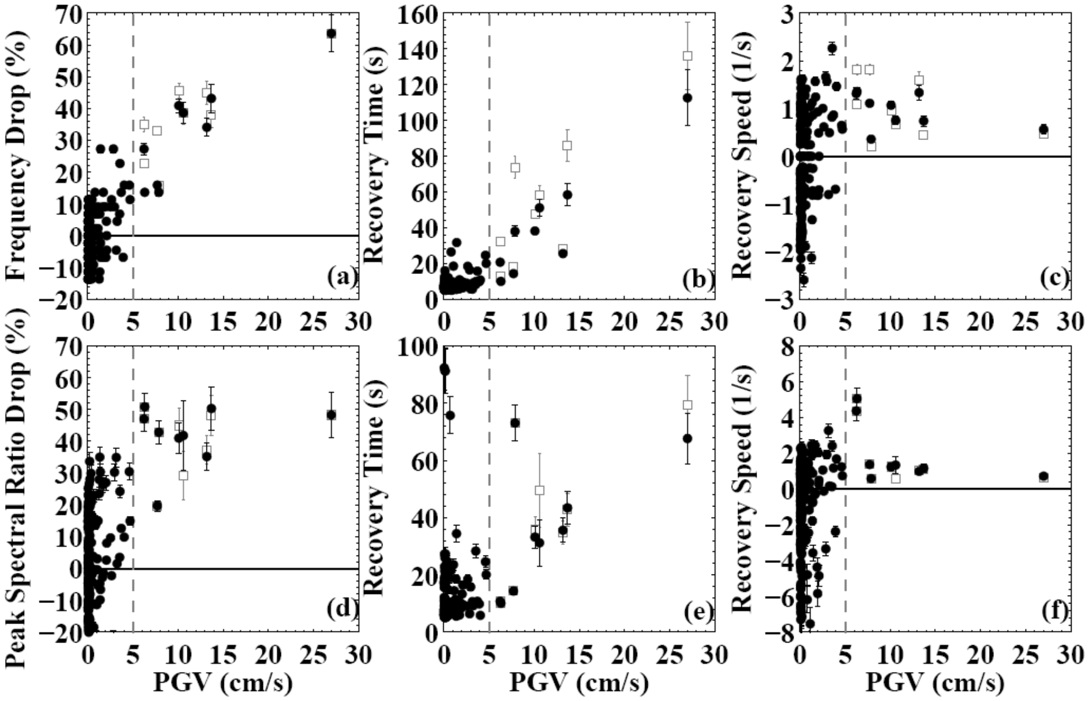

Figure 3.6 Similar plot as Figure 3.5 using peak ground velocity (PGV) as x-axis. The vertical grey dashed line marks the PGV value of 5 cm/s.

3.5 Discussions

3.5.1 Mechanisms

The ground motion recorded at surface stations is a convolution of the source, path, and site effects. The temporal changes of the spectral ratios observed in this study could be caused by changes in the seismic source spectrum, apparent changes produced by varying sources locations, and physical changes occurring during the propagation path and in shallow sediments. As shown in Figure 3.1, the station NIGH06 is not right on top of the aftershock zone. However, because the surface and borehole stations are very close to each other (100 m) as compared to the distances between the earthquake sources and stations (typically more than 10 km), the seismic sources and the propagation path are almost identical for the co-located surface and borehole stations. Hence apparent changes from variable source locations and propagation paths are unlikely to be the main cause of the observed temporal changes.

Temporal changes of material properties within the surface soil layer induced by the strong ground motion of the large earthquakes are likely to be the main origin of the observed variations in the spectral ratios and peak frequencies. The sharp reduction in the spectral ratios and peak frequencies are usually considered as two signatures of *in situ* nonlinear site response during strong shaking (e.g., Field *et al.* 1997; Beresnev *et al.* 1998), which corresponds to a reduction in soil strength and an increase in soil damping observed during earlier laboratory studies (e.g., Seed *et al.*, 1969, 1970).

3.5.2 Dynamic Properties

Assuming a soft soil layer over a half-space bedrock with large impedance contrast (Dobry *et al.* 2000), the fundamental resonant frequency f of the soil layer can be computed by

$$f = \frac{V_s}{4H} = \frac{\sqrt{G/\rho_s}}{4H} \tag{3.1}$$

where V_s, H, G, ρ_s is the S-wave velocity, thickness, shear modulus, and density of the surface soil layer, respectively. According to the NIGH06 site profile provided by KiK-Net, the top two layers are clay with sand from 0-4 m and organic clay from 4-10 m, both with very low S-wave velocities of 100-270 m/s, as compared with the 740 m/s below. Hence, the above assumption is justified. In addition, the fundamental frequency observed from spectral ratios before the 2004 Mid-Niigata earthquake is ~4.4 Hz, which agrees well with the resonance frequency (4 Hz) of the top two layers (i.e., H = 10 m). Hence, I infer that the resonance effect and observed temporal variations in the peak frequencies are mainly constrained in the top 10 m of near-surface layers.

Similarly, the amplification factor (AMP), impedance contrast (I), and damping ratio (ξ) follow the relation (Dobry *et al.* 2000)

$$AMP = \frac{2}{(1/I) + (\pi/2)\xi} \tag{3.2}$$

With the assumption of large impedance contrast, the term $1/I$ could be ignored and the Equation 3.2 could be simplified as

$$AMP = \frac{4}{\pi\xi} \tag{3.3}$$

Finally, I compute the dynamic strain γ as (e.g., Hill *et al.* 1993)

$$\gamma = \frac{PGV}{V_s} \tag{3.4}$$

Using Equations 3.1-3.4, I can relate the observed temporal changes in the peak frequency and peak spectral ratios to changes in the shear modulus G and the material damping ξ, as well as the dynamic strain γ.

The relationship between G/G_0, ξ and γ is shown in Figure 3.7, where G_0 is the average shear modulus measured before 2004 Mid-Niigata earthquake. Although I do not have measurements with higher strains ($\gamma > 0.004$), the modulus degradation and damping ratio curves generally follow typical values for generic clay sites (Vucetic & Dobry 1991; EPRI 1993). As mentioned before, the degree of soil nonlinearity depends both on the material properties and the ground motion characteristics, namely the amplitude and frequency content (e.g., Hartzell 1998; Assimaki *et al.* 2008). Although strong shaking causes physical changes and temporal variations of the material properties under the NIGH06 site, the event intervals are well beyond the maximum recovery time of ~150 s (Figure 3.6b). Hence, the material properties at site NIGH06 are almost recovered to the pre-main shock level when the next event occurs, and could be considered as near identical for all the events analyzed in this study. Therefore, assuming that the site conditions are practically identical for all events investigated, I suggest that the observed variation in the degree of nonlinearity for the Mid-Niigata main shock and aftershocks is likely caused by variations in the amplitude and/or frequency content of the input ground motions.

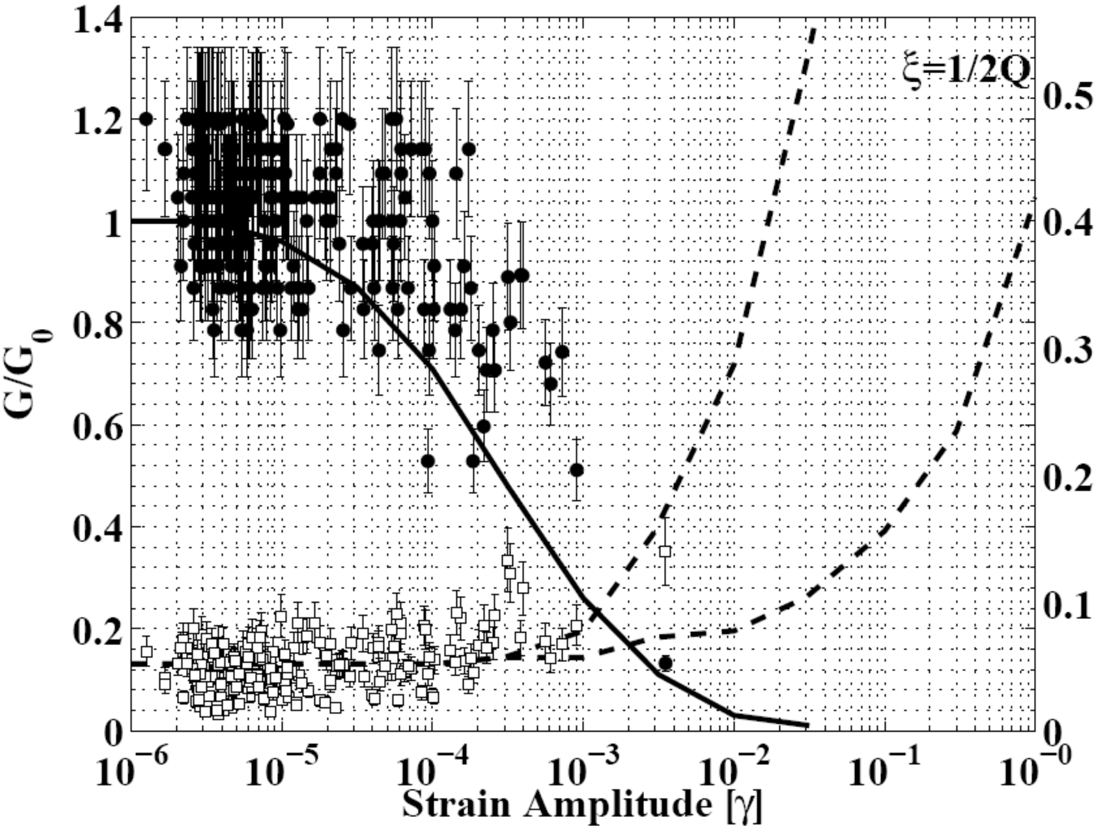

Figure 3.7 Calculated values of modulus degradation *G/G_0* (solid circles) and damping ratio *ξ* (open squares) plotted against the dynamic strains (γ). The vertical solid bar centered at each data point shows the standard deviation. The left and right vertical axis corresponds to the values of *G/G_0* and *ξ*, respectively. The solid and dashed lines show the modulus reduction curve for clay (Vucetic & Dobry 1991), and typical range of damping ratio for clay (EPRI 1993), respectively.

3.5.3 Uncertainties

In this study, I found that the coseismic peak frequency drops, peak spectral ratio drop, and the postseismic recovery time increases as the PGV increases from ~5 cm/s, or the PGA increases from ~100 Gal. Our observations are generally consistent with the 100-200 Gal PGA threshold for soil nonlinearity inferred from previous studies (e.g., Beresnev & Wen 1996a), indicating that input ground motion at a given site plays an important role in controlling the degree of the soil nonlinearity and the recovery process. However, nonlinear effects have been identified in laboratory studies of geo-materials under strains as low as 10^{-8} (TenCate *et al.* 2004), and also *in situ* for a site under PGA of ~35 Gal (Rubinstein 2011). I note that the resolution of the recovery time in this study is somewhat limited by the 10-s window, so the subtle nonlinearity and recovery associated with small events (i.e. PGA less than 100 Gal) could be buried under the averaging effects. Reducing the sliding-window size to smaller values would help to detect the subtle nonlinear site response associated with smaller input ground motions (e.g. Rubinstein 2011).

Recently Lyakhovsky *et al.* (2009) performed theoretical analyses and numerical simulations of the systematic shift of resonance frequencies based on the nonlinear continuum damage model. They found that under a constant material damage, the shift of the resonance frequency with increasing ground motion is only a few percent. However, for increasing material damage, the resonance frequency shift may reach to tens of percent. Here I observed large changes (30-70%) in peak frequencies associated with the strong ground motions of the Mid-Niigata main shock and its large aftershocks. Such a large change in the peak (resonance) frequencies suggests that the increasing ground motion with a constant level of damage itself cannot explain the observed features alone, and an increasing material damage in the near surface layer is needed. This is also consistent with the observations that soft and unconsolidated near-surface sediments are more susceptible to damages caused by strong shaking, resulting in nonlinear site effects and postseismic recoveries (e.g., Rubinstein & Beroza 2005; Sawazaki *et al.* 2009). I note that the maximum time scale of recovery in this study is around 150 s, which also corresponds to the maximum PGV observed during the Mid-Niigata main shock. However, such time scale is still several order of magnitudes smaller than those measured at other KiK-Net site in Japan (Sawazaki *et al.* 2006, 2009) and along the North Anatolian Fault in Turkey (Wu *et al.* 2009b), indicating that different site conditions may cause a larger variability (at least in the postseismic recovery) than the input ground motion at a given site.

So far the mechanisms and the controlling parameters for temporal changes in the near-surface layers and the time scale of recovery are still under investigation. Logarithmic recovery of material damage has been observed by previous studies (e.g., Schaff & Beroza 2004; Peng & Ben-Zion 2006; Sawazaki *et al.* 2006; Wu *et al.* 2009b), and fluids diffusion is suggested to play an important role in the recovery process. Although there is no direct evidence, if the assumption of fluids diffusion holds in our case, the recovery rate would be mainly controlled by the permeability of the site, which could also be associated with amplitude of seismic waves (e.g., Rubinstein & Beroza 2005; Elkhoury *et al.* 2006). On the other hand, laboratory studies also found logarithmic recovery under normal stress due to increasing contact area of crack surfaces or grains for geo-material and sedimentary rocks (Marone 1998; Vakhnenko *et al.* 2005). Since I did not observe a clear relationship between apparent recovery speed and PGV (Figure 3.6c, f), it is likely that the recovery process is much more complicated than a simple process that is solely controlled by the input ground motion. To clarify the physical processes of the recovery, *in situ* measurements of the pore pressures are necessary, and seismic inversion of time-and depth-dependent site properties would also be very helpful (Assimaki *et al.* 2008; Sawazaki *et al.* 2009).

CHAPTER 4

Refined Thresholds for Nonlinear Ground Motion and Temporal Changes of Site Response Associated with Medium Size Earthquakes

4.1 Introduction

As mentioned in previous chapters, nonlinear site response is associated with deviations from the linear trend predicted by Hooke's elasticity when the amplitude of ground motion exceeds a certain threshold. This phenomenon is well documented in both laboratory experiments (Ostrovsky & Johnson 2001, and references within) and under *in situ* conditions (Beresnev & Wen 1996a, and references within). Generally, nonlinear response has a strong correlation with the level of ground motion (e.g. Hartzell 1998; Su *et al.* 1998; Johnson *et al.* 2009) along with rock type and other characteristics of the sites (e.g. Beresnev & Wen 1996a; Hartzell 1998; Trifunac *et al.* 1999; Tsuda *et al.* 2006). Quantification of soil nonlinearity and subsequent consequences for site response are currently key components of estimating seismic hazard, predicting future ground motions (Frankel *et al.* 2000), and designing geotechnical and structural engineering systems on soils (NEHRP 2003).

Comparisons of the site response during strong and weak ground motions provide one of the most typical ways to identify nonlinear site behavior. Several recent studies have also investigated details of the recovery process from nonlinear response by computing the temporal evolution of spectral ratios between a target site and a nearby reference site (e.g. Pavlenko & Irikura 2002b; Sawazaki *et al.* 2006, 2009; Karabulut & Bouchon 2007; Wu *et al.* 2009a, b; Rubinstein 2011). These studies generally identify strong reductions of peak frequencies (i.e. resonant frequencies) measured in the spectral ratios during the strong ground motions of a nearby large earthquake, followed by logarithmic recoveries to the level before the large event. The time scales of the recoveries observed in these studies are quite different. In some cases, the coseismic changes appear to recover on timescales of minutes or less (e.g. Pavlenko & Irikura 2002b; Karabulut & Bouchon 2007), while in other cases the recoveries appear to last for years (e.g. Sawazaki *et al.* 2006). Some of the documented differences may stem from different analysis resolutions, but they may also reflect (at least partially) different types of nonlinear behavior.

4.1.1 Two Forms of Nonlinear Behavior

Lyakhovsky *et al.* (2009) analyzed theoretically the response of a solid governed by a nonlinear damage rheology and highlighted the existence of two forms of nonlinear behavior. With fixed existing material damage, the nonlinear effects are small and the recovery to linear behavior with reduction of source amplitude is instantaneous. When the source motion leads to increasing material damage, the nonlinear effects are considerably larger and the recovery to linear behavior after the source ceases to operate is logarithmic with time. Both forms of nonlinear response of materials to loading are seen clearly in high resolution laboratory experiments

(Pasqualini *et al.* 2007).

4.1.2 Thresholds of Near Surface Nonlinearity

Because nonlinear effects tend to be clear particularly under strong shaking, most of the previous observational seismological studies on this topic focused on large earthquakes (typically larger than Mw6). They found that nonlinear site response typically manifests beyond an amplitude threshold of 100-200 Gal or dynamic strain of 10^{-5} to 10^{-4} (e.g. Beresnev & Wen 1996a). On the other hand, laboratory studies identified nonlinear effects for geomaterials under strains as small as 10^{-8} (TenCate *et al.* 2004). Using repeating earthquakes, Rubinstein and Beroza (2004b) found reduction of *S*-wave velocities in the near surface (which could be used as a proxy for resonant frequency) after a Mw5.4 aftershock of the 1989 Mw6.9 Loma Prieta earthquake. Recently, Rubinstein (2011) used the spectral ratio method to analyze strong ground motion recordings of 13 earthquakes with magnitudes of 3.7-6.5 (including the 2003 Mw6.5 San Simeon earthquake, 2004 Mw6.0 Parkfield earthquake and their aftershocks). He found that at the Turkey Flat site, ~35 Gal of PGA produces nonlinear site effects, suggesting that nonlinear effects could be much more common than previously thought.

In Chapter 3 (Wu *et al.* 2009a), I quantified the effects of the input ground motion on the degree of nonlinearity by applying the spectral ratio method to the strong motion data recorded by a pair of surface and borehole stations before, during, and after the 2004 Mw6.8 Mid-Niigata earthquake sequence. I found that the coseismic peak frequency reduction and the postseismic recovery time increase with the peak ground velocity (PGV) beyond ~5 cm/s, or PGA beyond ~100 Gal. I were unable to identify clear coseismic drop and postseismic recovery with PGA less than 100 Gal, mainly because of averaging effects associated with the employed 10-s sliding-window. I noted that by reducing the sliding-window size to smaller values, it may be possible to detect more subtle nonlinear site response associated with smaller input ground motions.

In this Chapter, I apply the sliding-window spectral ratio method with a small window size to the strong motion data generated by ~2000 medium-size earthquakes recorded by 6 pairs of surface and borehole stations (Figure 4.1). These include the data analyzed previously by Wu et al. (2009a), together with a few sites that have shown nonlinear responses by other recent studies (Sawazaki *et al.* 2006, 2009; Assimaki *et al.* 2008). Because I have more than 2000 seismic records, I am able to stack the spectral ratios for corresponding PGA values, which result in stable measurements. Our analysis shows that the peak frequency starts to decrease at PGA levels of several tens of Gal, followed in some cases by a near instantaneous recovery. When the PGA values exceed ~60 Gal to more than 100 Gal, the onset of nonlinear response is followed by a gradual recovery. The two different observed forms of nonlinear behavior for different ranges of excitation levels are consistent with the theoretical expectations based on the damage model of Lyakhovsky *et al.* (2009) and the laboratory observations of Pasqualini *et al.* (2007). The low thresholds for the onset of *in situ* nonlinear effects, documented in this work and the study of Rubinstein (2011), imply that nonlinear models should be considered for smaller earthquakes than previously thought (e.g. Kramer & Paulsen 2004).

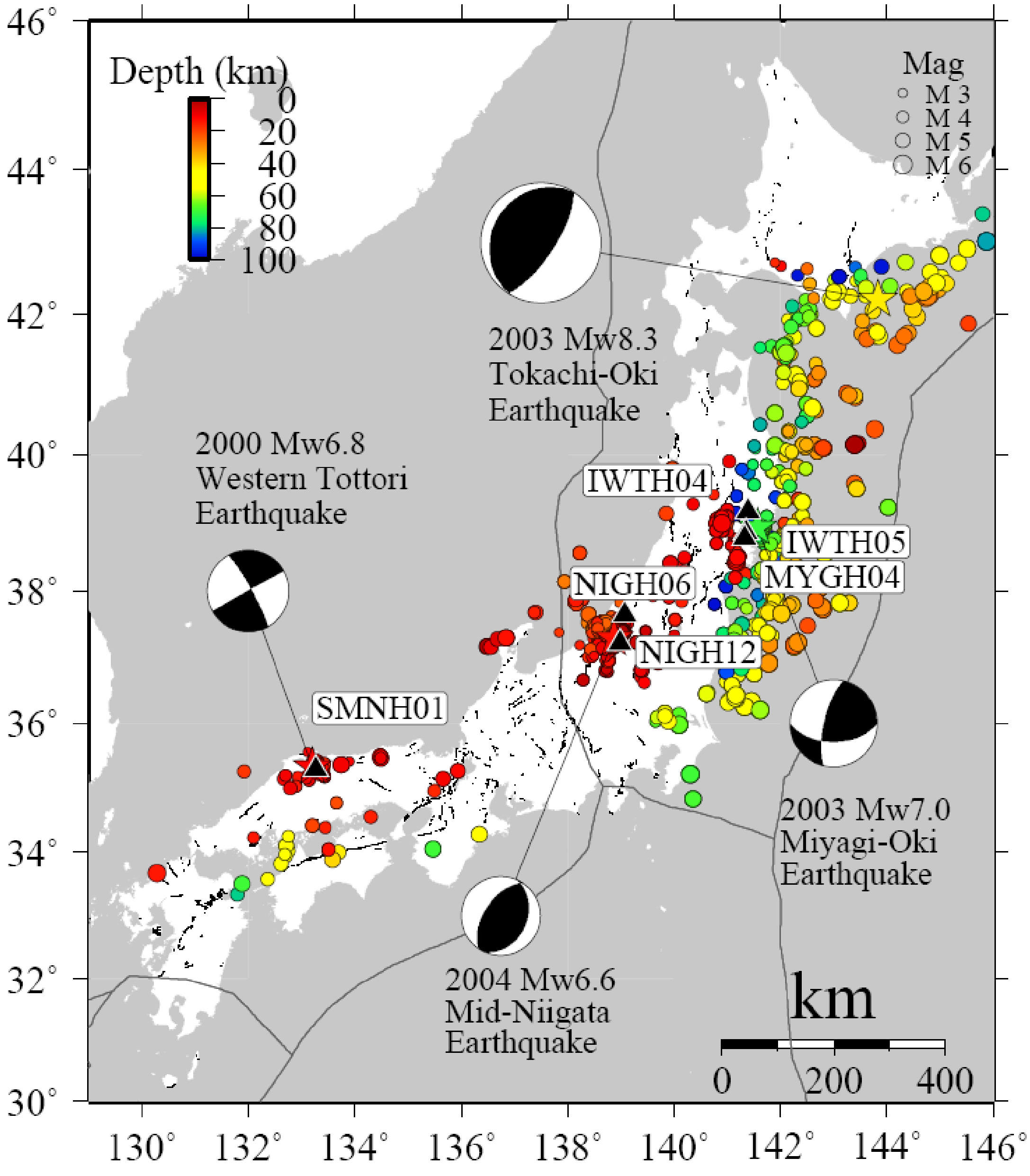

Figure 4.1 Map of the study region in Japan. Epicenters of the 2000 Mw6.8 Western Tottori earthquake, 2003 Mw8.3 Tokachi-Oki earthquake, 2003 Mw7.0 Miyagi-Oki earthquake, and 2004 Mw6.6 Mid-Niigata earthquake are shown in stars together

with their moment tensor solution. Other events are shown in circles. The size of circle indicates the magnitude of each event and color shows the depth with red being shallow and blue being deep. Locations of the 6 KiK-Net stations used in this study are shown in black triangles. The black lines show the active faults in this region and the grey lines denote the subduction plate boundaries.

4.2 Seismic Data

The analysis employs strong motion data recorded by 6 stations (MYGH04, NIGH06, NIGH12, SMNH01, IWTH04, IWTH05) in the Japanese Digital Strong-Motion Seismograph Network KiK-Net operated by the National Research Institute for Earth Science and Disaster Prevention (Aoi *et al.* 2000).

The 6 stations used in this study are chosen mainly because previous studies have identified clear nonlinear effects at these stations during large events (Sawazaki *et al.* 2006, 2009; Assimaki *et al.* 2008; Wu *et al.* 2009a). I also find that the observed temporal changes in peak frequencies and peak spectral ratios (maximum of the spectral ratios) at these stations are much clearer than those at other stations, allowing us to better detect potential temporal changes associated with relatively small ground motions. Additional details on the network and site conditions can be found in Table 4.1, Figure 4.2, or at the KiK-Net website (http://www.kik.bosai.go.jp/kik/index_en.shtml).

Table 4.1 List of events with date/time, magnitude (Ma), latitude, longitude, depth (km), PGA (Gal), PGV (cm/s), Peak Frequency Drop (%), Peak Frequency Recovery Time (s), Peak Spectral Ratio Drop (%), and Peak Spectral Ratio Recovery Time (s).

Station	Lon.	Lat.	V_{S30} (m/s)	Site Classification
MYGH04	141.33	38.78	804	B
NIGH06	139.07	37.64	304	D
NIGH12	138.99	37.22	540	C
SMNH01	133.26	35.29	349	D
IWTH04	141.39	39.18	415	C
IWTH05	141.35	38.86	375	C

Max V_S Contrast	Soil Types	Nonlinearity Threshold (Gal)
4.36	filling, slate	25
2.74	clay, organic clay, gravel	25
2.08	gravel, cobble stone, sand	25
2.18	filling, silt, gravel, boulder	15
2.77	sandy clay, fine sand, sandy silt	85
2.19	hornblende, biotite, tonalite	55

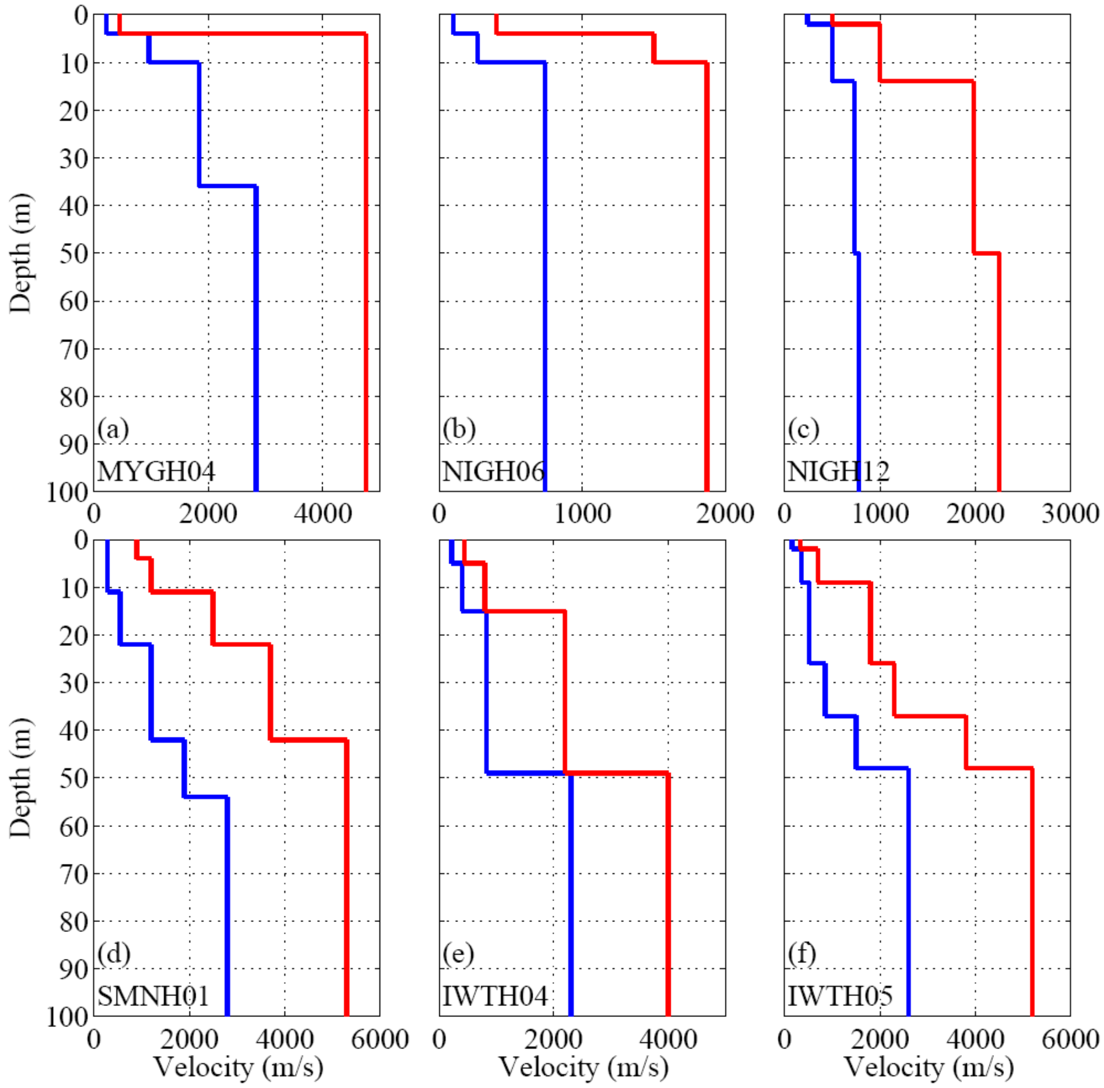

Figure 4.2 V*p* (red lines) and V*s* (blue lines) profiles for the 6 sites utilized in this study.

In the subsequent analysis I utilize a total of 2204 events that occurred between January 1999 and May 2008 and recorded by the 6 surface and borehole strong motion sensors. The magnitudes of most events range from 3 to 5, and the hypocentral depths range from 5 to 70 km. The recorded PGAs of most events range from 0 to 100 Gal, generally less than the 100-200 Gal threshold for nonlinear site effects suggested by previous studies (e.g. Chin & Aki 1991; Beresnev & Wen

1996a).

4.3 Analysis Procedure

The analysis procedure follows overall those of Sawazaki *et al.* (2006, 2009) and Wu *et al.* (2009a). The main analysis steps are as follows. I use 6-s time windows that are moved forward by 2s for all waveforms recorded by the surface and borehole stations. The zero time corresponds to the hand-picked *S*-wave arrival, and I use the time corresponding to starting point of each window to denote the time of that window. In such case, the window corresponding to the *S*-arrival window (i.e. zero time) fully captures the strongest motion during the *S*-wave. I have tested various window lengths and sliding values. Our testing results indicate, as noted by Wu et *al.* (2009a), that increasing window length would miss the temporal changes over small time scales. On the other hand, decreasing window length would reduce the stability of the results. The employed 6-s window appears to be a well-balanced value for the examined data between temporal resolution and stability. All possible seismic phases, including pre-event noise, *P*, *S* and coda waves are analyzed together. Next, I remove the mean value of the traces and apply a 5 per cent Hanning taper to both ends. I compute the Fourier power spectra of the two horizontal components and take the square root of the sum to get the amplitude of the vector sum of the two horizontal spectra. The obtained spectra are smoothed by applying the mean smoothing algorithm from the subroutine “smooth” in the Seismic Analysis Code (Goldstein *et* *al.* 2003), with half width of 0.5 Hz. I tested different smoothing window sizes, and found that smoothing window with half width of 0.5 Hz could remove most of the noisy spikes while not changing the overall shape of spectra significantly. The spectral ratios are obtained by dividing the combined horizontal spectra of surface stations by the spectra of the borehole stations.

Figure 4.3 shows an example of the original acceleration records at NIGH06 generated by an M5.3 event on 10/25/2004 and the 6-s windows used to compute the spectral ratios for the direct *S* and coda waves. By comparing the spectral ratios, I identify a clear shift of resonant frequency around 4 Hz to lower values and a drop in peak amplitude for the direct *S* waves (Figure 4.3c). Both of these features are hallmarks of nonlinear site effects (e.g. Beresnev & Wen 1996a).

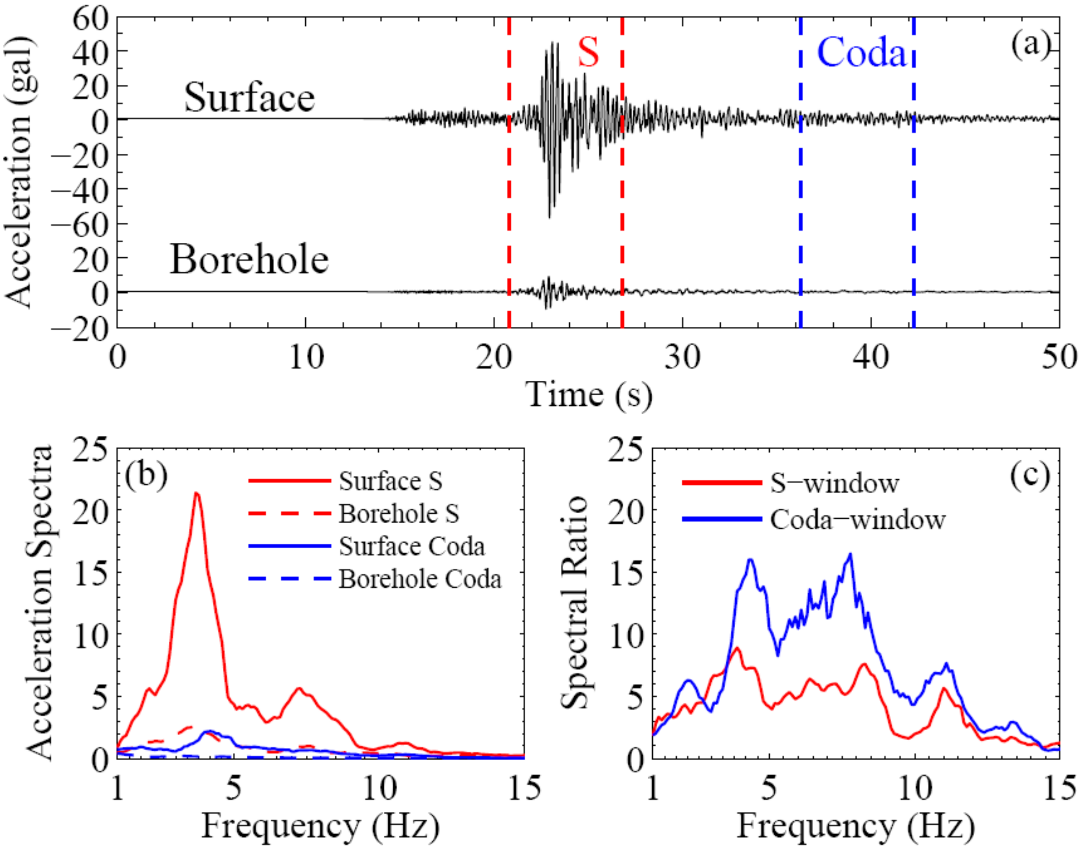

Figure 4.3 (a) East-component ground accelerations recorded at the station NIGH06 generated by an M5.3 earthquake on Oct 25, 2004. Surface recording is shown at the top and borehole recording is shown at the bottom. The red and blue dashed lines indicate the direct *S* and coda window that are used to compute the acceleration spectra in (b) and spectral ratios in (c).

4.4 Results

After processing all the data, I obtain 137980 spectral ratios, including 2204 spectral ratio traces for the direct *S*-windows. First I sort all the traces for each station by their PGA and stack them in different PGA ranges (0-500 Gal with an increment of 1 Gal). The PGA for each trace is measured from the amplitude of the vector sum of the two horizontal-component ground acceleration records within the 6-s window.

Then I identify the peak spectral ratios and peak frequencies for the stacked traces. Figure 4.4 shows all the spectral ratio traces against the corresponding PGAs for the 6 stations. A general pattern is that the peak frequency drops to lower values when the PGA is between 10 and 100 Gal, although the actual threshold varies for different stations and it is hard to quantify by visual inspection. In addition, the spectral ratio traces in such plots have different seismic phases and contain both the peak motion in each seismogram (which may produce nonlinearity) as well as the following weaker motion (at which time the site response may be associated with a recovery process).

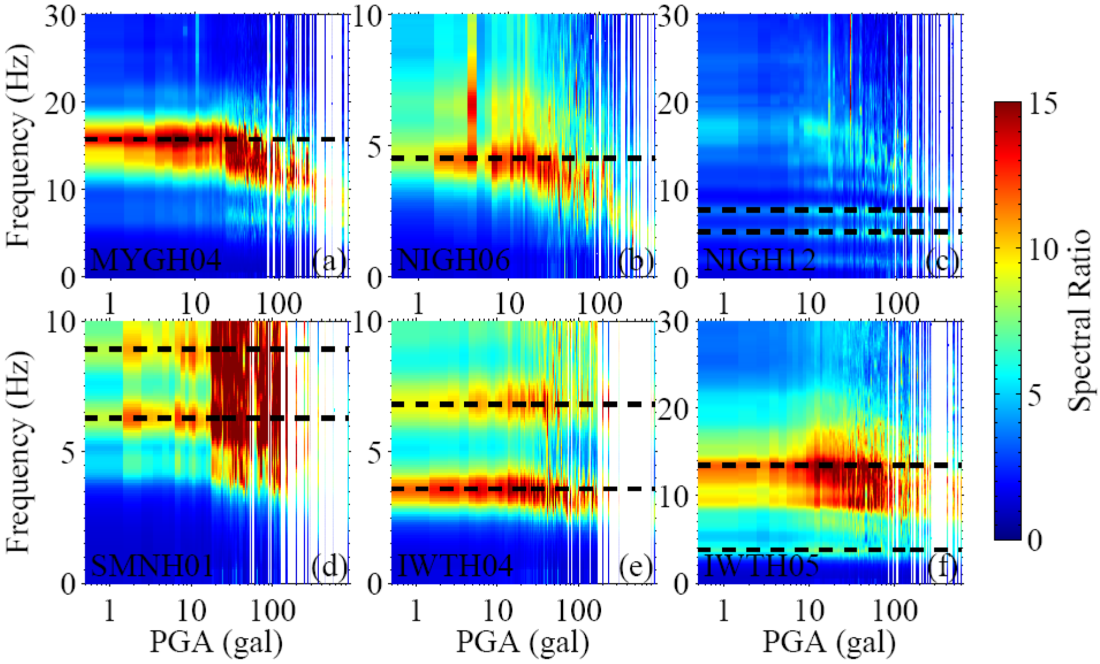

Figure 4.4 Stacked spectral ratios from all the 6-s windows plotted against PGA for the 6 stations (a-f). All the spectral ratio traces for each station are stacked based on the PGA of each sliding window from 0 to 1000 Gal with a step of 1 Gal. The x-axis shows the PGA value in log scale, and the y-axis shows the frequency. The spectral ratio value are color-coded with red being high and blue being low. Gaps represent no data. The horizontal dashed lines indicate the resonance frequencies without nonlinearity measured from 0-10 Gal.

To better quantify the degree and process of nonlinear response in the spectral ratios for the medium-size events, I select data with PGA less than 100 Gal and focus on the temporal evolutions of the spectral ratios before, during and after the direct *S* waves (which generally have the largest amplitude of all the seismic phases for medium-size events). I group the events in different PGA ranges (0-100 Gal with an increment of 10 Gal) and stack the spectral ratio traces from 12 s before to 60 s after the *S*-wave arrival time within each group. As before, I tested stacking the trace using different PGA ranges, and the obtained results are similar. Next, I identify the peak spectral ratio and peak frequency for the stacked trace in each PGA range. Figure 4.5 illustrates the procedure for data recorded at site NIGH06. The results show again a sudden drop of peak spectral ratio and a shift of the spectral peak to lower frequencies during the *S*-wave arrival, and these changes become clear when the PGA exceeds certain threshold. Similar analyses using data at the other sites indicate that the threshold varies from ~20 to ~80 Gal among the different stations, and the degree of nonlinearity (i.e. percentage drop of peak frequency) also varies for different stations.

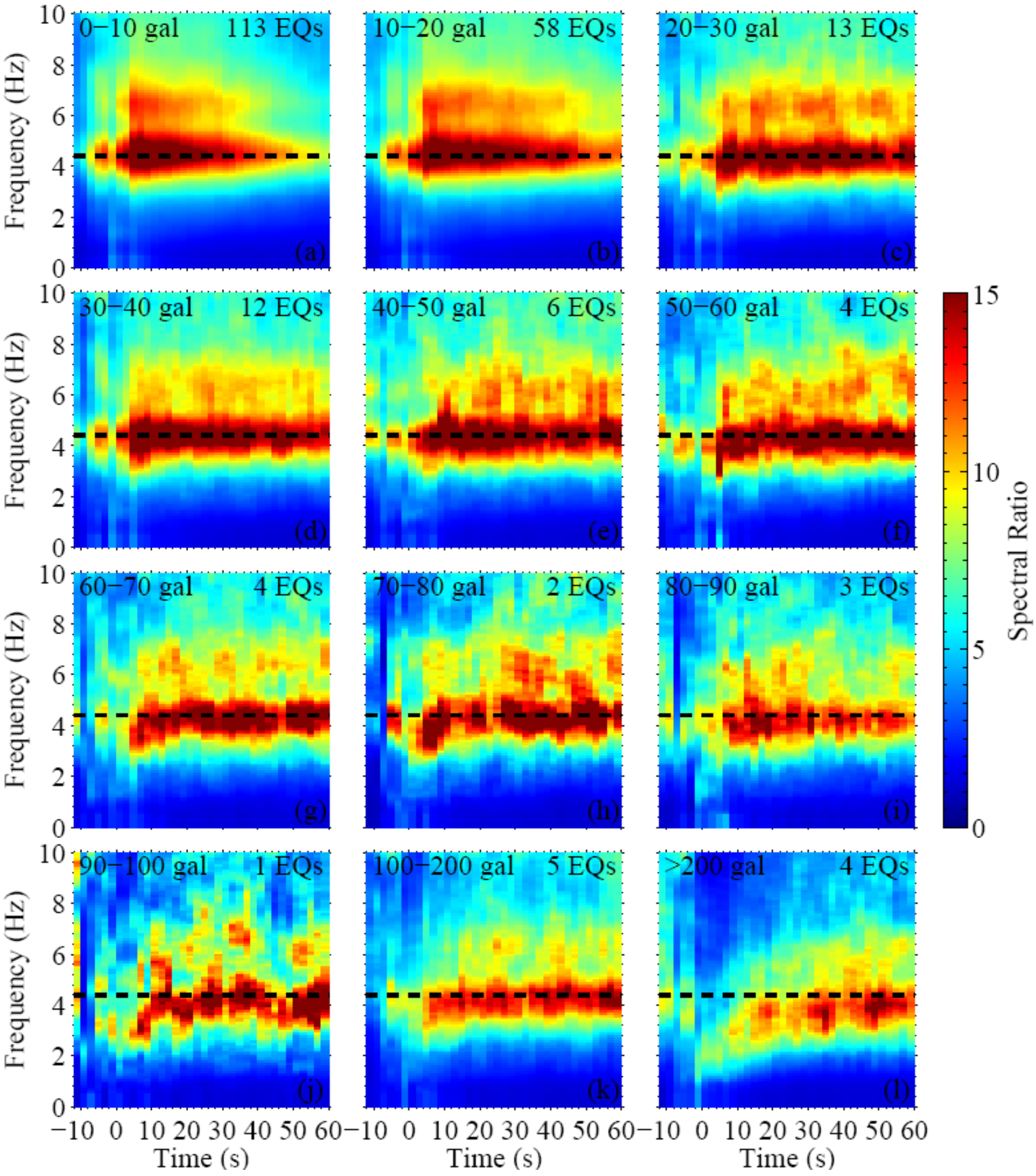

Figure 4.5 Stacked spectral ratios for station NIGH06 plotted against the travel time relative to the *S*-wave arrival. Spectral ratio traces from 12 s before to 60 s after the *S*-wave arrival are stacked based on the PGA of that event from 0 to 100 Gal with a step of 10 Gal (a-j). I also include the results between 100-200 Gal and >200 Gal for comparison (k-l). The spectral ratio value are color-coded with red being high and blue being low. The PGA range and number of the stacked events are marked at the left and right side on the top of each panel. The horizontal dashed lines indicate the reference resonance frequency of 4.4 Hz.

Using the obtained results, I examine the relationship between the observed temporal changes and the input ground motion, by relating the percentage of drop in peak frequency and peak spectral ratio with the PGA range for the stacked traces. I use the measured peak frequency and peak spectral ratio for the stacked trace in the PGA range 0-10 Gal as the reference values. To test the validity of the reference value, I have compared the stacked spectral ratio trace in the PGA range of 0-10 Gal with those traces from low-amplitude coda-windows, and found that they are nearly identical (Figure 4.6a). I also checked individual spectral ratio traces in the PGA range of 0-10 Gal, and found no significant variation in peak frequency (Figure 4.6b).

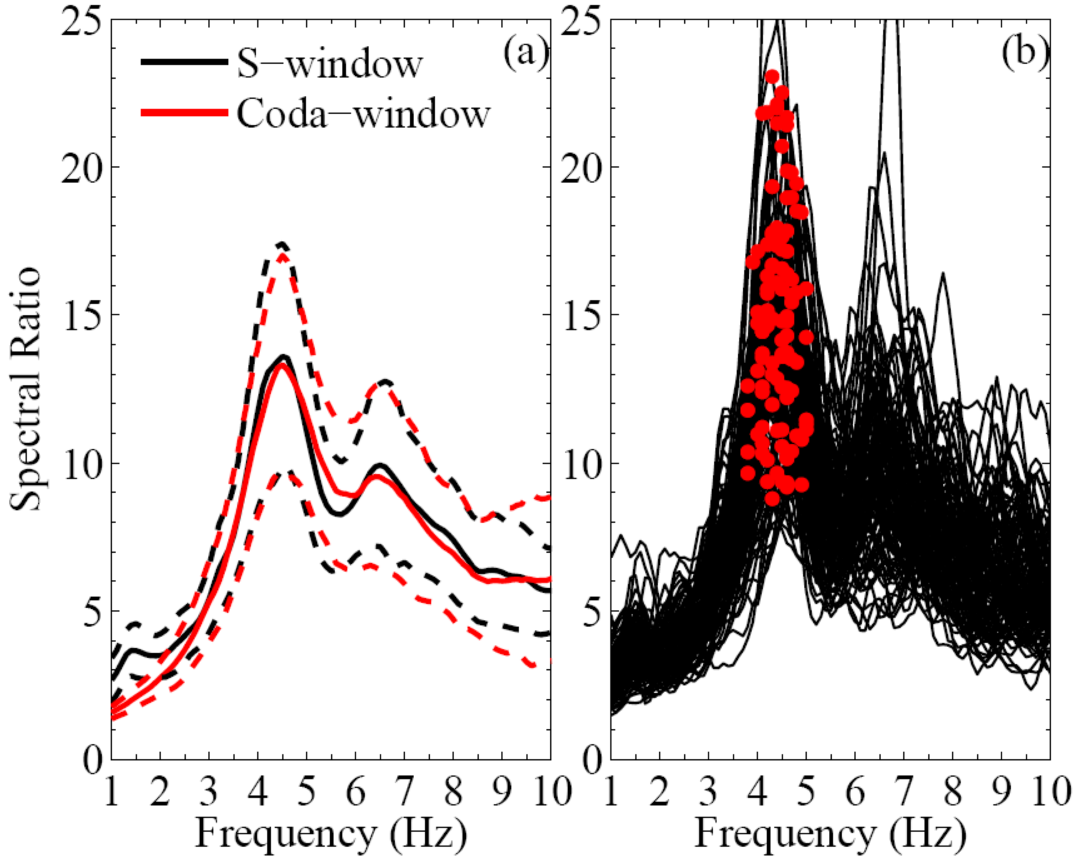

Figure 4.6 (a) Comparison of the stacked spectral ratios at station NIGH06 from the

direct-*S* windows (black) and the *S*-coda windows (red) for all the events in the PGA range of 0-10 Gal. The solid and dashed lines show the average spectral ratios and the standard deviations. (b) The spectral ratio traces from the direct-*S* windows used to generate the black solid line in (a). The red dots mark the lower resonance peaks of the spectral ratios.

I calculate the percentage reduction for both peak frequency and peak spectral ratio associated with the *S* waves, by comparing the 6-s windows immediately after the *S*-wave arrivals with the reference values. The peak frequency drop (PFD) and peak spectral ratio drop (PSRD) are defined by

$$PFD = (f_r - f_s)/f_r \tag{4.1}$$

$$PSRD = (PSR_r - PSR_s)/PSR_r \tag{4.2}$$

where f_r and PSR_r are the reference peak frequency and peak spectral ratio, respectively, and f_s and PSR_s are the peak frequency and peak spectral ratio measured at the 6-s window immediately after the *S*-wave arrival, respectively. Because the degree of nonlinearity is site specific, I use 10% of the peak frequency drop or peak spectral ratio drop measured in the PGA range of 90-100 Gal for each station as the threshold to judge whether nonlinearity occurs. Then I repeat the process for other resonance peaks if available. The measured PGA threshold of nonlinearity varies (Figure 4.7) from ~20 to ~80 Gal among all the stations. Figure 4.7 also shows that the percentage of drop in peak frequency starts to increase with PGA higher than the threshold for each station. As previous studies (Wu *et al.* 2009a, b) suggested, the uncertainty for peak spectral ratio is much larger than that for peak frequency (see also Figure 4.6b). I am able to identify systematic drop of peak spectral ratio only for two stations MYGH04 and NIGH06 (Figure 4.8). For the other 4 stations there is no clear correlation between the percentage of drop in peak spectral ratio and PGA, probably due to the large uncertainties. Because of this, I focus in the discussion on the temporal changes in peak frequency.

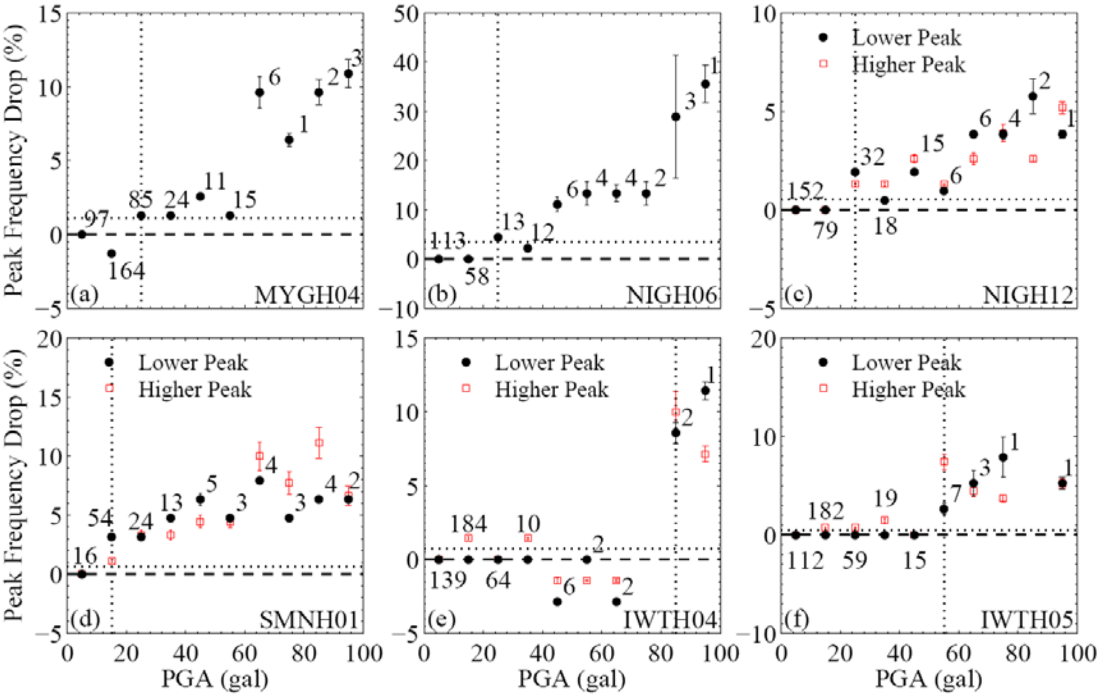

Figure 4.7 Percentage drop of the peak frequency plotted against the PGA for the 6 stations (a-f). The black solid circles and red open squares mark the values measured from the 6-s windows immediately after the direct *S*-wave arrivals for the lower and higher resonance peaks, respectively. The vertical solid bar centered at each data point shows the standard deviation, with the number of stacked events by its side. The horizontal dashed line indicates the zero level. The horizontal dotted line marks 10% of the value measured at 90-100 Gal. The vertical dotted line marks the inferred PGA threshold of nonlinearity. The station name is marked at the bottom-right corner of each panel.

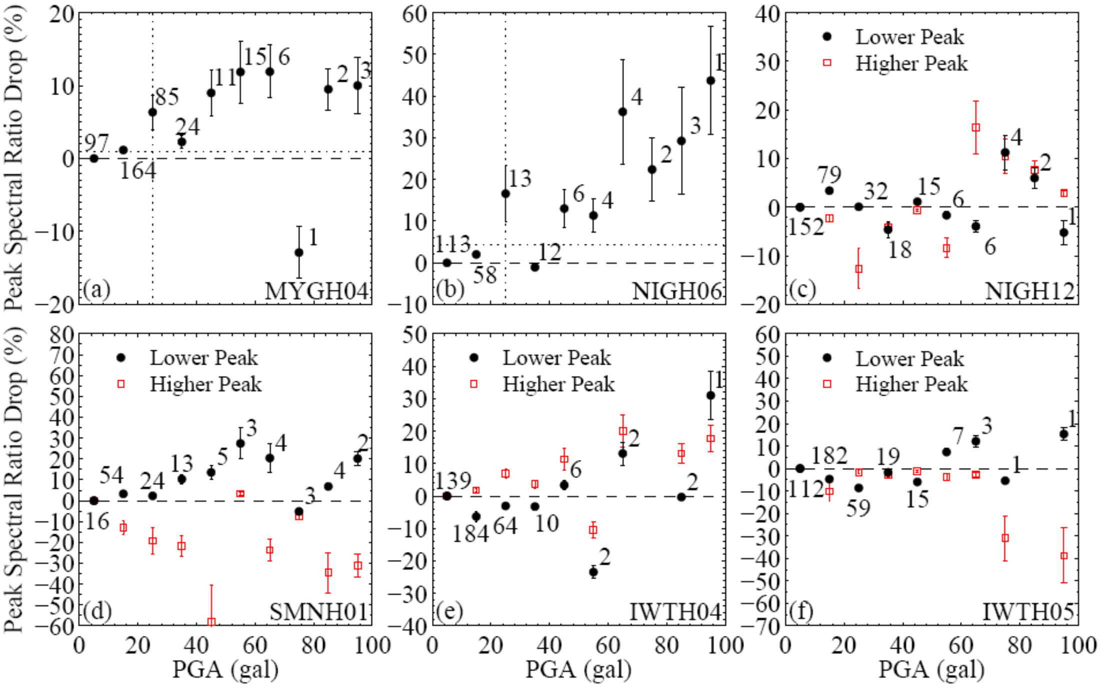

Figure 4.8 Similar plot as Figure 6 for percentage drop of the peak spectral ratio.

4.5 Discussions

To relate the observed temporal changes in surface-to-borehole spectral ratios with nonlinear site response, the following conditions need to be satisfied: 1. the source spectrum should be identical for the station pair; 2. the propagation path should also be the same for the station pair; 3. the reference site should have no significant site response, and 4. the reference spectra should be stable over time. Because the surface and borehole stations are very close to each other (on the order of 100 m) as compared to the distances between the earthquake sources and stations (typically more than 5 km), the seismic sources and the propagation path are almost identical for the co-located surface and borehole stations. Hence their source and path terms are effectively cancelled by taking the spectral ratio and the first and second conditions are satisfied. I also examined the spectra of borehole stations and found no significant peaks or troughs, and no clear variation over time, so the third and fourth conditions are also satisfied to a very good approximation.

Nonlinear site effects (i.e. reduction of shear modulus and increased damping) induced by strong motions of medium-size earthquakes are likely to be the main origin of the observed variations in the peak frequencies and peak spectral ratios (e.g. Pavlenko & Irikura 2002b; Sawazaki *et al.* 2006, 2009; Karabulut & Bouchon 2007; Wu *et al.* 2009a, b; Rubinstein 2011). Assuming a soft soil layer over a half-space bedrock with large impedance contrast (Dobry *et al.* 2000), the fundamental resonant frequency f of the soil layer can be computed by Equation 3.1. From the site profiles (see the KiK-Net website), I found significant velocity contrast between the near-surface layers and the underlying bedrocks for the 6 stations, so the aforementioned assumption is justified. Using Equation 3.1, together with the velocity and layer thickness values from the site profiles, I compute fundamental resonance frequencies of 13.8 Hz, 4 Hz, 7.7 Hz, 6.6 Hz, 2.8 Hz, and 3.2 Hz for the top layers where strongest velocity contrast occurs at stations MYGH04, NIGH06, NIGH12, SMNH01, IWTH04, IWTH05, respectively. The computed resonance frequencies agree reasonably well with the observed values of 15.7 Hz, 4.4 Hz, 7.7 Hz, 6.3 Hz, 3.5 Hz, and 3.8 Hz from the spectral ratios without significant nonlinear effects (i.e. in the PGA range of 0-10 Gal). Hence I infer that the observed nonlinear effects are mainly constrained within the top few tens of meters for the 6 sites.

4.5.1 Refined Thresholds of Nonlinearity

As mentioned, the results of Figure 6 indicate that the peak frequency starts to decrease when the PGA is on the order of several tens of Gal, above which there is a clear correlation between the percentage of drop in peak frequency and PGA level. These observations, together with the results of previous studies (e.g. Hartzell 1998; Su *et al.* 1998; Johnson *et al.* 2009; Wu *et al.* 2009a), support the view that nonlinear effects strongly correlate with the level of ground motion. However, the ~20-30 Gal PGA threshold revealed by our analysis is lower than the value of 100-200 Gal found by most previous studies (e.g. Beresnev & Wen 1996a). This is perhaps not too surprising, because as far as I know none of the previous studies except the recent work by Rubinstein (2011) investigated nonlinear site effects with PGA less than 100 Gal (typically associated with medium-size events). The nonlinear effects with PGA less than 100 Gal are generally much weaker than the traditional nonlinear site effects associated with stronger shaking (Figure 4.9b). Since most previous studies mainly focused on individual events (rather than stacked data), the subtle nonlinear effects are quite likely to be buried by low signal-to-noise ratio (SNR). From the comparison of our results (Figure 4.9b) with the results of Wu *et al.* (2009a) without stacking (Figure 4.9a), I could see a clearer image of the peak frequency drop in the PGA range of 0-100 Gal after stacking. Hence, the stacking technique utilized in this study helps to reveal the otherwise buried small nonlinear effects in a statistical way.

However, stacking requires a significant amount of strong motion recordings, which was not available until the last decade. In addition, reducing the sliding-window size from 10 s to 6 s helps to identify subtle co-seismic changes associated only with the direct *S*-waves, which also causes some differences in the results for PGA > 100 Gal (Figure 4.9).

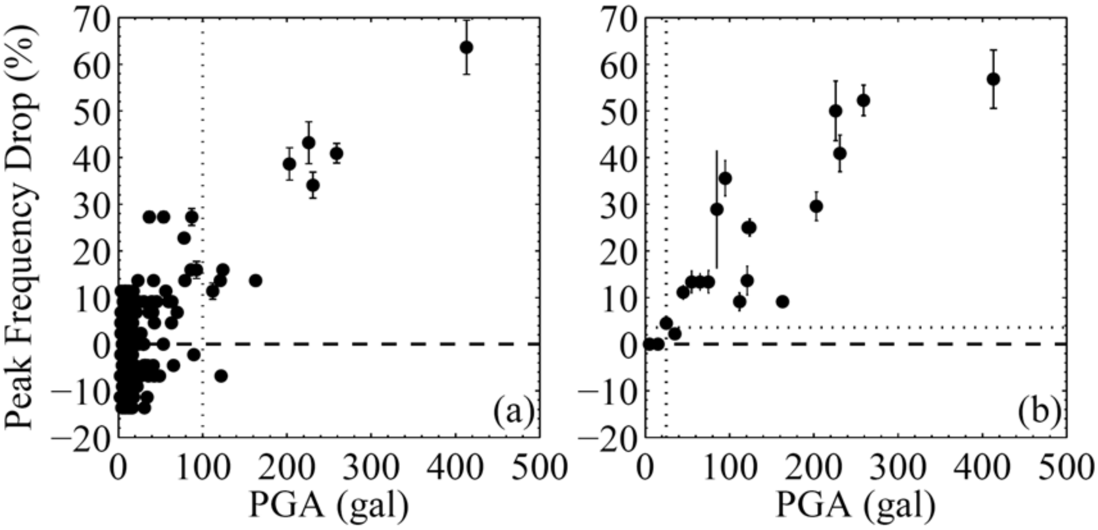

Figure 4.9 (a) Percentage drop of the peak frequency measured from 10-s windows plotted against the PGA at NIGH06 from Wu *et al.* (2009a). The solid circles mark the values measured from the 10-s windows immediately after the direct *S*-wave arrivals. The vertical solid bar centered at each data point shows the standard deviation. The horizontal dashed line indicates the pre-main shock value. The vertical grey dotted line marks the PGA value of 100 Gal. (b) Similar plot as (a) for 6-s windows. Values below 100 Gal are measured from the stacked spectral ratio traces (Figure 6b), and values above 100 Gal are measured from individual even. The horizontal dotted line marks 10% of the value measured at 90-100 Gal. The vertical dotted line marks the inferred PGA threshold of nonlinearity.

The peak frequency drops found in this study for PGA < 100 Gal are typically within the duration of the *S*-wave (e.g. Figure 4). In some cases (e.g. 60-70, 70-80, 90-100, > 200 Gal), I can identify the logarithmic type of recovery found by various previous studies (e.g. Sawazaki *et al.* 2006; Wu *et al.* 2009a). However, such recovery is not clear in other cases with lower PGA values. One possible explanation is that the observed weak nonlinear effects are induced in damaged rocks by increasing wave amplitude *without* causing additional material damage. This is consistent with the analytical and numerical results of Lyakhovsky *et al.* (2009) for a continuum nonlinear damage rheology model. The results from that study show a few percent shift in the resonance frequency with increasing ground motion at a constant damage level, and tens of percent shift in the resonance frequency with increasing damage level. These two forms of nonlinear effects are observed clearly in the laboratory experiments of Pasqualini *et al.* (2007).

Based on the results of Figure 4.7, the percentage of drop in peak frequency is generally very small (< 5%) at the onset of nonlinearity, except for station IWTH04. At this station, the point between 60 and 70 Gal is missing, which may blur the true picture. When the PGA value is approaching 100 Gal, the percentage drop at station NIGH06 could be as large as 35%. Therefore, when the PGA level is relatively low the ground motion is probably not strong enough to cause additional damage to the medium. In this case weak nonlinear effects with increasing ground motion for material with frozen damage level or very minor additional damage is likely to be the major mechanism for our observations. On the other hand, when the PGA level is relatively high (i.e. approaching or large than 100 Gal), additional damage is generated and I start to observe much larger changes in the peak frequency (Figure 4.9), followed by logarithmic recovery (Figure 4.5). I have tried to quantify the recovery time scale for the coseismic peak frequency drop (see Wu *et al.* 2009a for additional analysis details). However, because the coseismic drop in peak frequency is small (Figure 4.7, especially for lower PGA ranges), and the logarithmic recovery on short timescales is very fast (Figure 4.5), I was not able to identify a sharp boundary between the near instantaneous recovery and the rapid logarithmic recovery. Based on the stacked spectral ratios for the 6 sites (e.g. Figure 4.5), the higher PGA threshold for production of significant additional damage and considerably stronger nonlinear effects (i.e. tens of percentage drop in peak frequency followed by a clear logarithmic type of recovery) ranges from ~60 Gal to more than 100 Gal.

4.5.2 Possible Mechanisms

I note that higher pre-existing damage makes the medium more susceptible to further damage, since it is generally easier to nucleate and grow cracks in material with higher crack density. Rubinstein and Beroza (2004b) and Rubinstein (2011) used the correlation between pre-exiting damage and susceptibility to additional damage to explain nonlinear effects associated with increasing damage induced by M4-5.5 aftershocks of the 1989 Mw6.9 Loma Prieta earthquake and 2004 Mw 6.0 Parkfield earthquake. Here I attempt to resolve nonlinear response that is *not* associated with further increase of the damage. I believe this is the situation in the cases with near instantaneous recovery to linear behavior in the times windows after the direct *S* waves for the following two reasons. First, I examined the damage recovery time of both large and small earthquakes utilized in this study and by Wu *et al.* (2009a) and found that the maximum recovery time to 90% of the reference value is less than 200 s. Since most aftershocks occurred well beyond this time interval, most of the damage caused by the preceding large earthquakes has been recovered at the occurrence time of each earthquake I utilized, and is continuously decreasing further. Some low-amplitude damage remains for longer durations, as documented in studies with repeating earthquakes (e.g. Rubinstein & Beroza 2004b; Peng & Ben-Zion 2006), and contributes to the overall long-term damage evident by the lower seismic velocities in the near surface material and fault zone structures (e.g. Li *et al.* 1990; Peng *et al.* 2003; Liu *et al.* 2005; Lewis & Ben-Zion 2010). Such remaining and decreasing transient damage will produce some apparent non-zero recovery time of the nonlinear behavior. However, this damage was produced by the previous events rather than by the motion that generates the subtle nonlinear effects I observe. Second, I also identified weak nonlinear effects for medium-size earthquakes before the M>6 events in each site, and I found no clear change in the nonlinear response for medium-size earthquakes before and after large events. Hence, I conclude that some of the nonlinear effects I observe for the medium-size earthquakes reflect nonlinear response of damaged rocks without additional increments to the levels of damage.

According to Figure 4.7, the PGA onset and degree of nonlinearity appear to vary significantly at different sites, so the PGA threshold probably also depend on the site conditions. I examined the site conditions in terms of the site classification by the average S-wave velocity (V_{S30}) in the upper 30 m of the site (NEHRP 2003), soil types at the top layers of each site, and the S-wave velocity contrast, but none of these properties shows any clear correlation with the PGA onset (see Table 4.1). It is likely that the existing rock damage at each site controls the onset of nonlinearity (e.g. Lyakhovsky *et al.* 2009). A useful quantification of the near-surface damage layer is the crack density, which could be estimated from analyses of seismic scattering and shear-wave splitting (e.g. Revenaugh 2000; Liu *et al.* 2005; Chao & Peng 2009). However, such analyses are beyond the scope of this paper. In any case, the results obtained in this study, together with the recent work of Rubinstein (2011), suggest that nonlinear site response can be induced by medium-size (M4-5) earthquakes and can occur more commonly than previously thought. The observed weak form of nonlinearity with near instantaneous recovery is likely associated with near constant material damage. As noted before, laboratory studies have identified nonlinear effects for geomaterials under strains as small as 10^{-8} (TenCate *et al.* 2004), which is much smaller than the dynamic strains (10^{-6}-10^{-5}) induced by the earthquakes utilized in this study. Observing nonlinear effects associated with such weak motion under *in-situ* conditions will require the development of additional analysis techniques and high resolution data. Although the significance of weak nonlinearity is case specific, quantification of nonlinearity at different degrees will help to further advance our understanding of site response to shaking caused by earthquakes.

CHAPTER 5

Temporal Changes of Site Response During the Mw9.0 Tohoku Earthquake in Japan

5.1 Introduction

It is well known that local site conditions have significant effects on the strong ground motions generated during large earthquakes (e.g., Joyner *et al.* 1976; Chin & Aki 1991; Yu *et al.* 1992). When the amplitude of ground motion exceeds a certain threshold, the sediment response deviates from the linear Hooke's law, resulting in nonlinear site effects (e.g., Beresnev & Wen 1996a). The recent Mw9.0 off the Pacific coast of Tohoku earthquake on 03/11/2011 is the largest earthquake in Japan's long earthquake recording history. This great earthquake is recorded by ~1200 K-NET/KiK-NET strong motion seismic stations with peak ground acceleration (PGA) at as high as ~3000 Gal (Aoi *et al.* 2011). In addition, the long-duration (~200 s) of the Tohoku earthquake (Hayes *et al.* 2011) generate a wide range of ground motions between less than 10 Gal to more than 1000 Gal from the direct waves, followed by long coda waves. This provides an unprecedented dataset to quantify the degrees of nonlinear site response and the temporal changes over a wide range of PGA levels.

Previous measurements on nonlinear site response were mostly from PGAs in the range of a few tens of Gal to a few hundred Gal (e.g., Sawazaki *et al.* 2006; Wu *et* *al.* 2009a; Rubinstein 2011). Their results are generally characterized by sharp reductions of the peak frequencies and peak spectral ratios during the large PGAs, followed by logarithmic recovery. In this chapter I present preliminary results from temporal changes of site response associated with a wide range of PGAs during the Tohoku main shock.

5.2 Data and Analysis Procedure

5.2.1 Seismic Data

The analysis employs strong motion data recorded by the Japanese Digital Strong-Motion Seismograph Network KiK-Net operated by National Research Institute for Earth Science and Disaster Prevention (Aoi *et al.* 2000). In this study I analyze data recorded by six stations (FKSH10, IBRH12, IBRH15, IBRH16, MYGH04, TCGH16). The six stations generally feature strong velocity contrast between the surface soil layers and the underlying bedrocks. The soil layers at the top several tens of meters generally consist of clay, sandy clay, filling, and gravel with very low *S*-wave velocities of ~100-200 m/s. The bedrocks are typically conglomerate, argillite, and shale with *S*-wave velocities of ~700-3000 m/s. These stations are chosen mainly because the PGAs recorded are well above the common soil nonlinearity threshold of ~200 Gal indicated by previous studies (Chin & Aki 1991; Beresnev & Wen 1996b), due to their relatively close distances to the epicenter of the Tohoku earthquake. I also find that the observed temporal changes in peak frequencies and peak spectral ratios (maxima of the spectral ratios) at these stations are much clearer than those at other stations, allowing us to better quantify temporal changes associated with the strong ground motion caused by the Tohoku main shock.

In the subsequent analysis I utilize a total of 32 events that occurred between 01/01/2011 and 03/28/2011 and recorded by the 6 surface and borehole strong motion sensors (Figure 5.1). These include 22 events starting 73 days before, the Tohoku main shock, and 9 events within 17 days after the main shock. The magnitudes of the events range from 3 to 9, and the hypocentral depths range from 5 to 100 km. The maximum PGA recorded at these 6 stations is 1220 Gal.

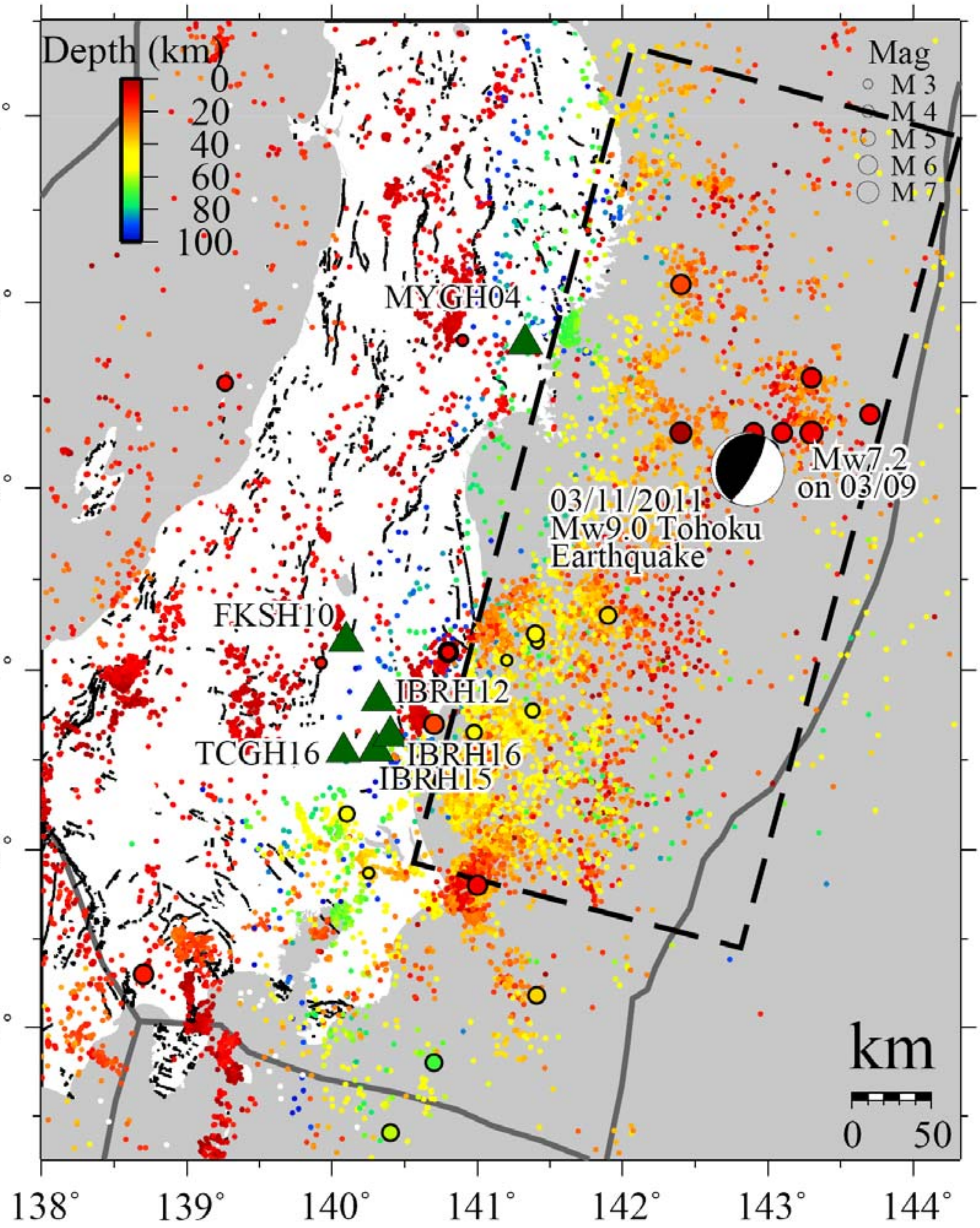

Figure 5.1 Map of the study region in Japan. The epicenter of the 2011 Mw9.0 Tohoku earthquake is indicated by the moment tensor solution (beach ball symbol). The large, black rectangle represents the fault area of the 2011 Tohoku earthquake, projected on the surface (Suzuki *et al.* 2011). Epicenters of other events analyzed in this study are shown in large circles. The size of circle indicates the magnitude of each event and color shows the depth with red being shallow and blue being deep. The background events since 2011/01/01 from the Japan Meteorological Agency (JMA) catalog are shown as small dots. Locations of the 6 KiK-Net stations used in this study are shown in green triangles. The black lines show the active faults in this region and the grey lines denote the subduction plate boundaries.

5.2.2 Analysis Procedure

The analysis procedure generally follows those of Sawazaki *et al.* (2006, 2009) and Wu *et al.* (2009a, 2009b, 2010), and is briefly described here. I use 6-s time windows that are moved forward by 2 s for all waveforms recorded by the surface and borehole stations. All possible seismic phases, including pre-event noise, *P*, *S* and coda waves are analyzed together, and the PGA value is measured for each window. Note that here the term PGA refers to the maximum acceleration value in each window, rather than for the entire seismic records. I apply the sliding-window-based approach to the records of the Tohoku main shock to track the temporal changes during and immediately after the strong motion, and also to all the other events to measure the reference level of peak frequency and peak spectral ratio (see the Results section). Figure 5.2a shows an example of original acceleration records at station IBRH15 generated by the Tohoku main shock, the *S*-wave, coda wave, and pre-event noise windows used to compute the spectral ratio.

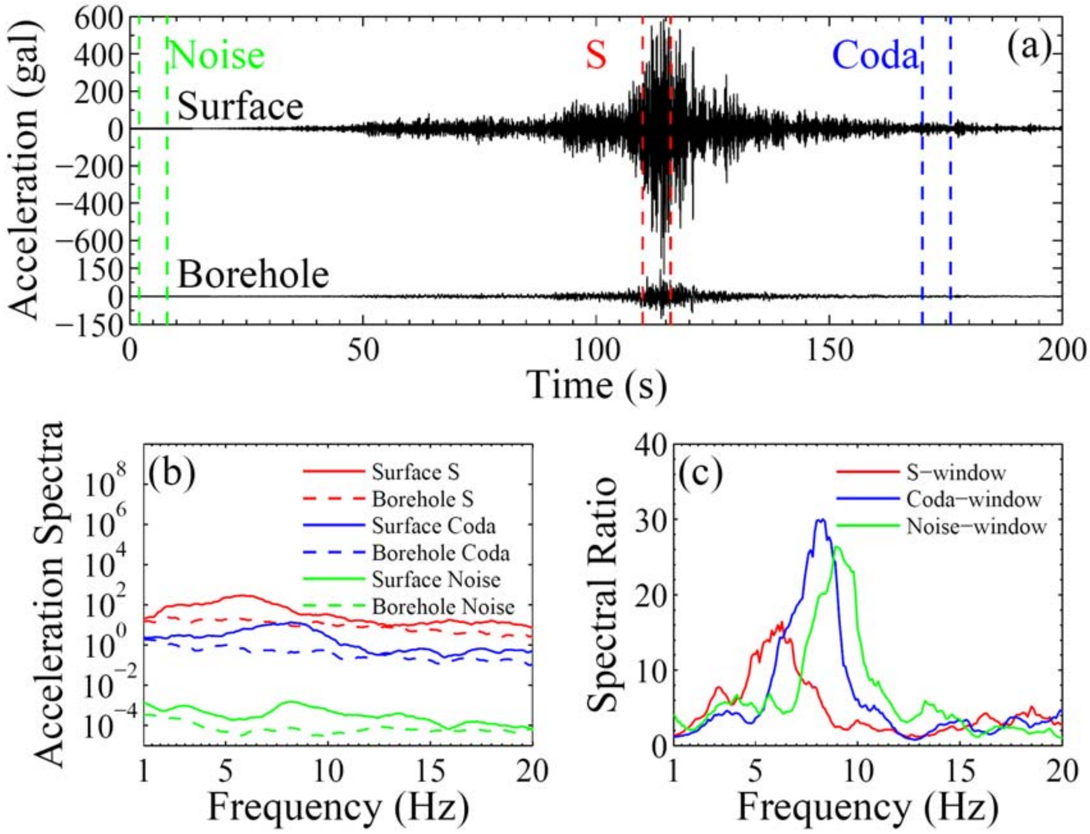

Figure 5.2 (a) EW-component ground accelerations recorded at the station IBRH15 generated by the Tohoku main shock. Surface and borehole recordings are shown at the top and bottom panels, respectively. The green, red and blue dashed lines indicate the pre-event noise, direct *S* and coda window that are used to compute the acceleration spectra in (b) and spectral ratios in (c).

Next, I remove the mean value of the traces and apply a 5 per cent Hanning taper to both ends. I add the power spectra of the two horizontal components and take the square root of the sum to get the amplitude of the vector sum of the two horizontal spectra. The obtained spectra are smoothed by applying the mean smoothing algorithm from the subroutine "smooth" in the Seismic Analysis Code (Goldstein *et al.* 2003), with half width of five points. The spectral ratio is obtained by taking the ratio of the horizontal spectra for surface and borehole stations. The amplitude of the spectra for both the surface and borehole recordings and the resulting spectral ratio at station IBRH15 are shown in Figure 5.2b and c.

5.3 Results

After processing all the data, I obtain 10272 spectral ratio traces for all the six stations from the sliding-window-based analysis. The running spectral ratios show clear decreases in peak spectral ratios and peak frequencies at the time of the Tohoku main shock, followed by an apparent logarithmic-type recovery (Figure 5.3). In addition, for the station MYGH04, two bursts of strong ground motions were recorded, and the peak frequency briefly recovers in between, and then followed by an apparent logarithmic recovery (Figure 5.3d).

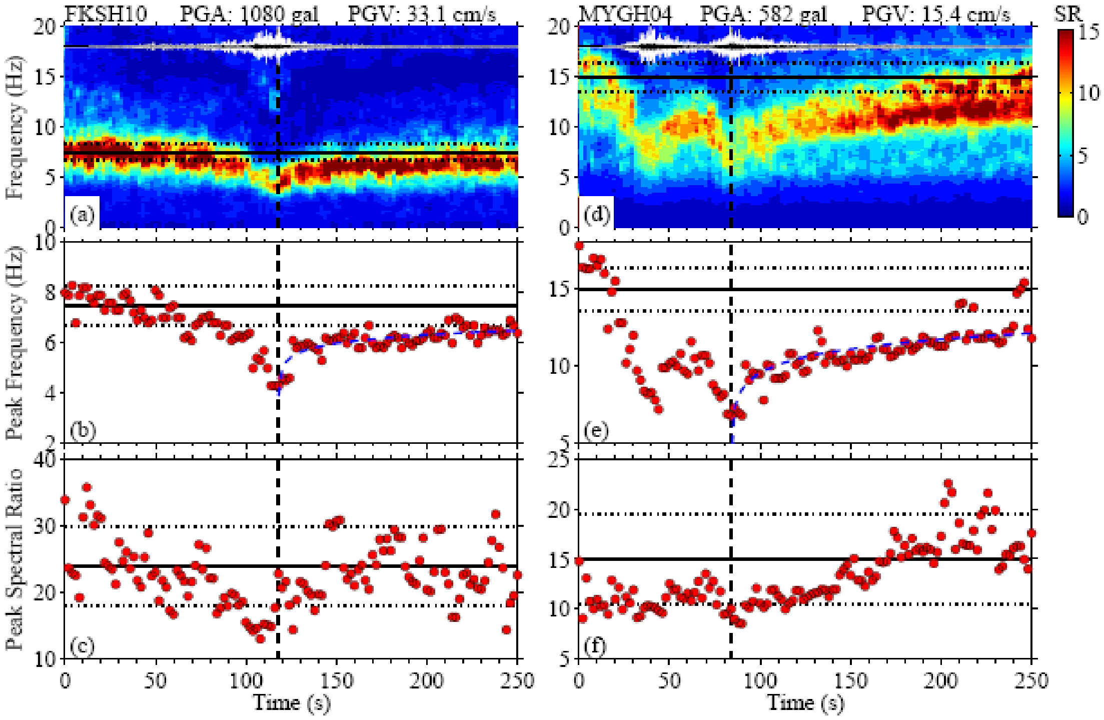

Figure 5.3 (a) Color-coded surface/borehole spectral ratios plotted against time for the station FKSH10. The x-axis shows the time since the beginning of the recording, and the y-axis shows the frequency. The spectral ratio values are color-coded with red being high and blue being low. The vertical dashed lines indicate the time when the highest PGA value is recorded. The horizontal solid and dotted lines show the reference value and uncertainties of the peak frequency obtained by averaging all the spectral ratios for the windows before the *P*-arrivals of all the earthquakes between 2011/01/01 and 2011/03/28. The white and black traces on the top show the waveforms of the surface and borehole recordings, respectively. (b) Measured peak frequencies from (a). The horizontal and vertical lines are the same as in (a). The blue dashed curve shows the least-squares logarithmic fitting of the peak frequencies after the highest PGA. (c) Measured peak spectral ratios from (a). The horizontal solid and dotted lines show the reference value and uncertainties of the peak spectral ratio obtained by averaging all the spectral ratios for the windows before the *P*-arrivals of all the earthquakes between 2011/01/01 and 2011/03/28. (d-f) Similar plots as (a-c) for the station MYGH04.

To better quantify the temporal changes in site response associated with different levels of ground shaking, I sort the spectral ratios traces by their PGA values, and average them in PGA bins of every 10 Gal from 0 Gal to the maximum PGA level. I have tested changing the size of PGA bin from 1 Gal to 20 Gal, and the obtained results are similar. Next, I identify the peak spectral ratio and peak frequency of the stacked trace at each PGA bin, and then compute the percentage drop of peak frequency and peak spectral ratio (Figure 5.4). The reference values of peak frequency and peak spectral ratio at each site are obtained by averaging all the spectral ratio traces for the windows before the *P*-arrivals of all the earthquakes at that site, assuming that the source and path effects are largely cancelled out by taking the spectral ratios between collocated surface and borehole stations. As shown in Figure 5.2c, the spectral ratio of the pre-event noise is very similar to the spectral ratio of the coda-window, except with a minor peak frequency shift. So this assumption is justified. I have tested averaging the spectral ratios of pre-event noise windows, coda windows, and direct *S*-arrival windows of small events as the reference spectral ratio, and the results are almost identical. According to Figure 5.4, the percentage drop of peak frequency and peak spectral ratio range from 40-60% and 30-70%, respectively, and generally increase with the PGA level. I compute the first order polynomial (linear) least-squares fitting of the data in Figure 5.4, and correlation coefficient is generally larger than 0.65. The only exception is the station TCGH16 where multiple peaks exist in the spectral ratios, which might introduce additional uncertainties in the measurement.

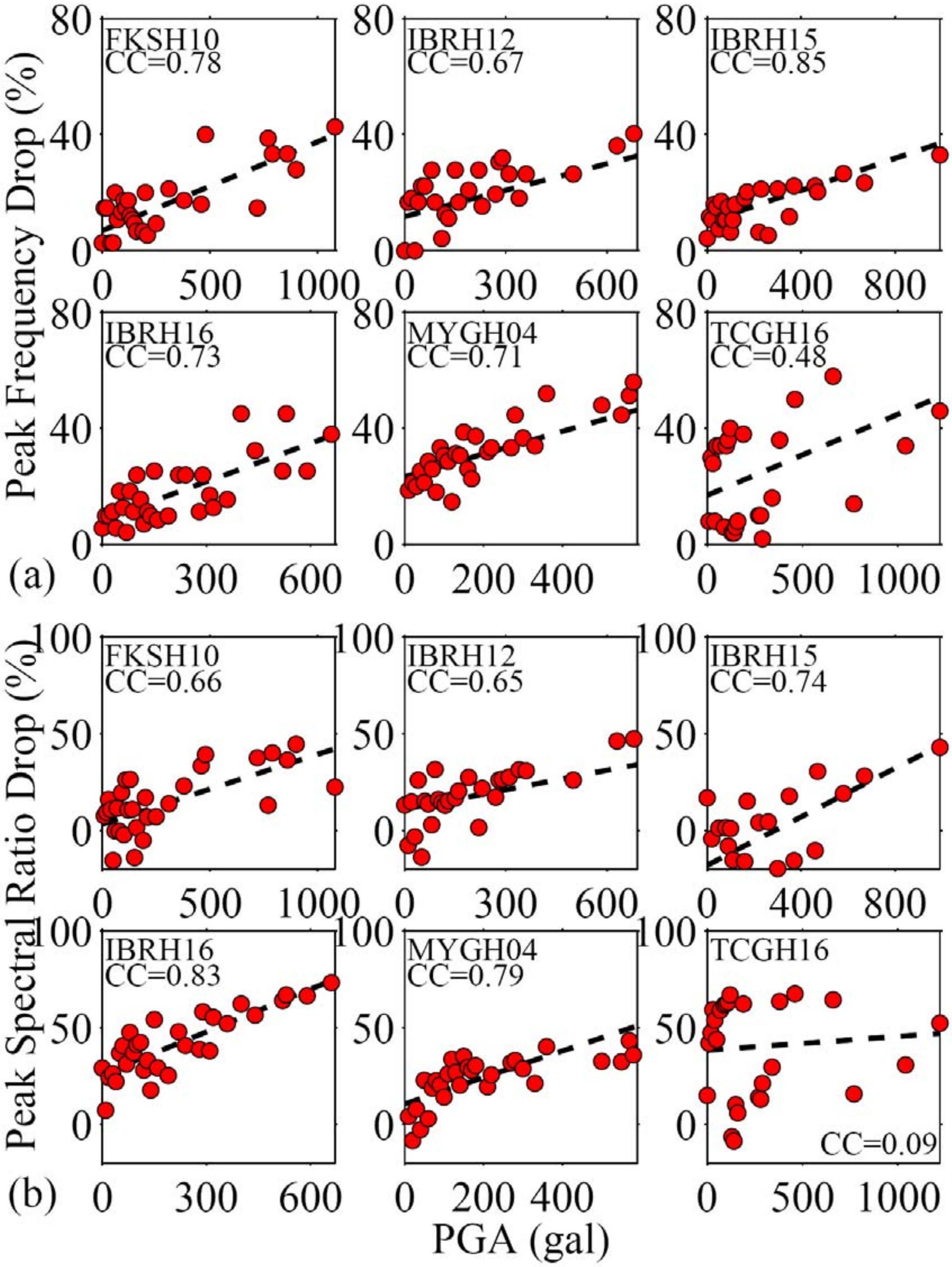

Figure 5.4 (a) Calculated percentage drop of peak frequencies plotted against PGA at the six stations during the Tohoku main shock. The black dashed line shows the least-squares fitting of the data. Station names and correlation coefficient values are marked on the top-left corner of each panel. (b) Similar figure as (a) for the percentage drop of the peak spectral ratios.

5.4 Discussion

Previous studies have found clear evidences of soil nonlinearity after previous large earthquakes in Japan, including the 1995 Mw6.8 Kobe earthquake, 2000 Mw6.8 Western Tottori earthquake, 2003 Mw8.3 Tokachi-Oki earthquake, 2003 Mw7.0 Miyaki-Oki earthquake, and 2004 Mw6.6 Niigata earthquake (e.g., Pavlenko & Irikura 2002a; Sawazaki *et al.* 2006; Rubinstein *et al.* 2007a; Assimaki *et al.* 2008; Wu *et al.* 2009a; Wu *et al.* 2010). The sharp reductions of the peak frequency and peak spectral ratio followed by gradual recovery observed in this study (Figure 5.3) are similar to the previous observations of nonlinear site response using spectral ratio approaches (e.g., Sawazaki *et al.* 2006; Wu *et al.* 2009a). Hence, I attribute the temporal changes of the spectral ratios to nonlinear site response during the main shock.

Assuming a soft soil layer over a half-space bedrock with large impedance contrast (Dobry *et al.* 2000), the fundamental resonant frequency f of the soil layer can be computed by Equation 3.1. Based on the site profiles of the 6 analyzed stations (see the KiK-Net website), strong velocity contrasts do occur between the surface sedimentary layers in the top several tens of meters and the underlying bedrock. The observed peak frequency in the spectral ratio traces (e.g., Figure 5.3) generally matches the values computed from site profiles using Equation 3.1. So the observed temporal changes are likely to be constrained within the surface sedimentary layers.

The peak frequency and peak spectral ratio generally recover to at least 90%

of the reference value in time periods of several tens to several hundred seconds after the strong shaking (e.g., Figure 5.3). At station MYGH04, the peak frequency drop to ~45% of the reference value during the first phase, followed by a recovery to ~80% of the reference value within ~30 seconds. However, the recovery process is interrupted by a second phase, which is observed by many stations close the coast of Fukushima-Ibaraki (Aoi *et al.* 2011). The PGA of the secondary phase at MYGH04 is comparable to the first phase, and cause similar type of drop and recovery of the peak frequency and peak spectral ratio, with a recovery time scale of ~150 seconds to the value before the second phase. I note that the peak frequency still do not recovery to the reference value at the end of the main shock record (~ 250 s after the origin time). Whether this is due to permanent damage or longer time recovery remains to be investigated further with aftershock data. Due to the length of the available data at the time of writing, I am not able to look at the longer-period lower-amplitude temporal changes of the material properties as suggested by some previous studies (Sawazaki *et al.* 2009; Lyakhovsky *et al.* 2009).

As measured before, the percentage drop of peak frequency and peak spectral ratio measured during the Tohoku main shock correlate (with correlation coefficient larger than 0.65) with the PGA value at most sites (Figure 5.4). The only exception is the station TCGH16, where there are two close peaks between 2 Hz and 6 Hz in the spectral ratio, which make the measurements of the peak frequency and peak spectral ratio more difficult and less accurate. The results in this study are generally consistent with the observation of Wu *et al.* (2009a) in the PGA range of 0 to ~500 Gal, but extend the correlation between the soil nonlinearity and the input PGA to a much higher PGA range of 500 Gal to more than 1000 Gal. The slope between the input PGA and the degrees of nonlinearity varies at different sites, which is likely caused by different site conditions. I have checked the site profiles for the six stations from the KiK-Net website (http://www.kik.bosai.go.jp), including average S-wave velocity (V_{S30}) in the upper 30 m of the site (NEHRP 2003), soil types at the top layers of each site, and the S-wave velocity contrast. However I do not find clear correlation between the site conditions and observed degrees of nonlinearity.

In this chapter I only focused on the clear temporal changes of site responses during the Tohoku main shock. Additional results on the long-term recovery and variable nonlinear behaviors will be reported in a follow-up work.

CHAPTER 6

Dynamic Triggering of Shallow Earthquakes near Beijing, China

6.1 Introduction

6.1.1 Earthquake Interaction

Earthquake interaction has been classified into three categories (Freed 2005): static, quasi-static, and dynamic triggering. Static triggering is associated with stress changes from permanent fault displacement, and mostly occurs around the immediate vicinity of the main shock rupture zone. Quasi-static triggering is typically associated with afterslip, viscoelastic relaxation, or fluid diffusion, and can occur at distances up to a few times the main shock rupture zone. In recent years, many studies have found widespread evidence that large earthquakes could also cause significant increase of seismicity rate in regions that are several hundreds to thousands of kilometers away (e.g. Hill *et al.* 1993; Brodsky *et al.* 2000; Gomberg *et al.* 2001; Hough & Kanamori 2002; Kilb *et al.* 2002; Hough *et al.* 2003; Gomberg *et al.* 2004; Prejean *et al.* 2004; Freed 2005; Hill & Prejean 2007; Velasco *et al.* 2008). This type of triggering is mostly caused by dynamic stresses associated with large amplitude surface waves. Systematic investigations of dynamic triggering could help to improve the understanding of the underlying mechanisms of earthquake initiation and interaction, which are both key components of earthquake forecasting and hazard analysis.

6.1.2 Dynamic Triggering in Intraplate Regions

Previously, dynamically triggered earthquakes are identified preferentially near active plate boundary faults or geothermal/volcanic regions with abundant background seismicity (Hill *et al.* 1993; Hill & Prejean 2007; Peng *et al.* 2011b, and reference within). Recent studies have found remotely triggered earthquakes in relatively stable intraplate regions (e.g. Hough *et al.* 2003; Gomberg *et al.* 2004; Velasco *et al.* 2008; Gonzalez-Huizar & Velasco 2011). Peng *et al.* (2010b) found clearly triggered earthquakes in north China after the 2008 Mw 7.9 Wenchuan earthquake. Jiang *et al.* (2010) extended the analysis of Peng *et al.* (2010b) to the rest of continental China, and found many triggered earthquakes near active faults in different tectonic settings. These observations further support the view that earthquake dynamic triggering is a ubiquitous phenomenon that is independent of tectonic environments, and a number of physical mechanisms could play a role in dynamic triggering (Velasco *et al.* 2008). However, the underlying mechanisms of dynamic triggering in various tectonic environments remain a topic that need further investigations (Hill & Prejean 2007).

6.1.3 Physical Models and Triggering Potential

Physical models proposed to explain the dynamic triggering process typically fall into two categories (Hill & Prejean 2007; Hill 2008): direct triggering by friction failure via different modes (e.g. Gomberg *et al.* 1997, 2001, 2005; Perfettini *et al.* 2003; Johnson & Jia 2005; Hill 2008), or indirect triggering through excitation of crustal fluids and/or transient deformation (e.g. Linde & Sacks 1998; Brodsky *et al.* 1998, 2000, 2003; Hill *et al.* 2002). The friction failure model assumes that the critically stressed faults are triggered by the transient dynamic stress from the passing seismic waves, so the triggered seismicity usually occurs during or immediately after the teleseismic waves. On the other hand, indirect triggering models generally involve some time delays between the passing seismic waves and the onset of triggered earthquakes, due to the response time of fluids or transient deformation.

Many factors could play a role in determining the triggering potential at each site. These includes dynamic stresses at the triggering depth (wave type, amplitude, frequency, and incidence angle), local conditions (triggered fault type, fault orientation, tectonic environments, and hydrological properties), and information about the triggered earthquakes (origin times, hypocentral locations, and focal mechanisms). Comprehensive investigation of these parameters would not only help to better constrain the physical mechanisms of dynamic triggering, but also help to identify the conditions that favor dynamic triggering at various tectonic settings.

Here I present a systematic analysis of dynamic triggering near Beijing in north China associated with 4 large teleseismic earthquakes in East Asia (Figure 6.1). I focus on this region because it is covered by a dense regional seismic network, and previous studies have identified remotely triggered seismicity by the 2008 Mw 7.9

Wenchuan earthquake (Peng *et al.* 2010b; Jiang *et al.* 2010). Following our previous study, I find that this region was also triggered by four large teleseismic earthquakes (including the Wenchuan earthquake). The local earthquakes are likely triggered by Coulomb stress changes at shallow depths (< 5km), and the possible controlling parameters for dynamic triggering include amplitude, incident angle, and type of the surface waves.

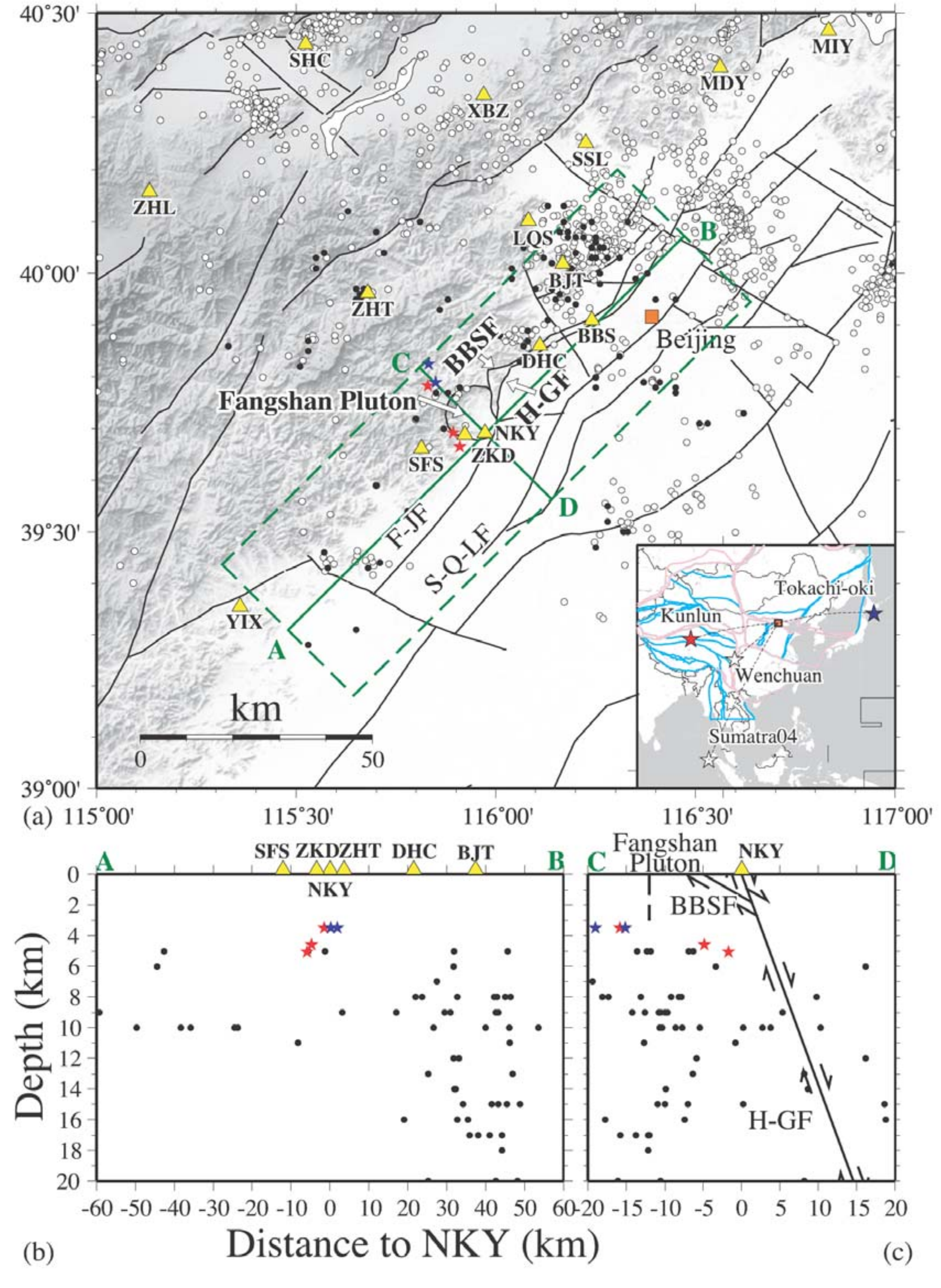

Figure 6.1 (a) A map showing the study region around Beijing in north China. The yellow triangles mark the seismic stations in the CC network utilized in this study. Red and blue stars mark the epicenters of local earthquakes triggered by the 2001 Mw7.8 Kunlun and 2003 Mw8.3 Tokachi-oki earthquakes, respectively. The filled and open circles mark the background seismicity with waveforms and listed in the

local catalog, respectively. The regional and local faults are marked as black lines. The Babaoshan fault, Huangzhuang-Gaoliying fault, Fangshan-Jumahe Fault, Shunyi-Qianmen-Liangxiang Fault, and Fangshan Pluton are labeled as BBSF, H-GF, F-JF, S-Q-LF, and Fangshan Pluton, repectively. The solid green line along AB and the green dashed line box show the projection line and projection area in (b). The orange square shows the location of Beijing. The inset shows a map of China with the box corresponds to the study region. The red and blue stars mark the epicenters of the 2001 Mw7.8 Kunlun and 2003 Mw8.3 Tokachi-oki earthquakes, respectively. The open stars show the epicenters of the 2004 Mw9.2 Sumatra and the 2008 Mw7.9 Wenchuan earthquakes. The dashed lines show the ray paths. The major tectonic block boundaries and block-boundary faults are shown in pink and cyan lines, respectively. (b) Cross-section view of the line AB in (a). The triggered and background seismicity within the green box in (a) and nearby stations are projected the line AB. (c) Cross-section view of the line CD in (a). The triggered and background seismicity within the green box in (a) and the station NKY are projected to the line CD. The black lines show the schematic dipping directions of Babaoshan and Huangzhuang-Gaoliying faults, with arrows showing the slip directions. The vertical dashed line shows the surface boundary of the Fangshan Pluton.

6.2 Study Region

Our study region is about 35 km southwest of Beijing, and it is within the southwestern part of the North China Plain (Figure 6.1). This region is along the major block boundary of the Taihang Mountain in the west and the Bohai Bay Basin in the east, and there is a significant lateral thickness variation of lithosphere at this region (Chen *et al.* 2008). This region is also characterized by many normal faults and compressive folds in the NW to NWW directions (Deng *et al.* 2003), including the Babaoshan and Huangzhuang-Gaoliying faults, and several other major parallel faults (Figure 6.1). In particular, the Babaoshan and Huangzhuang-Gaoliying faults are both normal faults with the strike in the NW direction. The dipping angles of Babaoshan and Huangzhuang-Gaoliying faults are $25-35^{\circ}$ and $65-75^{\circ}$, respectively (Che *et* *al.* 1997). Previous studies of leveling, gravity, geomagnetic and strain field of region close to these faults suggest that the shallow part of Babaoshan fault is currently creeping, while the Huangzhuang-Gaoliying fault is currently locked (e.g. Che *et al.* 1997; Che & Fan 2003). The background seismicity in this region is relatively low, and the earthquakes are generally not close to the faults inferred from the surface trace and dipping angles. Another interesting feature in the study region is the Fangshan Pluton, which is an intrusive Mesozoic pluton (133–128 Ma) at the junction of Taihang tectonic belt and Yanshan intraplate orogenic belt (Yan *et al.* 2006; Wang *et al.* 2011). The intrusion is mainly composed of quartz diorite and granodiorite, and its lithological boundary to the host rocks is marked as a curve around stations NKY and ZKD in Figure 6.1. This region has been seismically active in historic times, with several M 6-7 earthquakes occurring in the 17-18th century (e.g., an M~6 earthquake on 1658/02/03 and an M~6.5 on 1730/09/30). Currently the region is seismically quiet, with ~23 M>1 earthquakes each year since 2000 (Peng *et al.* 2010b).

6.3 Seismic Data

The analysis employs seismic data recorded by 45 stations in the Capital-Circle (CC) digital seismograph network (Figure 6.1) operated by the China Earthquake Networks Center (Liu *et al.* 2003; Chen *et al.* 2006). The network consists of 107 broadband, borehole and surface short-period stations. First I search the Advanced National Seismic System (ANSS) catalog for all the M≥7.5 teleseismic earthquakes since 2000 with hypocentral depth less than 100 km, and download the seismic data from 8 hours before until 8 hours after each teleseismic earthquake recorded at the broadband station BJT that belongs to the New China Digital Seismograph Network (IC). I visually examine the 5 Hz high-pass filtered seismograms of all the 39 teleseismic earthquakes, and identify clear impulsive signals with double peaks during the passage of surface waves of four large earthquakes in East Asia, including 2001 Mw7.8 Kunlun, 2003 Mw8.3 Tokachi-oki, 2004 Mw9.2 Sumatra, and 2008 Mw7.9 Wenchuan earthquakes. Figure 6.2 shows that the Peak Ground Velocities (PGVs) measured from both the vertical and transverse components for the four earthquakes are generally larger than those for the rest of the earthquakes. I note that other four teleseismic earthquakes (e.g., 2001 Mw7.7 El Salvador, 2001 Mw7.7 India, 2006 Mw8.3 Kuril, and 2007 Mw8.1 Solomon earthquakes) are also associated with some local high-frequency signals during their passing surface waves, but the signals are not clear as the previous four cases, and the other 31 teleseismic earthquakes show no sign of triggered earthquakes. Hence, in this study I focus on those four earthquakes with clear triggering and request the data from all stations in the CC network.

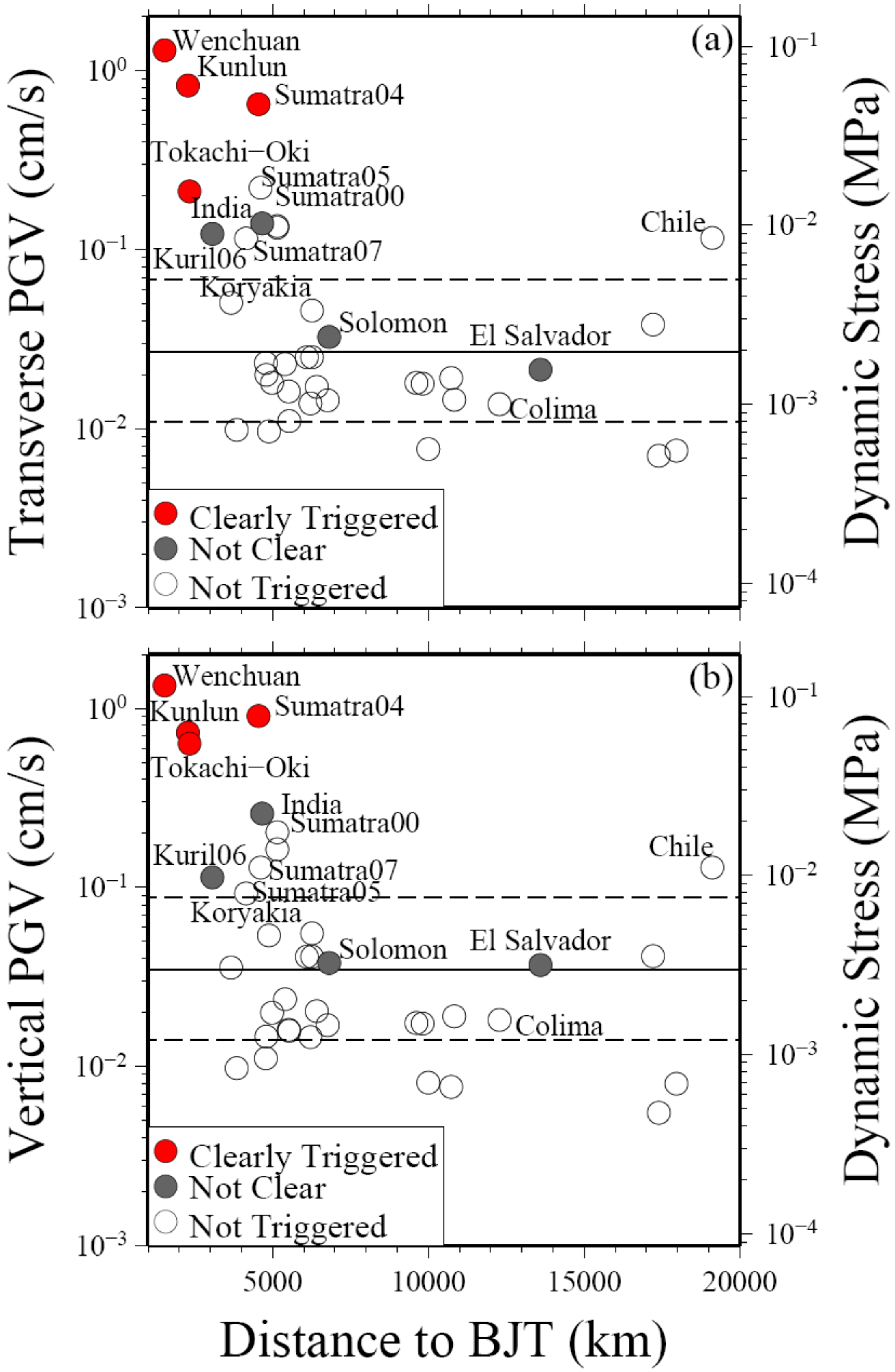

Figure 6.2 (a) Transverse Peak Ground Velocity (PGV) and the corresponding

Dynamic Stress (DS) plotted against epicentral distance at station BJT for all the 39 teleseismic events utilized in the preliminary survey. The y-axes on the left and right show the scales for the PGV and DS, respectively. The DS is estimated using the relationship $DS = G * PGV / V$ (Hill *et al.* 1993), where V is the phase velocity, and assumed to be 3.5 km/s, and G is the shear rigidity, which is assigned as a nominal value of 30 GPa. Solid red and grey circles show the teleseismic events with clear and unclear triggering effects, respectively. Open circles show the teleseismic events without triggering effects. The horizontal solid and dashed lines mark the approximate threshold and range of PGV for dynamic triggering, respectively. (b) Similar plot as (a) for vertical PGV and DS.

6.4 Analysis Procedure

The analysis procedure generally follows that of (Peng *et al.* 2010b; Jiang *et al.* 2010) and is briefly described here. I visually examine all the records, and remove those bad traces with incomplete surface wave recording, because triggered seismicity is generally found during and immediately after the large amplitude surface waves (Velasco *et al.* 2008). After the selection process, I obtain a total of 154 station-event pairs for subsequent analysis. I remove the instrument response to obtain the velocity records. I also remove the mean and trend, and apply a 5 Hz two-way high-pass Butterworth filter to all the data. Then I visually identify local earthquakes as impulsive seismic energies with clear *P*- and *S*-waves on the 5 Hz high-pass-filtered three-component velocity records (e.g., Figure 6.3d). In the following analysis, I focus only on the station-event pairs with at least one identified local earthquake within 1-hour of the *P*-arrivals of the teleseismic earthquakes.

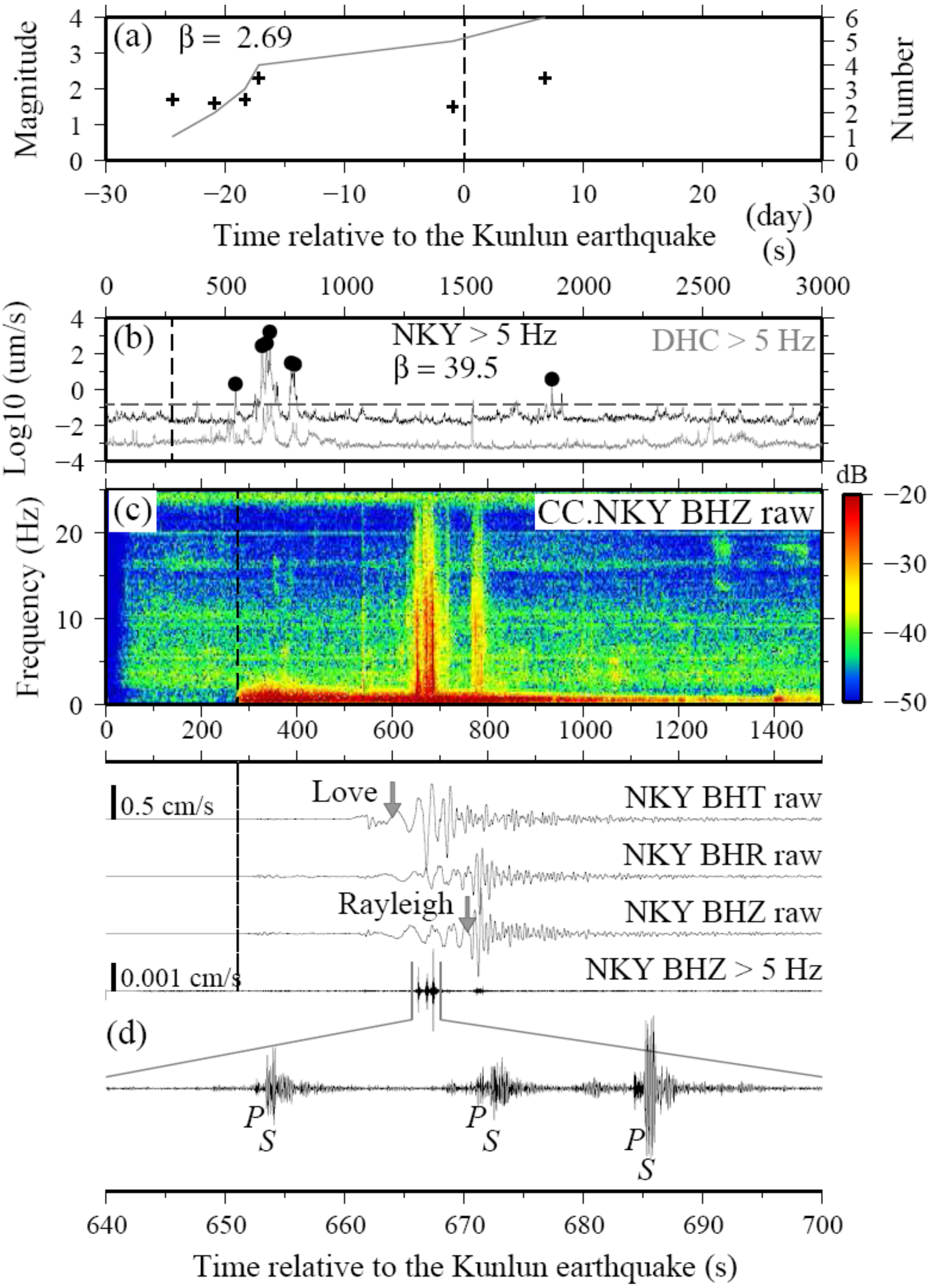

Figure 6.3 (a) Seismicity ± 30 days of the Kunlun main shock and within 120 km of station NKY near Beijing. The crosses mark the events listed in the regional earthquake catalog and the line shows the cumulative number of events. The corresponding β-statistic value based on the catalog is 2.69. The vertical dotted line marks the *P*-arrival time of Kunlun earthquake at NKY through panel a-d. (b) The

5-Hz high-pass-filtered envelope functions at station NKY (solid line) and the nearby station DHC (gray line) within ~3000s of the *P*-wave arrival of the Kunlun earthquake (vertical dashed line). The solid circles mark the hand-picked events after the *P*-arrival. The corresponding β statistic value is 39.5. The horizontal dashed line marks the 10 times median absolute deviation (MAD) threshold. (c) The spectrogram of the vertical component seismogram recorded at station NKY. I applied a 0.5 Hz high-pass filtering to the raw data before computing the spectrogram to remove the potential high frequency artifact by computing short-time FFT for long-period signals (Peng *et al.* 2011a). The color bar shows the spectra value in 10log10(cm/s/Hz) dB. (d) Raw and high-pass-filtered seismograms showing the teleseismic waves of the Kunlun earthquake and local seismic events, respectively. The top three traces: the raw three component (transverse, radial and vertical) seismograms recorded at station NKY. The grey arrows indicate the predicted Love and Rayleigh wave arrival times based on the peaks in seismogram assuming Love wave velocity of 3.8 km/s, and Rayleigh wave velocity of 3 km/s. The middle trace: 5 Hz high-pass-filtered seismograms on vertical component showing small local earthquakes during and immediately after the passage of surface waves. The bottom trace: a zoom-in plot of the vertical seismograms showing the *P*- and *S*-waves of the three triggered earthquakes recorded at station NKY.

6.4.1 β Statistics

The β statistics measures the differences between the observed number of events after the main shock and the expected number from the average seismicity rate before the main shock, and is scaled by the standard deviation of the seismicity rate (Matthews & Reasenberg 1988; Reasenberg & Simpson 1992). It is defined by

$$\beta(n_a, n_b; t_a, t_b) = \frac{n_a - E(n_a)}{Var(n_a)} \tag{6.1}$$

where n_b and n_a are the number of earthquakes observed before and after the main shock, t_b and t_a are the time duration before and after the main shock, respectively. $E(n_a)$ is the expected number of events within the period t_a and $Var(n_a)$ is the standard deviation. For a binomial process, $E(n_a) = n_b\ (t_a / t_b)$, and $Var(n_a) = n_b\ (t_a / t_b)\ (1 - n_b / n_a)$

(Gomberg *et al.* 2001; Kilb *et al.* 2002; Pankow *et al.* 2004; Hough 2005). When the seismicity rate before the main shock is small enough, the binomial process could be simplified as a Poisson process, where $E(n_a) = Var(n_a) = n_b\ (t_a\ /t_b)$ (Hill & Prejean 2007). Results with $|\beta| > 2$ (approximately two standard deviations) are generally considered as statistically significant (Reasenberg & Simpson 1992; Hill & Prejean 2007).

Next, I manually pick earthquakes on the high-pass filtered seismograms 6 hours before and 1 hour after the *P*-arrival of each teleseismic event for station BJT. I first take the envelope function of the 5 Hz high-pass filtered seismogram, smooth it with half window width of 1 Hz, and stack the resulting three-component envelopes to obtain the envelope function for each event-station pair. Next, I identify the events by searching for clear double peaks in the envelope function that correspond to *P* and *S* waves. I use 10 times of the median absolute deviation (MAD) with duration of 1 hour before the *P* arrival as amplitude threshold. Only the events with amplitude larger than the threshold are used to compute the β statistics to ensure that the handpicked events are not caused by the random fluctuations or near-surface high frequency noises. Finally I replace the number of earthquakes n_b and n_a with the amplitude-normalized number of N_b and N_a that are defined by $N_b = n_b$ and $N_a = n_b \sum_{i=1}^{n_a} A_i^{'} \Big/ \sum_{i=1}^{n_b} A_i$, where A_i and A_i^{i} are the amplitudes of events before and after the main shock h(Miyazawa & Mori 2006; Jiang *et al.* 2010). When there is no earthquake before the main shock, I assume $N_b = n_b = 0.25$, and

$\frac{1}{n_b}\sum_{i=1}^{n_b} A_i = 10 \times MAD$ to compute N_a (Kilb *et al.* 2002).

For the β statistics for all the CC stations, t_a and t_b depend on the length of available seismic data. For the β statistics based on regional catalog, I infer the scaled amplitude of the each event from the magnitude using a simple scaling relationship $A = \sqrt{10^{M_w}}$ (Stein & Wysession 2003), where A and M_w are the scaled amplitude and moment magnitude, respectively.

6.5 Results

6.5.1 General Patterns

After visual inspection of the 5 Hz high-pass filtered data from all the CC network stations, I identified 19 triggered earthquakes the first hour following the *P*-arrivals of the four teleseismic earthquakes (Table 6.1, Figures 6.3-6.6). Figure 6.3 shows seismic activity ± 30 days of the Kunlun earthquake from regional earthquake catalog (Figure 6.3a) and the high-pass-filtered envelope function at station NKY (Figure 6.3b). Similar examples for the station-event pairs NKY-Tokachi-oki, ZHT-Sumatra2004, NKY-Wenchuan are shown in Figures 6.4-6.6. I note that none of the visually identified local earthquakes from the high-pass filtered continuous data are listed in the earthquake catalog, and there is no clear change in seismicity rate from the catalog ± 30 days of the four teleseismic earthquakes I analyzed. In comparison, I do see significant increase of seismicity rate (β > 2) from the continuous recordings. This is consistent with recent observations of dynamic triggering in other regions (e.g. Gomberg *et al.* 2004; Prejean *et al.* 2004; Jiang *et al.* 2010), and suggests that analyzing continuous seismic data is more effective in identifying remotely triggered earthquakes (Hill & Prejean 2007). Because of this, I focus on the results from the continuous waveform data in the following section.

Table 6.1 List of all the 19 triggered events found in this study. Fields 1-10 are year and name of triggering teleseismic event, station, *P*- and *S*-wave arrival time, longitude, latitude and depth of triggered event (if located), triggered event ID, respectively.

Year	Event	Stn	Tp(s)	Ts(s)	Lon.	Lat.	Depth (km)	ID
2001	Kunlun	NKY	540.7223	541.9534	115.91	39.66	5	1
2001	Kunlun	SFS	541.2228	542.7903	115.91	39.66	5	1
2001	Kunlun	ZKD	540.5175	541.3626	115.91	39.66	5	1
2001	Kunlun	BJT	656.1245	657.6993	115.83	39.78	3.5	2
2001	Kunlun	DHC	655.8533	658.3444	115.83	39.78	3.5	2
2001	Kunlun	NKY	652.3952	653.4281	115.83	39.78	3.5	2
2001	Kunlun	SFS	652.8047	654.1589	115.83	39.78	3.5	2
2001	Kunlun	ZHT	654.1443	655.7768	115.83	39.78	3.5	2
2001	Kunlun	ZKD	652.1589	652.8111	115.83	39.78	3.5	2
2001	Kunlun	BJT	688.754	691.7498	115.89	39.69	4.6	3
2001	Kunlun	DHC	689.8282	692.4067	115.89	39.69	4.6	3
2001	Kunlun	NKY	684.322	685.1851	115.89	39.69	4.6	3
2001	Kunlun	SFS	684.4601	685.8047	115.89	39.69	4.6	3
2001	Kunlun	ZKD	683.8246	684.4965	115.89	39.69	4.6	3
2001	Kunlun	NKY	669.903	671.9211	NA	NA	NA	4
2001	Kunlun	NKY	781.0661	789.0028	NA	NA	NA	5
2003	Tokachi-oki	NKY	663.4778	664.9517	115.85	39.78	3.5	6
2003	Tokachi-oki	SFS	663.6976	665.0173	115.85	39.78	3.5	6
2003	Tokachi-oki	ZHT	665.9599	667.4166	115.85	39.78	3.5	6
2003	Tokachi-oki	NKY	697.2234	699.4741	115.83	39.82	3.5	7
2003	Tokachi-oki	SFS	697.4884	699.3102	115.83	39.82	3.5	7
2003	Tokachi-oki	ZHT	696.7382	699.8997	115.83	39.82	3.5	7
2004	Sumatra	ZHT	946.2632	947.5602	NA	NA	NA	8
2004	Sumatra	ZHT	1285.147	1286.376	NA	NA	NA	9
2004	Sumatra	ZHT	1357.147	1358.45	NA	NA	NA	10
2004	Sumatra	ZHT	1419.816	1422.348	NA	NA	NA	11
2004	Sumatra	ZHT	1650.277	1651.676	NA	NA	NA	12
2004	Sumatra	ZHT	1680.532	1682.954	NA	NA	NA	13
2004	Sumatra	ZHT	2410.326	1682.799	NA	NA	NA	14
2004	Sumatra	ZHT	3021.666	3023.112	NA	NA	NA	15
2008	Wenchuan	NKY	394.8726	396.6338	NA	NA	NA	16
2008	Wenchuan	NKY	423.1113	424.4873	NA	NA	NA	17
2008	Wenchuan	NKY	437.8728	439.2304	NA	NA	NA	18

Table 6.1 Continued.

2008	Wenchuan	NKY	521.3867	522.5425	NA	NA	NA	19

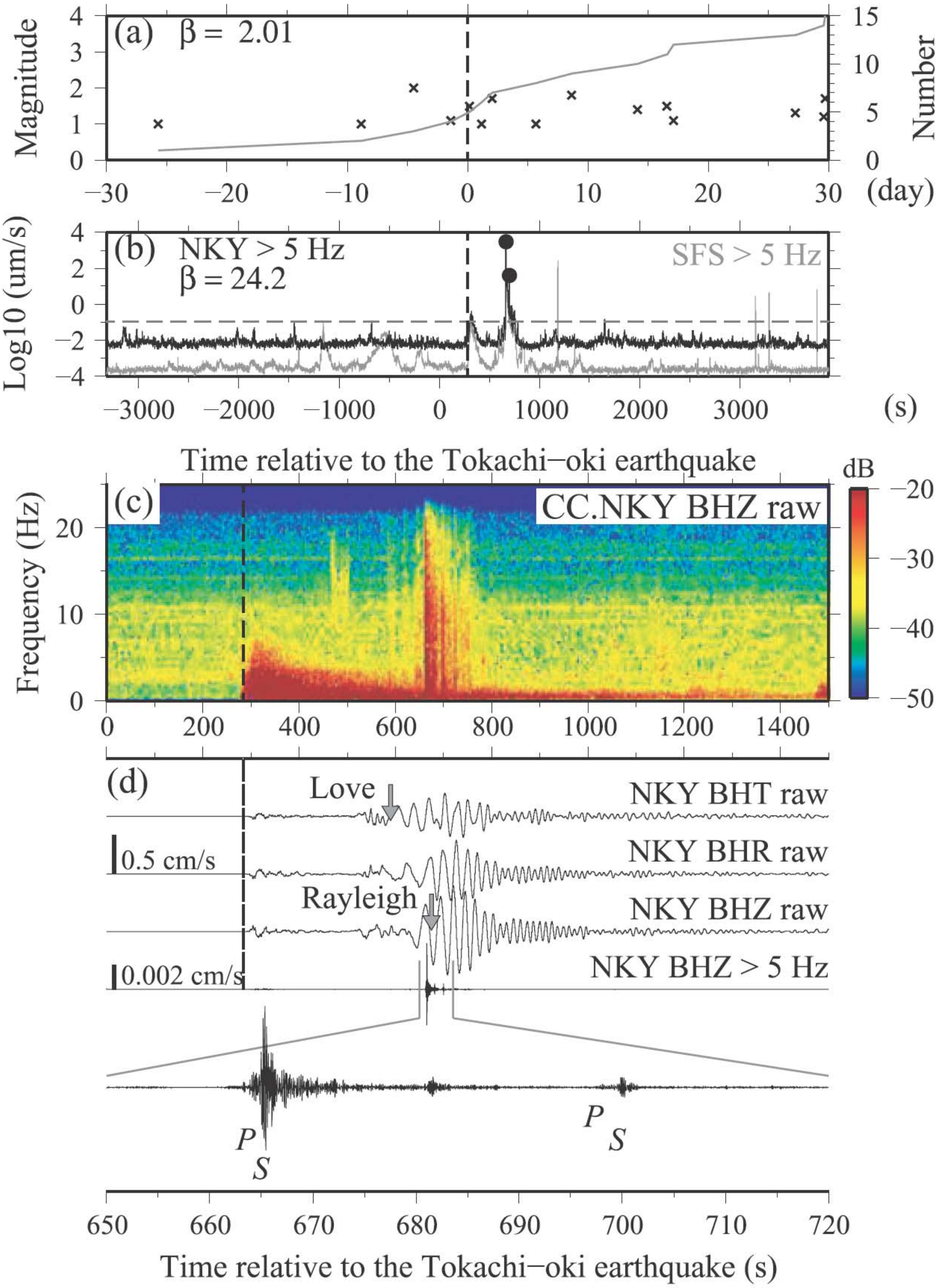

Figure 6.4 Similar plot as Figure 6.3 for the station-event pair NKY and the 2003 Tokachi-oki earthquake.

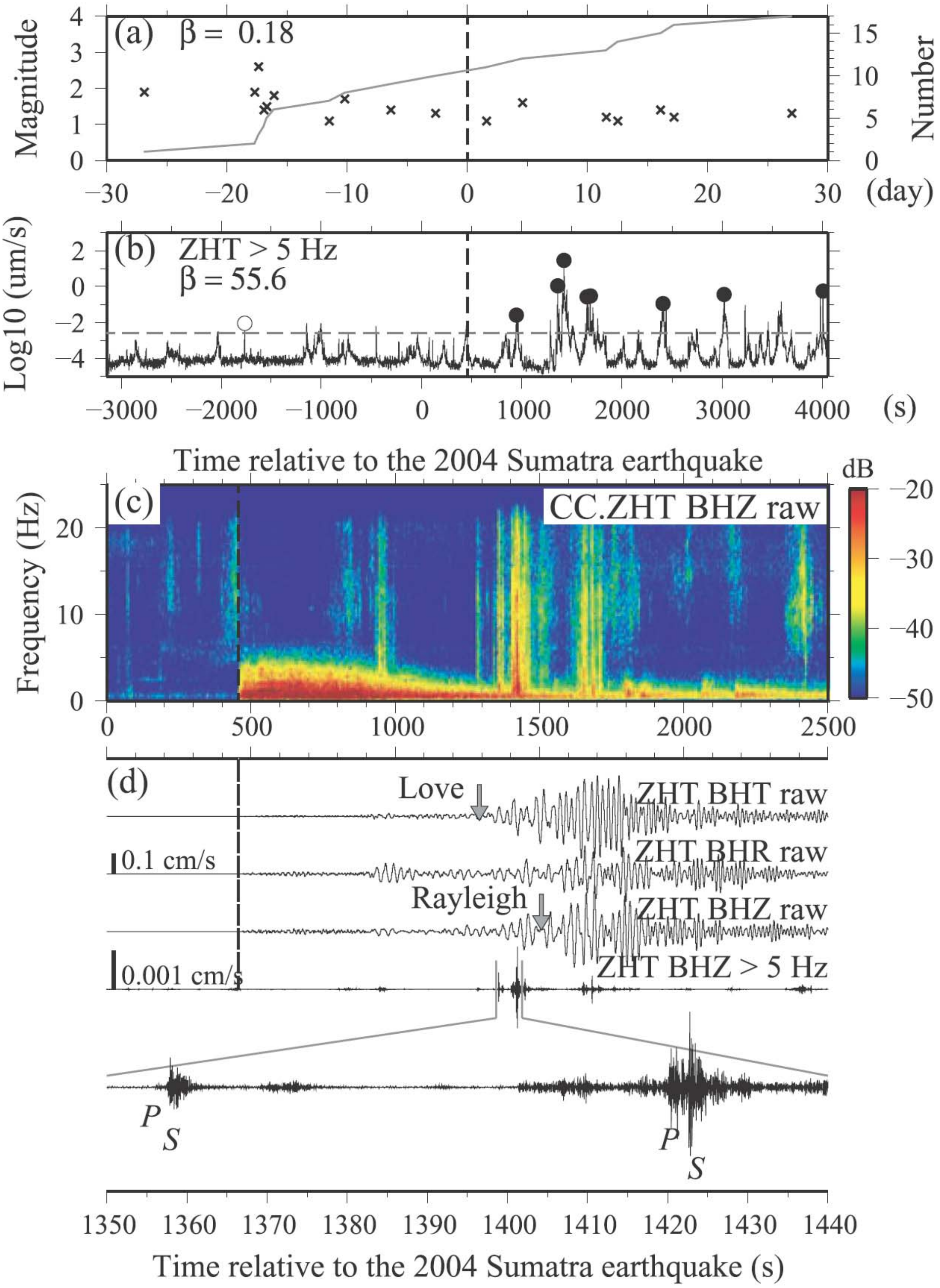

Figure 6.5 Similar plot as Figure 6.3 for the station-event pair ZHT and the 2004

Sumatra earthquake.

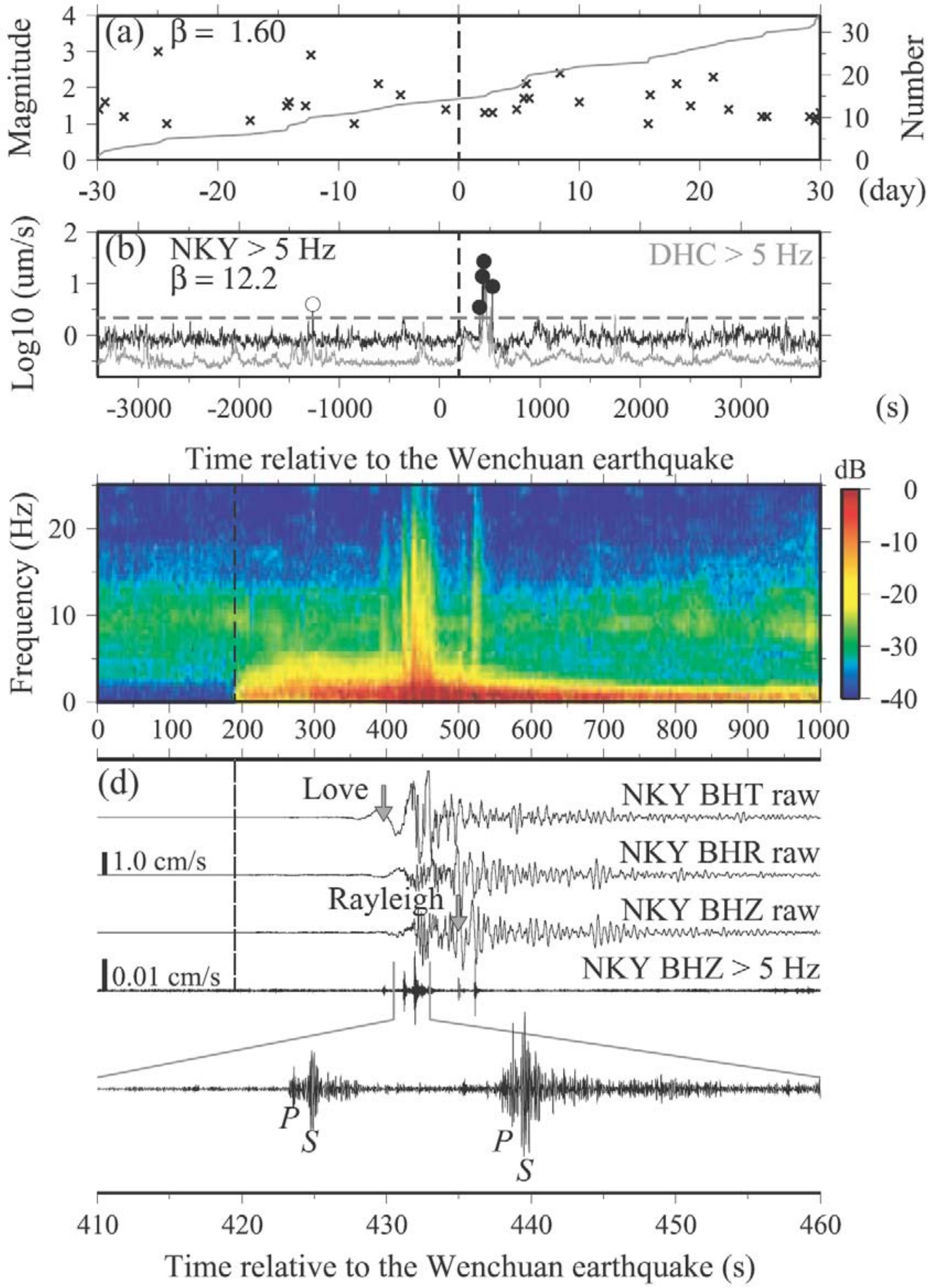

Figure 6.6 Similar plot as Figure 6.3 for the station-event pair NKY and the 2008 Wenchuan earthquake, modified from Jiang *et al.* (2010).

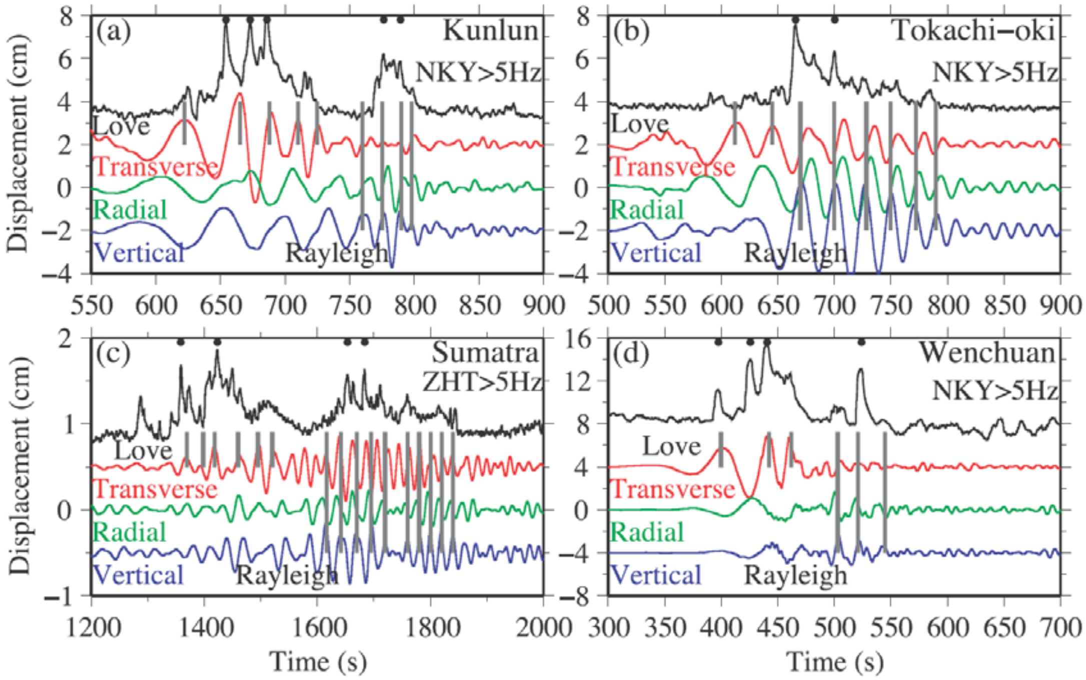

Figure 6.7 Zoom-in plots of the timing between the triggered seismicity and surface waves. (a) The top black trace shows the smoothed envelope function in logarithmic scale averaged from the 5 Hz high-pass filtered 3-component velocity records at NKY for the 2001 Kunlun earthquake. The broadband transverse, radial, and vertical displacement seismograms are plotted as red, green, and blue colors, respectively. The black dots on the top mark the timing of the triggered events. The short and long vertical grey lines mark the peaks of Love and Rayleigh waves, respectively. (b), (c), and (d) similar plot as (a) for the 2003 Tokachi-oki, 2004 Sumatra, and 2008 Wenchuan earthquakes, respectively.

Overall the surface waves of the four analyzed teleseismic earthquakes coincide with locally triggered earthquakes in our study region, and the increase of seismicity rate is statistically significant ($\beta > 2$) (Figures 6.3-6.6). In all four cases, the triggered seismic events occur during the first few cycles of the Love waves, and occurred again during the large-amplitude Rayleigh waves (Figure 6.7). The amplitudes of the triggered earthquakes during the Love waves appear to be larger than during the Rayleigh waves for the Kunlun, Sumatra, and Wenchuan earthquakes (Figures 6.3, 6.5-6.7). For the Tokachi-oki earthquake, the triggered earthquakes during the Rayleigh waves have much larger amplitudes (Figure 6.4).

5.5.2 Locations of Triggered Earthquakes

From visual comparison of the arrival times of the triggered earthquakes, I find 5 triggered earthquakes that are recorded by at least 3 stations. An example of high-pass-filtered seismograms showing triggered earthquakes recorded at different stations is given in Figure 6.8. Next, I pick the *P*- and *S*-arrival times for each station-event pair, and locate the 5 local earthquakes in both HYPO2000 and HYPO71 programs (Klein 2002) using the hand-picked *P*- and *S*-arrival times. The obtained locations from both methods are nearly identical. I also use the double-difference relocation program HypoDD (Waldhauser 2001) to relocate the 5 triggered earthquakes together with the background seismicity (a total of 107 earthquakes from 2001 to 2007) based on both the hand-picked and waveform cross-correlated travel times. Because the relocation method mostly works for earthquakes that are in close distance, the relocation process does not change the locations of the 5 triggered earthquakes that are relatively far from most of the background earthquakes (Figure 6.1).

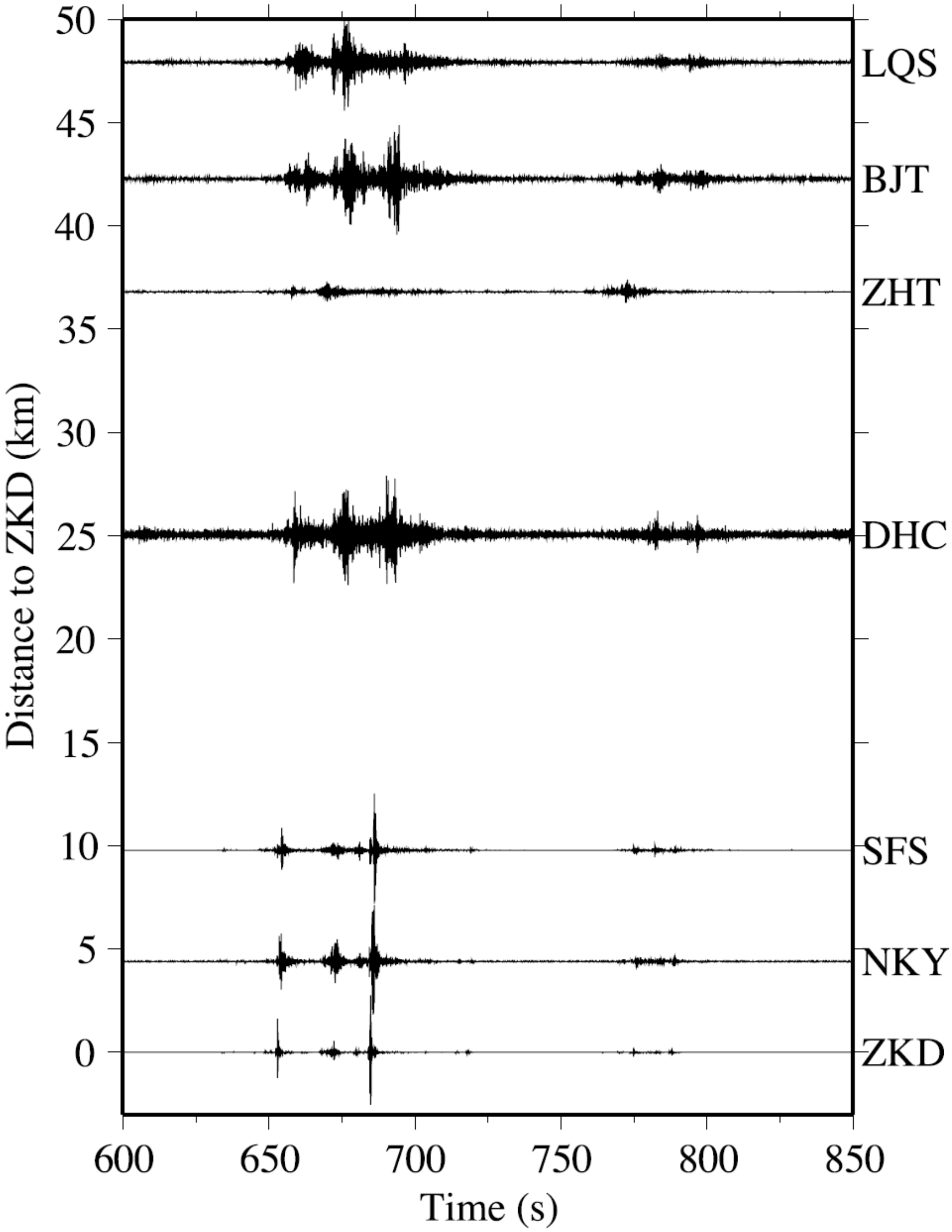

Figure 6.8 5 Hz High-pass-filtered seismograms aligned by the distance from the station ZKD during the surface waves of the Kunlun earthquake. Zero time is the Kunlun earthquake origin time.

As shown in Figure 6.1, the 5 triggered earthquakes are very close to the station NKY (< 20 km), and appear to be at shallow depth (< 5 km), just above the depth range of the background seismicity. I also find that the handpicked *S-P* times at station NKY for the triggered earthquakes are generally less than those for the background earthquakes (Figure 6.9), further suggesting that the triggered earthquakes are shallower or closer to the station NKY than the background earthquakes. The epicentral locations of these triggered earthquakes are near the boundaries of the Babaoshan/Huangzhang-Gaoliying faults and the Fangshan Pluton (Figure 6.1). Because the subsurface structures beneath this region are still not clear at this stage, I do not know whether the triggered earthquakes occur on the shallow portion of the normal faults, or on the boundary faults around the Fangshan Pluton.

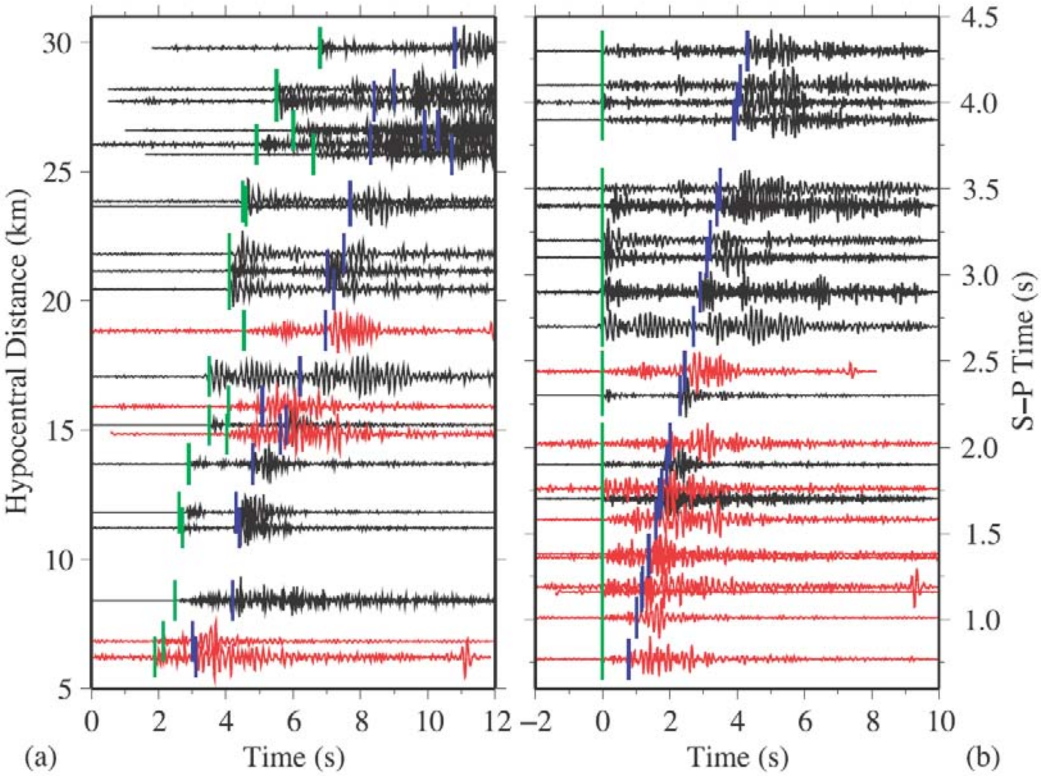

Figure 6.9 (a) 5 Hz High-pass-filtered seismograms of 5 located triggered (red) and 18 nearby (within 30km) background (black) events recorded at station NKY.

Seismograms are aligned by hypocentral distance from station NKY. Zero time is the event origin time. Green and blue vertical bars show the *P*- and *S*-arrival times, respectively. (b) 5 Hz High-pass-filtered seismograms aligned by the difference in *P*- and *S*-arrival times of 11 triggered (red) and 18 nearby (within 30km) background (black) events recorded at station NKY. Zero time is the *P*-arrival time. Only the waveforms for the located 5 events are plotted in (a), while the waveforms for all 11 triggered events at NKY are plotted in (b).

To examine whether the triggered earthquakes are regular or low-frequency earthquakes (e.g. Shelly *et al.* 2006) in the shallow crust, I compare the stacked spectra of 15 triggered earthquakes with the spectra of 18 nearby background earthquakes within 30 km of the station NKY (Figure 6.10). I use a 15 s time window starting 5 s before the handpicked *P*-arrivals to compute the spectra, and smooth the spectra with a moving window of 5 points. Due to the lack of accurate site response and attenuation for the medium, and the contamination of spectra in the lower frequency range (< 8 Hz) by the passage of teleseismic surface waves, I do not attempt to correct for the path and site effects and fit the source spectra. Alternatively, I shift the spectra to the same level so that I am able to compare the frequency content of the triggered vs. background events. I find that the spectra for triggered earthquakes show slightly faster decay rate in the frequency range of 10-20 Hz than those for background earthquakes (Figure 6.10b), suggesting that the triggered events may have lower corner frequencies than the background events However, because I did not correct for the path and site effects, the difference in the source spectra is not conclusive.

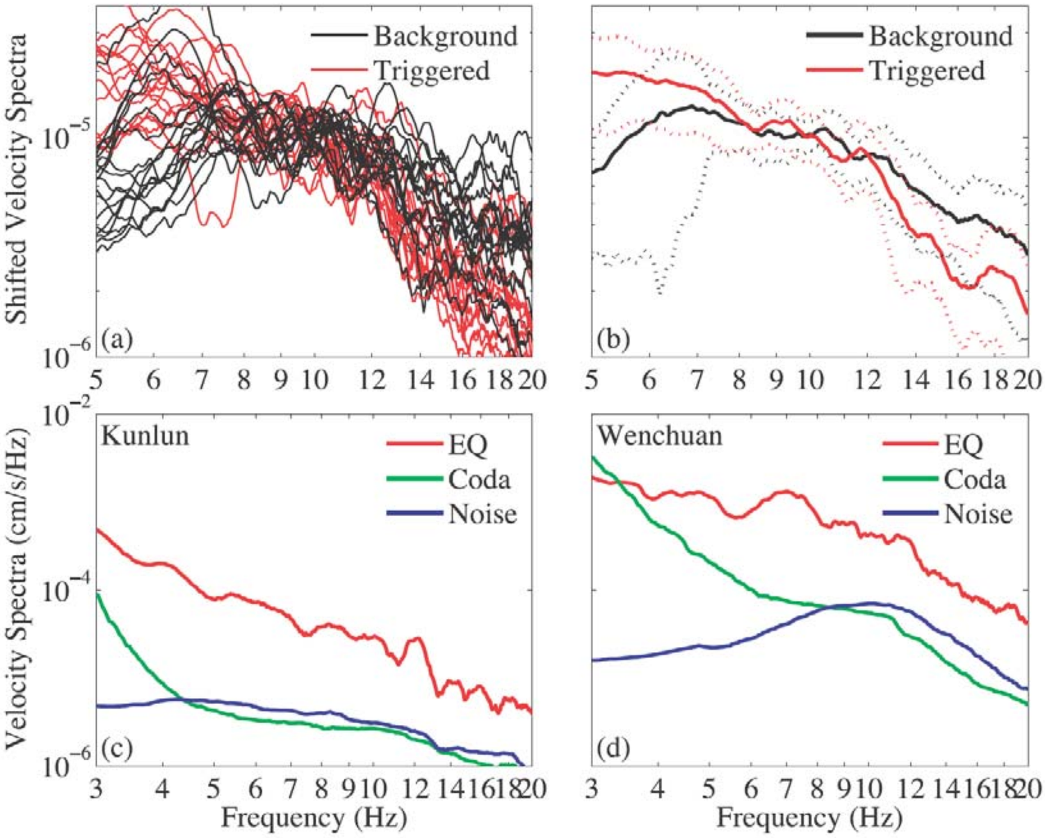

Figure 6.10. (a-b) Comparison of the shifted velocity spectra of the 15 triggered events (red solid line) and 18 nearby (within 30km) background events (black solid line). The spectra are computed from the whole waveform including both *P*- and *S*-waves. (a) Individual spectra of the triggered events (red) and the background events (black). The original velocity spectra are smoothed with half width of 1 Hz to remove the noisy spikes, and then shifted to the same level at the frequency range of 8-12 Hz for comparison of frequency content. (b) Stacked spectra of the triggered events (red solid line) and the background events (black solid line). The red and black dotted lines show the standard deviation for the spectra of triggered and background events, respectively. (c) Comparison of velocity spectra of triggered event (red), teleseismic coda (green), and background noise (blue) for the 2001 Kunlun earthquake. (d) Similar plot as (c) for the 2008 Wenchuan earthquake.

6.6 Modeling of Triggering Potential

To better explain our observations, I model the dynamic stress caused by the passage of Rayleigh and Love waves with an arbitrary incident angle on critically-stressed faults under the Coulomb failure criteria. The modeling procedure generally follows that of Hill (2008) and Gonzalez-Huizar & Velasco (2011) and is briefly described here.

For a right-hand coordinate system x_i where i =1,2,3, with the vertical axis (x_3) positive with depth, the displacements for the Rayleigh waves propagating in the x_1 direction are only in x_1 and x_3 directions (Stein & Wysession 2003):

$$u_1 = A_R k_1 \sin(\omega t - k_1 x)[\exp(-0.85 k_1 z) - 0.58 \exp(-0.39 k_1 z)] \tag{6.2}$$

$$u_3 = A_R k_1 \cos(\omega t - k_1 x)[-0.85 \exp(-0.85 k_1 z) + 1.47 \exp(-0.39 k_1 z)] \tag{6.3}$$

where A_R is the amplitude of the Rayleigh wave, ω is the angular frequency, k_1 is the horizontal wave number, and x_3 is the depth. The displacements for Love wave within a layer (thickness H = 35 km) over a half space is only in the x_2 direction (Stein & Wysession 2003):

$$u_2 = A_L \exp(i(\omega t - k_1 x_1))\cos\left(k_1 x_3 \sqrt{c_1^2 / \beta_1^2 - 1}\right) \tag{6.4}$$

where A_L is the amplitude of the Love wave, c_1 is the horizontal apparent velocity, and β_1 is the shear wave velocity within the top layer. For both the Rayleigh and Love waves, the strains induced by the displacements are (Stein & Wysession 2003):

$$\varepsilon_{ij} = \varepsilon_{ji} = \frac{1}{2}\left(u_{i,j} + u_{j,i}\right) \tag{6.5}$$

where $u_{i,j}$ is the first derivative of the displacement in the x_i direction relative to the x_j direction. For Poisson solid, the dynamic stresses (compression as negative) caused by the Rayleigh waves are (Gonzalez-Huizar & Velasco 2011):

$$\sigma_{ii} = \lambda\left(3\varepsilon_{ii} + \varepsilon_{jj}\right) \tag{6.6}$$

$$\sigma_{ij} = 2\lambda\varepsilon_{ij} \tag{6.7}$$

where λ is the Lamé constant, and $i = 1, j = 3$, or $i = 3, j = 1$, because Rayleigh wave propagating in x_1 direction do not introduce motion in the x_2 direction. The dynamic stresses caused by the Love waves are (Gonzalez-Huizar & Velasco 2011):

$$\sigma_{ij} = \sigma_{ji} = 2G\varepsilon_{ij} \tag{6.8}$$

where G is the shear modulus, and $i = 1, j = 2$, or $i = 3, j = 2$, because Love wave propagating in x_1 direction only introduce shear stresses in x_2 direction. Using Eq. 1-7, I model the dynamic stresses as a function of the wave incident angle, depth, and time, and then rotate the dynamic stresses σ_{ij} in coordinate system x_i to σ_{kl} in a new coordinate system y_i, where y_1, y_2, y_3, are the fault strike, fault dip, and fault plane normal directions, respectively, using two unitary matrices:

$$UM_1 = \begin{bmatrix} \cos(\theta) & \sin(\theta) & 0 \\ -\sin(\theta) & \cos(\theta) & 0 \\ 0 & 0 & 1 \end{bmatrix} \tag{6.9}$$

$$UM_2 = \begin{bmatrix} 1 & 0 & 0 \\ 0 & \cos(\delta) & -\sin(\delta) \\ 0 & \sin(\delta) & \cos(\delta) \end{bmatrix} \tag{6.10}$$

$$\sigma_{kl} = (UM_1 UM_2)^T \sigma_{ij} (UM_1 UM_2) \tag{6.11}$$

where θ and δ are the incident angles of the seismic waves and fault dip angle, respectively.

Finally I compute the triggering potential of a incident Rayleigh or Love wave, as the change in Coulomb failure function (Hill 2010):

$$\Delta CCF = \tau + \mu\sigma_n \tag{6.12}$$

where τ is the dynamic shear stress, σ_n is the dynamic normal stress acting on the fault plane, and μ is the friction coefficient. In our case, the triggered fault is likely to be normal as mentioned in Section 2.1, so the triggering potential is defined as (Gonzalez-Huizar & Velasco 2011)

$$P_N = -\tau_d + \mu\sigma_n \tag{6.13}$$

where τ_d is dynamic shear stress in the fault dip direction.

The model parameters I employed are $\lambda = G = 3\times10^{10}$ Pa, $\mu = 0.2$, 0.4 or 0.6, $f = 0.05$ Hz, $c_1 = 3.78$ km/s, $\beta_1 = 3.5$ km/s (Hill 2010), $\delta = 30°$ (for Babaoshan fault) or 70° (for Huangzhuang-Gaoliying fault). The output is the triggering potential as a function of wave incident angle θ from $0-360°$, depth from $0-30$ km, and time from $0-30$ s for a normal fault.

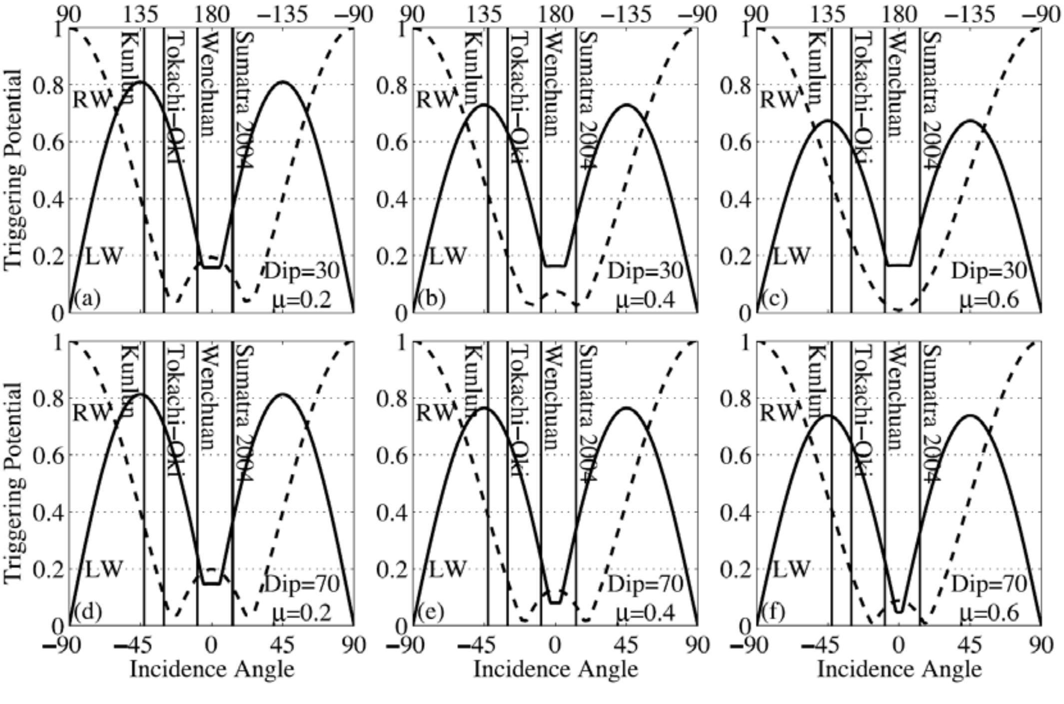

Figure 6.11 (a) Normalized Love (solid curve) and Rayleigh (dashed curve) wave triggering potential at depth of 4 km on a normal fault dipping at 30° assuming the coefficient of friction μ=0.2 and comparable displacement amplitudes at the surface for both types of surface waves. Incidence angle is measured counter-clockwise from

the fault strike direction (NW). The vertical solid lines show the incidence angle of the 4 large teleseismic earthquakes utilized in this study. (b)-(c) Similar plot as (a) for μ=0.4 and 0.6, respectively. (d)-(f) Similar plots as (a)-(c) for a normal fault dipping at 70°, and μ=0.2, 0.4, and 0.6, respectively.

The modeling results indicate that for the surface waves incident on a normal fault plane striking at NW direction, and dipping at 30° or 70° (Figure 6.1), the triggering potential of the Love wave is largest for teleseismic earthquakes with incidence angle around −135°, −45°, 45°, or 135°. The triggering potential of the Rayleigh wave is the highest for teleseismic earthquakes with incidence angle around −90° or 90° (Figure 6.11). I test our model using the dipping angles of the Babaoshan and Huangzhuang-Gaoliying faults (30° and 70°, see Figure 6.1c), combined with the coefficient of friction μ in the range of 0.2-0.6, and this does not change the overall shape of the triggering potentials (Figure 6.11). Our modeling results suggest that, based on the friction failure model, the triggering potentials for the Love and Rayleigh waves differ for different incident angles. Because the incidence angles for the four Mw>7.8 earthquakes used in this study span a range of only −15° to 45°, the available data do not allow a thorough test for our modeling results as shown in Figure 6.11.

6.7 Discussions

Our previous studies have identified clear triggering in continental China following the 2008 Wenchuan earthquake (Peng *et al.* 2010b; Jiang *et al.* 2010). This study provides additional evidence of dynamic triggering within intraplate regions near Beijing. I found that this region is repeatedly triggered by at least four large teleseismic earthquakes. This is consistent with recent observations in other intraplate regions (e.g. Gomberg *et al.* 2004; Velasco *et al.* 2008), and further suggests that dynamic triggering can occur in a wide range of tectonic environments. In addition, identification of multiple triggering cases at a specific site provides a unique chance to investigate the physical models and necessary conditions for dynamic triggering in intraplate regions.

6.7.1 Possible Mechanisms

As mentioned before, the physical models proposed to explain remotely triggered seismology are generally associated with frictional failure and/or excitation of crustal fluids/transient deformation (e.g. Hill & Prejean 2007). I note that the triggered earthquakes occurred during the first few cycles of the Love waves, and occurred again during the large amplitude Rayleigh waves (Figures 6.3-6.7). Recent studies of dynamically triggered earthquakes and tremors suggest that Rayleigh wave triggering could be explained by both Coulomb failure and fluid excitation, while Love wave triggering is more likely via Coulomb failure, because Love wave particle motions involve pure-shear strain with no volumetric component to excite fluid movements (Rubinstein *et al.* 2007b, 2009; Miyazawa *et al.* 2008; Peng & Chao 2008; Hill 2008; Peng *et al.* 2008, 2009, 2010a). In addition, most of the triggered earthquakes identified in this study are in phase with the passing surface waves without clear time delays (Figure 6.7), so they are better explained by the Coulomb failure criteria (Hill 2008, 2010; Gonzalez-Huizar & Velasco 2011). However, I only examine the continuous data within several hours after the *P*-arrival of each teleseismic earthquake due to the availability of continuous recording, so additional triggered earthquakes at later times associated with fluids or long-term aseismic creep (e.g. Prejean *et al.* 2004; Johnston *et al.* 2004) could escape our detection in the current study.

The aforementioned friction failure model generally assumes that the passage of seismic waves change the stress within the critically stressed local faults and trigger failure dynamically. Typically the effect of the passing seismic waves is quantified by the peak dynamic stress (PDS), which can be approximated from the PGV in a velocity seismogram (Hill *et al.* 1993). I examined PGV and PDS of the four teleseismic earthquakes recorded at NKY, the closest station to the epicenters of the triggered earthquakes, and I found that the vertical PGVs of the Kunlun, Tokachi-oki, 2004 Sumatra, and Wenchuan earthquakes are 0.69 cm/s, 0.59 cm/s, 0.91 cm/s, 1.27 cm/s, respectively. These PGVs would correspond to the PDSs in the range of 60~130 kPa, well above the triggering thresholds found at other regions (Brodsky & Prejean 2005; Peng *et al.* 2009; Van der Elst & Brodsky 2010). This is likely because the only available station during the entire study period is IC.BJT, which is about 50 km away from most of the triggered earthquakes around station NKY. Hence, I can only identify the most clear triggering case with large PGVs and

PDSs. In addition, the PGVs of the four analyzed teleseismic earthquakes at station IC.BJT are generally higher than other events, mostly because of their large magnitudes (~Mw>7.8) and relatively short propagation distances (Figure 6.2). This observation indicates that input wave amplitude plays an important role in controlling the triggering potential and the resulting amplitudes of the triggered events (Peng *et al.* 2009; Rubinstein *et al.* 2009; Chao *et al.* 2010).

In addition to the wave amplitude, other factors affecting the dynamic stress acting on the fault plane include the hypocentral depth, fault orientation, incident angle and type of seismic waves (Gonzalez-Huizar & Velasco 2011; Hill 2010). Our modeling results show that the triggering potential for the Love wave is larger than that for the Rayleigh wave for incidence angles ±45° on normal faults at depths of ~4km with dips of 30° and 70° (Figure 6.11). This is consistent with the observations that for the 2001 Kunlun, 2004 Sumatra and 2008 Wenchuan earthquakes, the locally triggered earthquakes during the Love wave generally have larger amplitudes than the local earthquakes during Rayleigh wave. For the 2003 Tokachi-oki earthquake, the triggered earthquakes during the Rayleigh wave have larger amplitudes than during the Love wave. This could be explained by the fact that the Rayleigh wave amplitude is above 3 times the Love wave amplitude, while our simple modeling analysis assumes equal surface displacement amplitudes for both the Love and Rayleigh waves. I note that the incident angles of the surface waves for the 2004 Sumatra and 2008 Wenchuan earthquakes are in the range of relatively lower triggering potentials for both Love and Rayleigh waves (−15° to 15°, see Figure

6.11). However, I still observe clear dynamic triggering for the two wave types (Figure 6.4 and Figure 6.6). This is probably due to the fact that the PGVs at our study region for both Sumatra and Wenchuan earthquakes are higher than other teleseismic events. As mentioned before, the observations and modeling results are somewhat limited by the small number of available teleseismic events and the relatively simple modeling, and the PGVs and other factors in dynamic triggering are still not clear at this point. Systematic studies of a larger dataset and detailed waveform modeling would be helpful to better constrain the physical models of remote triggering in this and other tectonic environments.

6.7.2 Comparison of Triggered and Background Events

The 5 triggered earthquakes with hypocentral locations all occurred at shallow depth (< 5 km), above the depth range of background seismicity (Figure 6.1b). One potential cause of shallow depth could be the reduction of seismic velocity in the shallow crust during the passage of large-amplitude surface waves. However, the reductions of seismic velocities are generally on the order of a few percent for large nearby earthquakes (Vidale & Li 2003; Rubinstein & Beroza 2004a; Peng & Ben-Zion 2006; Chao & Peng 2009). For teleseismic earthquakes, the velocity reduction could be on the order of 0.2% or even smaller (Zhao *et al.* 2010). This would translate into only a few tens of meters in depth uncertainty at most. In addition, I have examined the *S-P* times of the triggered earthquakes and found that they are generally smaller than those of the background earthquakes (Figure 6.9).

As briefly mentioned before, the waveforms of the triggered earthquakes do not correlate with those of the background seismicity, indicating that these shallow earthquakes may not occur if they were not triggered. In other words, these events, which are likely located near the velocity strengthening regions in the shallow crust (Marone & Scholz 1988), are normally aseismic and can only be driven into brittle failure by relatively large dynamic stresses of few tens of KPa or larger (Sleep & Ma 2008; Fischer & Sammis 2009). Such interpretation is also consistent with the fact that the observed spectra of the triggered earthquakes have faster decays at high frequency ranges than those for the nearby background earthquakes (Figure 6.10), an indicative of slow earthquakes in the shallow crust (Peng & Gomberg 2010, and references therein). However, the path effects during wave propagation, especially the apparent fast decay due to the lower Q in the shallow crust, could also modify the frequency content of the spectra. I cannot completely rule out the path and other effects at this stage because there is no background seismicity at the immediate vicinity of the triggered earthquakes. This will be addressed in future work when additional information and data become available.

As noted before, these shallow triggered earthquakes appear to be in phase with the passing surface waves (Figure 6.7), similar to the recent observations of triggered deep tremor (e.g. Rubinstein *et al.* 2007b, 2009; Peng & Chao 2008; Peng *et al.* 2008, 2009; Miyazawa & Brodsky 2008; Miyazawa *et al.* 2008; Gomberg *et al.* 2008; Ghosh *et al.* 2009) and low-frequency earthquakes (Tang *et al.* 2010; Peng *et al.*

2010a). Together with their shallow depths and low frequency contents, I infer that these triggered earthquakes may occur near the transition zone between the velocity strengthening and weakening zones in the top few kms of the fault (Marone & Scholz 1988), which could be considered as the counterpart of the deep tremor and slow-slip events that occurred below the seismogenic zone in the lower crust. I note that the shallow portion of the Babaoshan fault is currently creeping (Che *et al.* 1997; Che & Fan 2003). In addition, clear strain steps have been observed in the nearby borehole strain meters during the 2004 Sumatra and 2008 Wenchuan earthquakes (Aifu Niu, personal communication, 2009), and other places in north China during the 2001 Mw7.8 Kunlun earthquake (Qiu & Shi 2004). I hypothesize that the passing surface waves of the teleseismic earthquakes may trigger micro slow-slip events (Shelly *et al.* 2011) in the shallow portion of the creeping faults, which generate the transient strain step observed in the strain meters. This aseismic motion triggers more rapid slip on scattered regions of the fault that radiate seismic waves (Peng & Gomberg 2010) that are observed on the broadband high-gain seismometers as triggered earthquakes. An alternative hypothesis is that the triggered earthquakes are large and shallow enough to produce the observed strain signals. These hypotheses can be tested by an integrative analysis of the borehole strain meters and seismometers.

Finally, it is worth noting that the modeling of the triggering potential and some discussions are based on the assumption that the triggered earthquakes occur on the NW-striking normal faults. However, these earthquakes also appear to be around the Fangshan Pluton (Figure 6.1). Because of the uncertainties in the subsurface structures in this region, the host of the triggered earthquakes is still not clear at this stage. We are in the process of carrying out a dense seismic deployment around this region to improve earthquake locations and better understand the subsurface fault structures. The results from this ongoing deployment will be reported in subsequent studies.

CHAPTER 7

CONCLUSION

The aim of this thesis is to investigate the effects of passing seismic waves on the properties and additional brittle failures within the Earth. Specifically, the second chapter shows clear co-seismic changes in fault zone site response and logarithmic recovery after the Mw7.1 Duzce earthquake in Turkey, indicating nonlinear wave propagation effect within the shallow fault zones. In the third to the fifth chapters, observations of temporal changes in site response associated with both large and medium earthquakes are presented, indicating the seismic waves could also cause nonlinearity in shallow sedimentary layers. In the sixth chapter, I presented clear observations of shallow earthquakes in an intraplate setting near Beijing, China, instantaneously triggered by passing surface waves of 4 teleseismic events, indicating the dynamic stress caused by passing seismic waves not only produce nonlinearity at shallow depth, but also trigger the fault slip and brittle failure as well.

Although many efforts have been made in the last several decades to investigate nonlinear wave propagation effects, the controlling parameters and mechanisms of the nonlinearity are still not fully understood. Recently, several studies (e.g. Brenguier *et al.* 2008) used cross correlations of ambient noise to extract the empirical Green's functions between station pair, and found clear co-seismic damage at shallow FZ and stress changes at depth after large earthquakes. However, the noise cross-correlation technique requires relatively long continuous data for averaging and hence is only suitable for monitoring relatively longer-term temporal changes (i.e., > 1 day). The sliding-window spectral ratio method used in this thesis is a simple and robust approach to investigate temporal changes of site response where a pair of target and reference stations is available. This technique could be applied to track co-seismic changes and subsequent recovery after large earthquakes in the first few hundred seconds after large earthquakes. The results based on the sliding-window spectral ratio method presented in the second to the fifth chapters established clear causal relationship between the input ground motion and the degree of nonlinearity from several tens of Gal to more than 1000 Gal. In additional, two forms of nonlinear site response (with and without additional damage) are proposed to explain the observed co-seismic changes and subsequent recovery at different PGA levels.

Recent observations of remote triggering of micro-earthquakes and non-volcanic tremor introduce another approach to investigate the wave propagation effects on deep faults. Many studies have suggested that tremor is very sensitive to external stress perturbations, and can be triggered by dynamic stresses on the order of a few kPa (e.g. Peng & Chao 2008; Rubinstein *et al.* 2009; Peng *et al.* 2010a). Because of such stress sensitivity, tremor could be used as an indicator of the time-varying stress fields associated with both regular and slow earthquakes. However, it is still not clear what are the necessary conditions and what are the underlying mechanisms for the dynamic triggering of microearthquakes and tremor, and the various hypotheses are still yet to be tested by the increasing seismic data set. The results in the sixth chapter suggest PGV, type, and incident angle of the incident surface waves as important controlling parameters for the dynamic triggering.

After the occurrence of several recent large earthquakes (e.g., the 2010 Mw8.8 Chile earthquake, the 2010 Mw7.2 and 2011 Mw6.3 New Zealand earthquakes, and the 2011 Mw9.0 Tohoku earthquake), many high-quality digital seismograms become immediately available for seismological research. The newly available data will undoubtedly provide unprecedented opportunities to study how seismic waves could affect material properties and trigger additional seismic events at near-field and long-range distances. The methods outlined in this thesis could be easily employed by other researchers to extract useful information from the massive dataset. Hopefully the new information will improve our understanding of some important topics in earthquake seismology, including seismic/aseismic fault behavior, rock rheology, earthquake initiation and interaction, and finally help to better estimate the earthquake hazard, and mitigate the loss of future earthquakes.

REFERENCES

Aki, K., 1969. Analysis of the Seismic Coda of Local Earthquakes as Scattered Waves, *J. Geophys. Res.,* **74,** 615-631.

Aki, K. & Chouet, B., 1975. Origin of coda waves: Source, attenuation, and scattering effects, *J. Geophys. Res.,* **80,** 3322-3342.

Aoi, S., Kunugi, T., Suzuki, W., Morikawa, N., Nakamura, H., Pulido, N., Shiomi, K. & Fujiwara, H., 2011. Strong motion characteristics of the 2011 Tohoku-oki earthquake from K-NET and KiK-NET, *SSA Annual Meeting*.

Aoi, S., Obara, K., Hori, S., Kasahara, K. & Okada, Y., 2000. New Japanese uphole/downhole strong-motion observation network: KiK-net, *Seism. Res. Lett,* **72,** 239.

Assimaki, D., Li, W., Steidl, J. & Tsuda, K., 2008. Site Amplification and Attenuation via Downhole Array Seismogram Inversion: A Comparative Study of the 2003 Miyagi-Oki Aftershock Sequence, *Bull. Seism. Soc. Am.,* **98,** 301-330.

Aster, R. & Shearer, P., 1991. High-frequency borehole seismograms recorded in the San Jcinto Fault zone, Southern California Part 2. Attenuation and site effects, *Bull. Seism. Soc. Am.,* **81,** 1081-1100.

Ben-Zion, Y., 1998. Properties of seismic fault zone waves and their utility for imaging low-velocity structures, *J. Geophys. Res.,* **103,** 12567-12585.

Ben-Zion, Y. & Aki, K., 1990. Seismic radiation from an SH line source in a laterally heterogeneous planar fault zone, *Bull. Seism. Soc. Am.,* **80,** 971-994.

Ben-Zion, Y., Peng, Z., Okaya, D., Seeber, L., Armbruster, J., Ozer, N., Michael, A., Baris, S. & Aktar, M., 2003. A shallow fault-zone structure illuminated by trapped waves in the Karadere-Duzce branch of the North Anatolian Fault, western Turkey, *Geophys. J. Int.,* **152,** 699-717.

Ben-Zion, Y. & Sammis, C., 2003. Characterization of fault zones, *Pure Appl. Geophys.,* **160,** 677-715.

Ben-Zion, Y. & Shi, Z., 2005. Dynamic rupture on a material interface with spontaneous generation of plastic strain in the bulk, *Earth Planet. Sci. Lett.,* **236,** 486-496.

Beresnev, I., Atkinson, G., Johnson, P. & Field, E., 1998. Stochastic finite-fault modeling of ground motions from the 1994 Northridge, California, earthquake. II. Widespread Nonlinear response at soil sites, *Bull. Seism. Soc. Am.,* **88,** 1402-1410.

Beresnev, I. & Wen, K., 1996a. Nonlinear soil response-A reality?, *Bull. Seism. Soc. Am.,* **86,** 1964-1978.

Beresnev, I. & Wen, K., 1996b. The possiblity of observing nonlinear path effect in earthquake-induced seismic wave propagation, *Bull. Seism. Soc. Am.,* **86,** 1028-1041.

Bokelmann, G. & Harjes, H., 2000. Evidence for temporal variation of seismic velocity within the upper continental crust, *J. Geophys. Res.,* **105,** 23.

Brenguier, F., Campillo, M., Hadziioannou, C., Shapiro, N., Nadeau, R. & Larose, E., 2008. Postseismic relaxation along the San Andreas fault at Parkfield from continuous seismological observations, *Science,* **321,** 1478.

Brodsky, E., Karakostas, V. & Kanamori, H., 2000. A new observation of dynamically triggered regional seismicity: Earthquakes in Greece following the August, 1999 Izmit, Turkey earthquake, *Geophys. Res. Lett,* **27,** 2741-2744.

Brodsky, E. & Prejean, S., 2005. New constraints on mechanisms of remotely triggered seismicity at Long Valley Caldera, *J. Geophys. Res,* **110,** B04302, doi:04310.01029/02004JB003211.

Brodsky, E., Roeloffs, E., Woodcock, D., Gall, I. & Manga, M., 2003a. A mechanism for sustained groundwater pressure changes induced by distant earthquakes, *J. Geophys. Res,* **108,** B8, doi:10.1029/2002JB002321.

Brodsky, E., Roeloffs, E., Woodcock, D., Gall, I. & Manga, M., 2003b. A mechanism for sustained groundwater pressure changes induced by distant earthquakes, *J. Geophys. Res,* **108,** 2390.

Brodsky, E., Sturtevant, B. & Kanamori, H., 1998. Earthquakes, volcanoes, and rectified diffusion, *J. Geophys. Res.,* **103,** 23,827–823,838.

Castro, R., Mucciarelli, M., Pacor, F. & Petrungaro, C., 1997. S-wave site-response estimates using horizontal-to-vertical spectral ratios, *Bull. Seism. Soc. Am.,* **87,** 256.

Chao, K. & Peng, Z., 2009. Temporal changes of seismic velocity and anisotropy in the shallow crust induced by the 1999 October 22 M6. 4 Chia-Yi, Taiwan earthquake, *Geophys. J. Int.,* **179,** 1800-1816.

Chao, K., Peng, Z., Wu, C., Tang, C.-C. & Lin, C.H., 2010. Remote triggering of non-volcanic tremor around Taiwan, *Geophys. J. Int.***,** in review.

Che, Z. & Fan, Y., 2003. Tracing study of fault activity of the Beijing Huangzhuang-Gaoliying fault and Babaoshan fault in recent time, *Earthquake,* **23,** 97-104.

Che, Z., Gong, Y., Liu, S., Liu, T. & Meng, G., 1997. Comprehensive Study of Fault Activity of the Huangzhuang-Gaoliying and Babaoshan Fault in the Middle Section, *Earthquake Research in China,* **13,** 330-337.

Chen, L., Tao, W., Zhao, L. & Zheng, T., 2008. Distinct lateral variation of lithospheric thickness in the Northeastern North China Craton, *Earth Planet. Sci. Lett.,* **267,** 56-68.

Chen, Q., Chen, Y. & Li, L., 2006. China digital seismic network improves coverage and quality, *Eos Tran. AGU,* **87,** doi:10.1029/2006EO300003.

Chin, B. & Aki, K., 1991. Simultaneous study of the source, path, and site effects on strong ground motion during the 1989 Loma Prieta earthquake: A preliminary result on pervasive nonlinear site effects, *Bull. Seism. Soc. Am.,* **81,** 1859-1884.

Chun, K., Henderson, G. & Liu, J., 2004. Temporal changes in P wave attenuation in the Loma Prieta rupture zone, *J. Geophys. Res,* **109,** B02317.

Deng, Q., Zhang, P., Ran, Y., Yang, X., Min, W. & Chu, Q., 2003. Basic characteristics of active tectonics of China, *Science in China Series D: Earth Sciences,* **46,** 356-372.

Dieterich, J. & Kilgore, B., 1996. Imaging surface contacts: power law contact distributions and contact stresses in quartz, calcite, glass and acrylic plastic, *Tectonophysics,* **256,** 219-239.

Dobry, R., Borcherdt, R., Crouse, C., Idriss, I., Joyner, W., Martin, G., Power, M., Rinne, E. & Seed, R., 2000. New site coefficients and site classification system used in recent building seismic code provisions, *Earthquake Spectra,* **16,** 41-67.

Elkhoury, J., Brodsky, E. & Agnew, D., 2006. Seismic waves increase permeability, *Nature,* **441,** 1135-1138.

Enescu, B., Mori, J. & Miyazawa, M., 2007. Quantifying early aftershock activity of the 2004 mid-Niigata Prefecture earthquake (M w 6.6), *J. Geophys. Res,* **112**.

EPRI, 1993. Guidelines for determining design basis ground motions, *Electric Power Research Institute Technical Report*, pp. *EPRI TR-102293*.

Field, E.H., Johnson, P.A., Beresnev, I.A. & Zeng, Y.H., 1997. Nonlinear ground-motion amplification by sediments during the 1994 Northridge earthquake, *Nature,* **390,** 599-602.

Finzi, Y., Hearn, E., Ben-Zion, Y. & Lyakhovsky, V., 2009. Structural properties and deformation patterns of evolving strike-slip faults: numerical simulations incorporating damage rheology, *Pure appl. Geophys,* 1537-1573.

Fischer, A. & Sammis, C., 2009. Dynamic driving of small shallow events during strong motion, *Bull. Seism. Soc. Am.,* **99,** 1720.

Frankel, A., Mueller, C., Barnhard, T., Leyendecker, E., Wesson, R., Harmsen, S., Klein, F., Perkins, D., Dickman, N. & Hanson, S., 2000. USGS National Seismic Hazard Maps, *Earthquake Spectra,* **16,** 1-19.

Freed, A., 2005. Earthquake triggering by static, dynamic, and postseismic stress transfer, *Annu. Rev. Earth Planet. Sci,* **33,** 335-367.

Ghosh, A., Vidale, J., Peng, Z., Creager, K. & Houston, H., 2009. Complex non-volcanic tremor near Parkfield, California, triggered by the great 2004 Sumatra earthquake, *J. Geophys. Res,* **114,** B00A15, doi:10.1029/2008JB006062.

Goldstein, P., Dodge, D., Firpo, M. & Minner, L., 2003. SAC2000: Signal processing and analysis tools for seismologists and engineers. *in In The IASPEI International Handbook of Earthquake and Engineering Seismology, Part B, Chap 85.5*, eds Lee, W. H. K., Kanamori, H., Jennings, P. C. & Kisslinger, C. Academic Press, London.

Gomberg, J., Blanpied, M. & Beeler, N., 1997. Transient triggering of near and distant earthquakes, *Bull. Seism. Soc. Am.,* **87,** 294-309.

Gomberg, J., Bodin, P., Larson, K. & Dragert, H., 2004. Earthquakes nucleated by transient deformations fundamental process evident in observations surrounding the M7. 9 Denali Fault Alaska Earthquake, *Nature,* **427,** 621-624.

Gomberg, J., Reasenberg, P., Bodin, P. & Harris, R., 2001. Earthquake triggering by seismic waves following the Landers and Hector Mine earthquakes, *Nature,* **411,** 462-466.

Gomberg, J., Reasenberg, P., Cocco, M. & Belardinelli, M., 2005. A frictional population model of seismicity rate change, *J. Geophys. Res,* **110,** B05S03, doi:10.1029/2004JB003404.

Gomberg, J., Rubinstein, J., Peng, Z., Creager, K., Vidale, J. & Bodin, P., 2008. Widespread triggering of nonvolcanic tremor in California, *Science,* **319,** 173.

Gonzalez-Huizar, H. & Velasco, A.A., 2011. Dynamic triggering: Stress modeling and a case study, *J. Geophys. Res.,* **116,** B02304.

Hamiel, Y., Liu, Y., Lyakhovsky, V., Ben-Zion, Y. & Lockner, D., 2004. A viscoelastic damage model with applications to stable and unstable fracturing, *Geophys. J. Int.,* **159,** 1155-1165.

Hartzell, S., 1998. Variability in nonlinear sediment response during the 1994 Northridge, California, earthquake, *Bull. Seism. Soc. Am.,* **88,** 1426-1437.

Hayes, G., Earle, P., Wald, D., Benz, H. & Briggs, R., 2011. The USGS-NEIC response to the 2011/03/11 Mw9.0 Tohoku earthquake - magnitude and rupture modeling, *SSA Annual Meeting*.

Herece, E. & Akay, E., 2003. 1: 100.000 geological maps of the North Anatolian Fault, Appendix 3 and 4, *of Miner. Res. and Explor., Ankara*.

Hill, D., 2008. Dynamic stresses, Coulomb failure, and remote triggering, *Bull. Seism. Soc. Am.,* **98,** 66-92.

Hill, D., 2010. Surface Wave Potential for Triggering Tectonic (Non-Volcanic) Tremor, *Bull. Seism. Soc. Am.,* **100,** 1859-1878.

Hill, D., Pollitz, F. & Newhall, C., 2002. Earthquake-volcano interactions, *Physics Today,* **55,** 41-47.

Hill, D. & Prejean, S., 2007. Dynamic triggering. *in Earthquake Seismology Treatise on Geophysics*, pp. 257-291, ed. Kanamori, H. Elsevier, Amsterdam.

Hill, D., Reasenberg, P., Michael, A., Arabaz, W., Beroza, G., Brumbaugh, D., Brune, J., Castro, R., Davis, S. & DePolo, D., 1993. Seismicity remotely triggered by the magnitude 7.3 Landers, California, earthquake, *Science,* **260,** 1617-1623.

Hough, S., 2005. Remotely Triggered Earthquakes Following Moderate Mainshocks (or, Why California Is Not Falling into the Ocean), *Seism. Res. Lett.,* **76,** 58-66.

Hough, S. & Kanamori, H., 2002. Source properties of earthquakes near the Salton Sea triggered by the 16 October 1999 M 7.1 Hector Mine, California, earthquake, *Bull. Seism. Soc. Am.,* **92,** 1281-1289.

Hough, S., Seeber, L. & Armbruster, J., 2003. Intraplate triggered earthquakes: Observations and interpretation, *Bull. Seism. Soc. Am.,* **93,** 2212-2221.

Jiang, T., Peng, Z., Wang, W.J. & Chen, Q.F., 2010. Remotely triggered seismicity in Continental China by the 2008 Mw7.9 Wenchuan earthquake, *Bull. Seism. Soc. Am.,* **100(5B),** 5274–5289, doi: 5210.1785/0120090286.

Johnson, P., Bodin, P., Gomberg, J., Pearce, F., Lawrence, Z. & Menq, F., 2009. Inducing in situ, nonlinear soil response applying an active source, *J. Geophys. Res.,* **114,** B05304, doi:05310.01029/02008JB005832.

Johnson, P. & Jia, X., 2005. Nonlinear dynamics, granular media and dynamic earthquake triggering, *Nature,* **7060,** 871-874, doi:810.1038/nature04015.

Johnson, P. & Sutin, A., 2005. Slow dynamics and anomalous nonlinear fast dynamics in diverse solids, *The Journal of the Acoustical Society of America,* **117,** 124-130.

Johnston, M., Prejean, S. & Hill, D., 2004. Triggered deformation and seismic activity under Mammoth mountain in Long Valley Caldera by the 3 November 2002 Mw 7.9 Denali Fault earthquake, *Bull. Seism. Soc. Am.,* **94,** S360-S369.

Joyner, W., Warrick, R. & Oliver, A., 1976. Analysis of seismograms from a downhole array in sediments near San Francisco Bay, *Bull. Seism. Soc. Am.,* **66,** 937-958.

Karabulut, H. & Bouchon, M., 2007. Spatial variability and non-linearity of strong ground motion near a fault, *Geophys. J. Int.,* **170,** 262-274.

Kilb, D., Gomberg, J. & Bodin, P., 2002. Aftershock triggering by complete Coulomb stress changes, *J. Geophys. Res,* **107,** B4, doi:10.1029/2001JB000202.

Klein, F., 2002. User's guide to HYPOINVERSE-2000, a Fortran program to solve for earthquake locations and magnitudes, *US Geol. Surv. Open-File Rept***,** 02-171.

Kramer, S. & Paulsen, S., 2004. Practical use of geotechnical site response models, *in Proc. Int. Workshop on Uncertainties in Nonlinear Soil Properties and their Impact on Modeling Dynamic Soil Response,* University of California Berkeley, 10.

Lewis, M.A. & Ben-Zion, Y., 2010. Diversity of fault zone damage and trapping structures in the Parkfield section of the San Andreas Fault from comprehensive analysis of near fault seismograms, *Geophys. J. Int.***,** in review.

Li, Y., Chen, P., Cochran, E., Vidale, J. & Burdette, T., 2006. Seismic evidence for rock damage and healing on the San Andreas Fault associated with the 2004 M 6.0 Parkfield earthquake, *Bull. Seism. Soc. Am.,* **96,** 349-363.

Li, Y., Leary, P., Aki, K. & Malin, P., 1990. Seismic trapped modes in the Oroville and San Andreas fault zones, *Science,* **249,** 763-766.

Li, Y., Vidale, J., Aki, K., Xu, F. & Burdette, T., 1998. Evidence of Shallow Fault Zone Strengthening After the 1992? M7. 5 Landers, California, Earthquake, *Science,* **279,** 217.

Linde, A. & Sacks, I., 1998. Triggering of volcanic eruptions, *Nature,* **395,** 888-890.

Liu, R., Wu, Z., Yin, C., Chen, Y. & Zhuang, C., 2003. Development of China digital seismological observational systems, *Acta Seismologica Sinica,* **16,** 568-573.

Liu, Y., Teng, T. & Ben-Zion, Y., 2005. Near-surface seismic anisotropy, attenuation and dispersion in the aftershock region of the 1999 Chi-Chi earthquake, *Geophys. J. Int.,* **160,** 695-706.

Lyakhovsky, V. & Ben-Zion, Y., 2008. Scaling relations of earthquakes and aseismic deformation in a damage rheology model, *Geophys. J. Int.,* **172,** 651-662.

Lyakhovsky, V., Ben-Zion, Y. & Agnon, A., 1997. Distributed damage, faulting, and friction, *J. Geophys. Res,* **102,** 635–627.

Lyakhovsky, V., Hamiel, Y., Ampuero, J. & Ben-Zion, Y., 2009. Non-linear damage rheology and wave resonance in rocks, *Geophys. J. Int.,* **178,** 910-920.

Manga, M. & Wang, C., 2007. Earthquake hydrology, *Treatise on geophysics,* **4,** 293–320.

Marone, C., 1998. Laboratory-derived friction laws and their application to seismic faulting, *Annual Reviews in Earth and Planetary Sciences,* **26,** 643-696.

Marone, C. & Scholz, C., 1988. The depth of seismic faulting and the upper transition from stable to unstable slip regimes, *Geophys. Res. Lett.,* **15,** 621-624.

Matthews, M. & Reasenberg, P., 1988. Statistical methods for investigating quiescence and other temporal seismicity patterns, *Pure Appl. Geophys.,* **126,** 357-372.

Mayeda, K., Malagnini, L. & Walter, W., 2007. A new spectral ratio method using narrow band coda envelopes: Evidence for non-self-similarity in the Hector Mine sequence, *Geophys. Res. Lett.,* **34,** L11303, doi:11310.11029/12007GL030041.

McGuire, R., 2004. Seismic hazard and risk analysis, Earthquake Engineering Research Institute, Oakland, California.

Miyazawa, M. & Brodsky, E., 2008. Deep low-frequency tremor that correlates with passing surface waves, *J. Geophys. Res.,* **113,** B01307, doi:01310.01029/02006JB004890.

Miyazawa, M., Brodsky, E. & Mori, J., 2008. Learning from dynamic triggering of low-frequency tremor in subduction zones, *Earth Planets Space,* **60,** e17-e20.

Miyazawa, M. & Mori, J., 2006. Evidence suggesting fluid flow beneath Japan due to periodic seismic triggering from the 2004 Sumatra-Andaman earthquake, *Geophys. Res. Lett.,* **33,** L05303.

NEHRP, 2003. NEHRP recommended provisions for seismic regulations for new buildings and other structures (FEMA 450), *National Earthquake Hazards*

Reduction Program (NEHRP), Building Seismic Safety Council, Washington, DC.

Ostrovsky, L. & Johnson, P., 2001. Dynamic nonlinear elasticity in geomaterials, *Rivista del Nuovo Cimento,* **24,** 1-46.

Pankow, K., Arabasz, W., Pechmann, J. & Nava, S., 2004. Triggered seismicity in Utah from the 3 November 2002 Denali fault earthquake, *Bull. Seism. Soc. Am.,* **94,** S332-S347.

Pasqualini, D., Heitmann, K., TenCate, J., Habib, S., Higdon, D. & Johnson, P., 2007. Nonequilibrium and nonlinear dynamics in Berea and Fontainebleau sandstones: Low-strain regime, *J. Geophys. Res,* **112,** B01204, doi:01210.01029/02006JB004264.

Pavlenko, O. & Irikura, K., 2002a. Changes in Shear Moduli of Liquefied and Nonliquefied Soils during the 1995 Kobe Earthquake and Its Aftershocks at Three Vertical-Array Sites, *Bull. Seism. Soc. Am.,* **92,** 1952-1969.

Pavlenko, O. & Irikura, K., 2002b. Nonlinearity in the response of soils in the 1995 Kobe earthquake in vertical components of records, *Soil. Dyn. Earthquake Eng.,* **22,** 967-975.

Pavlenko, O. & Irikura, K., 2003. Estimation of Nonlinear Time-dependent Soil Behavior in Strong Ground Motion Based on Vertical Array Data, *Pure Appl. Geophys.,* **160,** 2365-2379.

Peng, Z. & Ben-Zion, Y., 2004. Systematic analysis of crustal anisotropy along the Karadere–Düzce branch of the North Anatolian fault, *Geophys. J. Int.,* **159,** 253-274.

Peng, Z. & Ben-Zion, Y., 2005. Spatiotemporal variations of crustal anisotropy from similar events in aftershocks of the 1999 M7. 4 Izmit and M7. 1 Düzce, Turkey, earthquake sequences, *Geophys. J. Int.,* **160,** 1027-1043.

Peng, Z. & Ben-Zion, Y., 2006. Temporal changes of shallow seismic velocity around the Karadere-Düzce branch of the north Anatolian fault and strong ground motion, *Pure Appl. Geophys.,* **163,** 567-600.

Peng, Z., Ben-Zion, Y., Michael, A. & Zhu, L., 2003. Quantitative analysis of seismic fault zone waves in the rupture zone of the 1992 Landers, California, earthquake: evidence for a shallow trapping structure, *Geophys. J. Int.,* **155,** 1021-1041.

Peng, Z. & Chao, K., 2008. Non-volcanic tremor beneath the Central Range in Taiwan triggered by the 2001 Mw 7.8 Kunlun earthquake, *Geophys. J. Int.,* **175,** 825-829.

Peng, Z. & Gomberg, J., 2010. An integrative perspective of coupled seismic and aseismic slow slip phenomena, *Nature Geoscience***,** doi: 10.1038/ngeo1940.

Peng, Z., Hill, D.P., Shelly, D.R. & Aiken, C., 2010a. Remotely triggered microearthquakes and tremor in Central California following the 2010 Mw8.8 Chile Earthquake, *Geophys. Res. Lett.***,** doi:10.1029/2010GL045462, in press.

Peng, Z., Long, L.T. & Zhao, P., 2011a. The relevance of high-frequency analysis artifacts to remote triggering, *Bull. Seism. Soc. Am.,* in review.

Peng, Z., Vidale, E., Ishii, M. & Helmstetter, A., 2007. Seismicity rate immediately before and after mainshock rupture from high-frequency waveforms in Japan, *J. Geophys. Res.,* **112,** B03306.

Peng, Z., Vidale, J., Creager, K., Rubinstein, J., Gomberg, J. & Bodin, P., 2008. Strong tremor near Parkfield, CA, excited by the 2002 Denali Fault earthquake, *Geophys. Res. Lett.,* **35,** L23305, doi:23310.21029/22008GL036080.

Peng, Z., Vidale, J. & Houston, H., 2006. Anomalous early aftershock decay rate of the 2004 Mw6. 0 Parkfield, California, earthquake, *Geophys. Res. Lett,* **33,** 17.

Peng, Z., Vidale, J., Wech, A., Nadeau, R. & Creager, K., 2009. Remote triggering of tremor along the San Andreas Fault in central California, *J. Geophys. Res,* **114,** B00A06, doi:10.1029/2008JB006049.

Peng, Z., Wang, W.J., Chen, Q.F. & Jiang, T., 2010b. Remotely triggered seismicity in north China following the 2008 Mw 7.9 Wenchuan earthquake, *Earth Planets Space,* **62,** 893-898.

Peng, Z., Wu, C. & Aiken, C., 2011b. Delayed triggering of microearthquakes by multiple surface waves circling the Earth, *Geophys. Res. Lett.,* **38,** L04306.

Peng, Z. & Zhao, P., 2009. Migration of early aftershocks following the 2004 Parkfield earthquake, *Nature Geoscience*.

Perfettini, H., Schmittbuhl, J. & Cochard, A., 2003. Shear and normal load perturbations on a two-dimensional continuous fault: 2. Dynamic triggering, *J. Geophys. Res,* **108,** B9, 2409, doi:2410.1029/2002JB001805.

Phillips, W.S. & Aki, K., 1986. Site amplification of coda waves from local earthquakes in central California, *Bull. Seism. Soc. Am.,* **76,** 627.

Prejean, S., Hill, D., Brodsky, E., Hough, S., Johnston, M., Malone, S., Oppenheimer, D., Pitt, A. & Richards-Dinger, K., 2004. Remotely triggered seismicity on the United States west coast following the Mw 7.9 Denali Fault earthquake, *Bull. Seism. Soc. Am.,* **94,** S348-S359.

Qiu, Z. & Shi, Y., 2004. Application of observed strain steps to the study of remote earthquake stress triggering, *Acta Seismologica Sinica,* **17,** 534-541.

Reasenberg, P. & Simpson, R., 1992. Response of regional seismicity to the static stress change produced by the Loma Prieta earthquake, *Science,* **255,** 1687-1690.

Reilinger, R., McClusky, S., Oral, M., King, R., Toksoz, M., Barka, A., Kinik, I., Lenk, O. & Sanli, I., 1997. Global Positioning System measurements of present-day crustal movements in the Arabia-Africa-Eurasia plate collision zone, *J. Geophys. Res.,* **102,** 9983-9999.

Revenaugh, J., 2000. The relation of crustal scattering to seismicity in Southern California, *J. Geophys. Res.,* **105,** 25403-25422.

Rice, J., Sammis, C. & Parsons, R., 2005. Off-fault secondary failure induced by a dynamic slip pulse, *Bull. Seism. Soc. Am.,* **95,** 109.

Rojstaczer, S., Wolf, S. & Michel, R., 1995. Permeability enhancement in the shallow crust as a cause of earthquake-induced hydrological changes, *Nature,* **373,** 237-239.

Rubinstein, J., 2011. Nonlinear Site Response in Medium Magnitude Earthquakes near Parkfield, California, *Bull. Seism. Soc. Am.,* **101,** 275-286.

Rubinstein, J. & Beroza, G., 2004a. Evidence for Widespread Nonlinear Strong Ground Motion in the MW 6.9 Loma Prieta Earthquake, *Bull. Seism. Soc. Am.,* **94,** 1595-1608.

Rubinstein, J. & Beroza, G., 2004b. Nonlinear strong ground motion in the ML 5.4 Chittenden earthquake: Evidence that preexisting damage increases susceptibility to further damage, *Geophys. Res. Lett,* **31,** L23614, doi:23610.21029/22004GL021357.

Rubinstein, J. & Beroza, G., 2005. Depth constraints on nonlinear strong ground motion from the 2004 Parkfield earthquake, *Geophys. Res. Lett,* L14313.

Rubinstein, J., Gomberg, J., Vidale, J., Wech, A., Kao, H., Creager, K. & Rogers, G., 2009. Seismic wave triggering of nonvolcanic tremor, episodic tremor and slip, and earthquakes on Vancouver Island, *J. Geophys. Res,* **114,** B00A01, doi:10.1029/2008JB005875.

Rubinstein, J., Uchida, N. & Beroza, G., 2007a. Seismic velocity reductions caused by the 2003 Tokachi-Oki earthquake, *J. Geophys. Res,* B05315.

Rubinstein, J., Vidale, J., Gomberg, J., Bodin, P., Creager, K. & Malone, S., 2007b. Non-volcanic tremor driven by large transient shear stresses, *Nature,* **448,** 579-582.

Satoh, T., Fushimi, M. & Tatsumi, Y., 2001. Inversion of Strain-Dependent Nonlinear Characteristics of Soils Using Weak and Strong Motions Observed by Borehole Sites in Japan, *Bull. Seism. Soc. Am.,* **91,** 365-380.

Satoh, T., Sato, T. & Kawase, H., 1995. Nonlinear behavior of soil sediments identified by using borehole records observed at the Ashigra Valley, Japan, *Bull. Seism. Soc. Am.,* **85,** 1821-1834.

Sawazaki, K., Sato, H., Nakahara, H. & Nishimura, T., 2006. Temporal change in site response caused by earthquake strong motion as revealed from coda spectral ratio measurement, *Geophys. Res. Lett.,* **33,** L21303, doi:21310.21029/22006GL027938.

Sawazaki, K., Sato, H., Nakahara, H. & Nishimura, T., 2009. Time-Lapse Changes of Seismic Velocity in the Shallow Ground Caused by Strong Ground Motion Shock of the 2000 Western-Tottori Earthquake, Japan, as Revealed from Coda Deconvolution Analysis, *Bull. Seism. Soc. Am.,* **99,** 352-366.

Schaff, D. & Beroza, G., 2004. Coseismic and postseismic velocity changes measured by repeating earthquakes, *J. Geophys. Res,* B10302.

Scholz, C., 2002. The mechanics of earthquakes and faulting, 2nd ed., 471 pp., Cambridge Univ Press, New York.

Seeber, L., Armbruster, J., Ozer, N., Aktar, M., Baris, S., Okaya, D., Ben-Zion, Y. & Field, E., 2000. The 1999 Earthquake Sequence along the North Anatolia Transform at the juncture between the two main ruptures, *The 1999 İzmit and Düzce Earthquakes: Preliminary Results***,** 209–223, eds Barka, A., Kozaci, O., Akyuz, S. & Altunel, E., Istanbul Technical University, Turkey.

Seed, H., Idriss, I., Engineering, C.o., Center, E.E.R. & California, B.U.o., 1970. Soil Moduli and Damping Factors for Dynamic Response AnalysesCollege of Engineering, University of California.

Seed, H., Idriss, I., Group, G.E., Mechanics, S., Transportation, I.o., Engineering, T. & California, B.U.o., 1969. Influence of Soil Conditions on Ground Motions During EarthquakesUniv. of California, Institute of Transportation and Traffic Engineering, Soil Mechanics Laboratory.

Shelly, D., Beroza, G., Ide, S. & Nakamula, S., 2006. Low-frequency earthquakes in Shikoku, Japan, and their relationship to episodic tremor and slip, *Nature,* **442,** 188-191.

Shelly, D., Peng, Z., Hill, D.P. & Aiken, C., 2011. Tremor evidence for dynamically triggered creep events on the deep San Andreas Fault, *Nature Geosci.,* in press.

Sleep, N. & Ma, S., 2008. Production of brief extreme ground acceleration pulses by nonlinear mechanisms in the shallow subsurface, *Geochem. Geophys. Geosyst,* **9,** Q03008, doi:03010.01029/02007GC001863.

Steidl, J., Tumarkin, A. & Archuleta, R., 1996. What is a reference site?, *Bull. Seism. Soc. Am.,* **86,** 1733-1748.

Stein, S. & Wysession, M., 2003. An introduction to seismology, earthquakes, and earth structure, 88-90, Blackwell Publishing, Malden, MA, USA.

Su, F., Anderson, J. & Zeng, Y., 1998. Study of weak and strong ground motion including nonlinearity from the Northridge, California, earthquake sequence, *Bull. Seism. Soc. Am.,* **88,** 1411-1425.

Suzuki, W., Aoi, S., Sekiguchi, H. & Kunugi, T., 2011. Rupture process of the 2011 off the Pacific coast of Tohoku earthquake derived from strong-motion data**,** Japan Geoscience Union Meeting MIS036-P043, Makuhari, Chiba, Japan, May 022-027.

Tang, C.-C., Peng, Z., Chao, K., Chen, C.-H. & Lin, C.-H., 2010. Detecting low-frequency earthquakes within non-volcanic tremor in Southern Taiwan triggered by the 2005 Mw8.6 Nias Earthquake, *Geophys. Res. Lett.,* **37,** L16307, doi:16310.11029/12010GL043918.

TenCate, J., Pasqualini, D., Habib, S., Heitmann, K., Higdon, D. & Johnson, P., 2004. Nonlinear and nonequilibrium dynamics in geomaterials, *Phys. Rev. Lett.,* **93,** doi: 10.1103/PhysRevLett.1193.065501.

Trifunac, M., Hao, T. & Todorovska, M., 1999. On the reoccurrence of site specific response, *Soil. Dyn. Earthquake Eng.,* **18,** 569-592.

Tsuda, K., Archuleta, R. & Jamison, S., 2006. Confirmation of Nonlinear Site Response: Case Study from 2003 and 2005 Miyagi-Oki Earthquakes, *Bull. Seism. Soc. Am.,* **96,** 926-942.

Vakhnenko, O., Vakhnenko, V. & Shankland, T., 2005. Soft-ratchet modeling of end-point memory in the nonlinear resonant response of sedimentary rocks, *Physical Review B,* 1-14.

Van der Elst, N. & Brodsky, E., 2010. Connecting near-field and far-field earthquake triggering to dynamic strain, *J. Geophys. Res.,* **115,** B07311, doi:07310.01029/02009JB006681.

Velasco, A., Hernandez, S., Parsons, T. & Pankow, K., 2008. Global ubiquity of dynamic earthquake triggering, *Nature Geoscience,* **1,** 375-379.

Vidale, J. & Li, Y., 2003. Damage to the shallow Landers fault from the nearby Hector Mine earthquake, *Nature,* **421,** 524-526.

Vucetic, M. & Dobry, R., 1991. Effect of soil plasticity on cyclic response, *Journal of Geotechnical Engineering,* **117,** 89-107.

Waldhauser, F., 2001. HypoDD-A program to compute double-difference hypocenter locations, *US Geological Survey. Open File Report***,** 01-113.

Wang, C., Wang, C. & Manga, M., 2004. Coseismic release of water from mountains: Evidence from the 1999 (Mw= 7.5) Chi-Chi, Taiwan, earthquake, *Geology,* **32,** 769.

Wang, Y., Zhou, L. & Li, J., 2011. Intracontinental superimposed tectonics—A case study in the Western Hills of Beijing, eastern China, *Geol. Soc. Am. Bull.***,** doi:10.1130/B30257.30251.

Wu, C. & Peng, Z., 2011. Temporal Changes of Site Response During the Mw9.0 Tohoku Earthquake in Japan, *Earth Planets Space***,** in press.

Wu, C., Peng, Z. & Assimaki, D., 2009a. Temporal changes in site response associated with strong ground motion of 2004 Mw6. 6 Mid-Niigata earthquake sequences in Japan, *Bull. Seism. Soc. Am.,* **99,** 3487–3495.

Wu, C., Peng, Z. & Ben-Zion, Y., 2009b. Non-linearity and temporal changes of fault zone site response associated with strong ground motion, *Geophys. J. Int.,* **176,** 265-278.

Wu, C., Peng, Z. & Ben-Zion, Y., 2010. Refined thresholds for nonlinear ground motion and temporal changes of site response associated with medium size earthquakes, *Geophys. J. Int.,* **183,** 1567-1576, doi:1510.1111/j.1365-1246X.2010.04704.x.

Wu, C., Peng, Z., Wang, W. & Chen, Q., 2011. Dynamic triggering of shallow earthquakes near Beijing, China, *Geophys. J. Int.,* **185,** 1321–1334, doi: 1310.1111/j.1365-1246X.2011.05002.x.

Yan, D., Zhou, M., Song, H., Wang, G. & Sun, M., 2006. Mesozoic extensional structures of the Fangshan tectonic dome and their subsequent reworking during collisional accretion of the North China Block, *Journal of Geological Society,* **163,** 127-142.

Yang, W., Ben-Zion, Y. & Peng, Z., 2007. Correcting clipped seismic waveform by using waveforms of similar events, *Seis. Res. Lett.,* **78,** 249.

Yu, G., Anderson, J. & Siddharthan, R., 1992. On the characteristics of nonlinear soil response, *Bull. Seism. Soc. Am.,* **83,** 218-244.

Zhao, P., Peng, Z. & Sabra, K., 2010. Detecting remotely triggered temporal changes around the Parkfield section of the San Andreas Fault, *Earthquake Science,* **23,** 497-509.